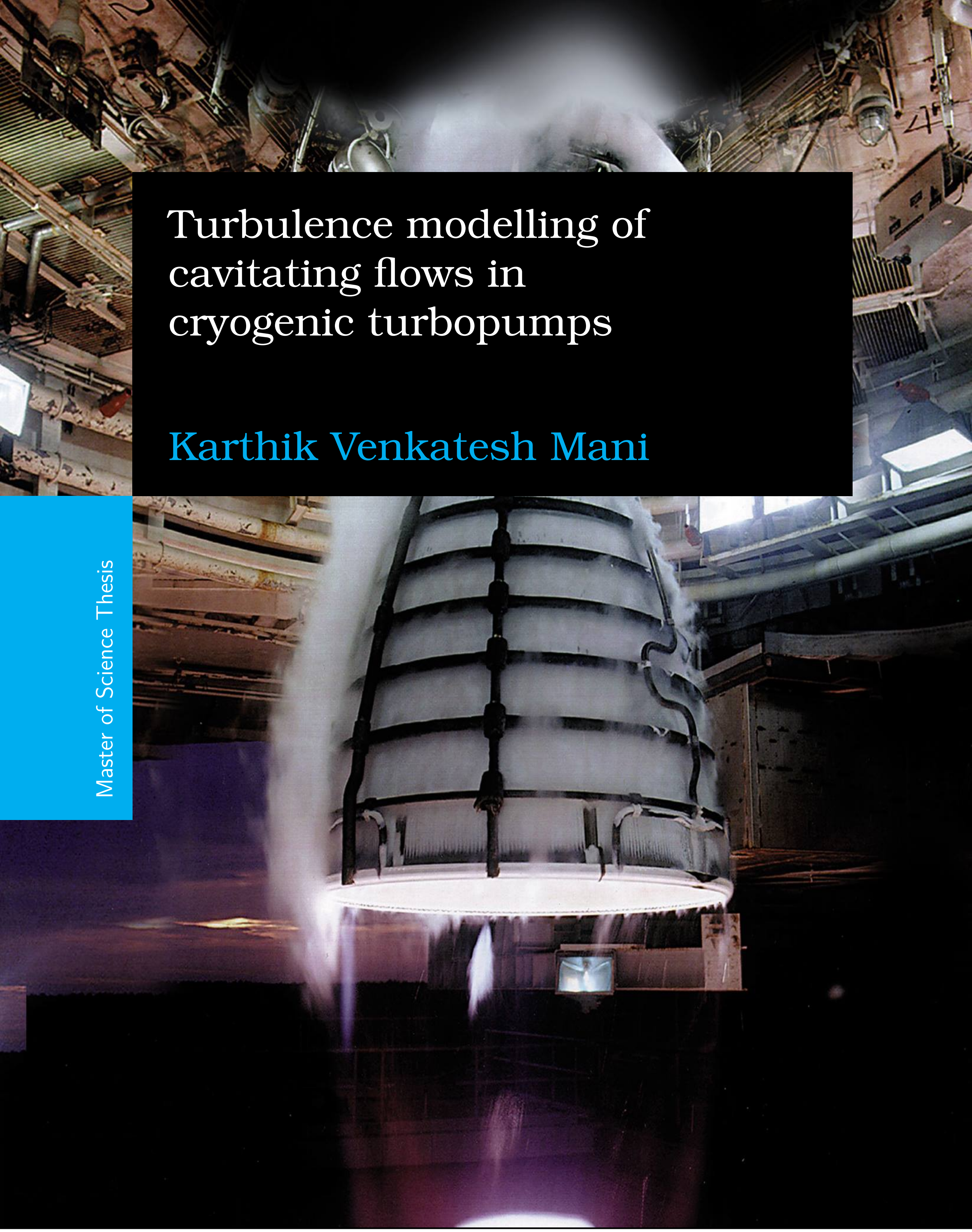

Turbulence modelling of cavitating flows in cryogenic turbopumps

Karthik Venkatesh Mani

Master of Science Thesis

Delft University of Technology

Space Engineering

Turbulence modelling of cavitating flows in cryogenic turbopumps

MASTER OF SCIENCE THESIS

For the degree of Master of Science in Space Engineering at Delft
University of Technology

Karthik Venkatesh Mani

October 27, 2015

Faculty of Faculty of Aerospace Engineering (AE) · Delft University of Technology

This thesis was pursued at the Deutsches Zentrum für Luft- und Raumfahrt e.V Institute of Aerodynamics and Flow Technology, Spacecraft Department, Göttingen, Germany

Abstract

Robust turbulence modelling of cavitating flows is essential for physically accurate predictions of the performance characteristics of cryogenic rocket turbo-pump inducers. Numerical modelling of such flows complement experiments and are comparatively inexpensive, but they lack accurate predictive capabilities. This work focuses on the characterisation of the choice of turbulence models on cavitation predictions for the modelling of cryogenic turbo-pump inducer. To isolate the influence of the turbulence modelling effects on the concurrent physical phenomena arising in the inducer, four canonical problems are abstracted and studied individually to separately consider rotation, adverse pressure gradients, blade passage and bluff body cavitation. Additionally, cavitation bubble dynamics in a bubbly flow in a 3D inducer are numerically simulated and studied so as to understand the effects of such on flow turbulence. It has been found that the type of cavitation model and the choice of turbulence model play a major role in the prediction of phase-distribution in the flow and concomitantly, on the cavitation induced instabilities predicted from computational fluid dynamics. The influence of the turbulence model is strongly dependent on the type of flow and a universal model which can be used to accurately predict cavitation in all flow domains seems to be unavailable among the existing classical turbulence closure models (both for two-equation and second-order closures). Stark differences in the predictions of cavitation are observed among non-bounded, bounded, and rotating flows based uniquely on the selection of turbulence models. The influence of other parameters such as the thermo-physical fluid characteristics, Reynolds number, or turbulence intensity have a minor effect for non-bounded flows. On the other hand, cavitation arising within the blade passage (bounded flows), the selection of the thermo-physical characteristics has a great effect on the cavitation prediction. Simulations of bubble dynamics using the Rayleigh-Plesset equation in cryogenic bubbly flows, with and without thermal effects, clearly depict the cavitating regions in a 3D inducer and yield corresponding bubble oscillation frequencies and time scales. The thermal effects attenuate bubble oscillations and distinct dominant frequencies of oscillations are observed for changing initial bubble radii. The information obtained from the turbulence model influence on cavitation and bubble oscillation influence on flow turbulence is used in the analysis of turbulence-cavitation interaction. A set of considerations are provided to turbo-pump designers as they need to carefully consider the choice of turbulence model and cavitation physics in order to use CFD tools to predictively model cryogenic inducers. These considerations will in turn help to improve dependability of the CFD tools, which will lead to reduced computational and monetary costs.

Acknowledgement

Firstly, I would like to thank Prof. Dr. Klaus Hannemann, the head of Spacecraft Department at DLR Institute of Aerodynamics and Flow technology - Göttingen, for giving me this wonderful opportunity to work there on my master thesis. I would like to thank my supervisors, Dr. Jean-Pierre Hickey and Dr. Angelo Cervone who helped me immeasurably.

I learned a lot from Dr. Hickey who not only helped me grow as an independent researcher but also gave me wonderful insights to multiple problems and guided me whenever I had questions. His support has been insurmountable and I shall forever be grateful to him.

I couldn't have done a good work without my friends. I would like to particularly thank my friends and colleagues in Delft and in Göttingen. I had an amazing group of friends in Delft with whom I had my fair share of fun and frolic, the DTs : Sajjad, Dharani, Shashank, Srivatsan, Gowrishankar, Avinash, Ajay, and Venky. They have been my family away from home. I would also like to thank some of my closest friends in Delft: Chabely, Pattareeya, Carlos, Chris, Francisco, Enrico, Andreas, Mihir, and Laura. I cannot thank enough my friends in Göttingen: Laureen, Clement, Enikő, Philipp, Gabriella, Cristina, Chiara, Carla, and Francis. I shall always relish the times that I spent in these two wonderful cities with the company of my friends.

ஈன்ற பொழுதின் பெரிதுவக்கும் தன்மகனைச்
சான்றோன் எனக்கேட்ட தாய்

The mother who hears her son called 'a wise man'
will rejoice more than she did at his birth

∼ Thiruvalluvar, Classical Tamil poet

I would like to thank my mother Mrs. Umamaheswari Mani and my father Dr. Manibharathi for their unconditional love and immeasurable faith that they have in me. Mom and Dad, I could have never been the person who I am now without you. There aren't enough words to thank you.

Delft University of Technology
October 27, 2015

Karthik Venkatesh Mani

Table of Contents

List of Figures

List of Tables

Glossary

List of Acronyms

DNS	Direct Numerical Simulation
RSM	Reynolds Stress Model
LH2	Liquid Hydrogen
LOX	Liquid Oxygen
LN2	Liquid Nitrogen
BES	Barotropic Equation based Solver
TES	Transport Equation based Solver

List of Symbols

α_l	Liquid volume fraction
β	Volume expansion coefficient in buoyancy
δ_T	Thermal boundary layer thickness
δ_{ij}	Kronecker delta function
κ	von Karman constant
Λ	Fluid dynamic parameter
λ	Latent heat of vapourisation
μ	Dynamic viscosity
μ_a	Acoustic viscosity
μ_l	Dynamic viscosity of the liquid
μ_t	Turbulent eddy viscosity
$\mu_{thermal}$	Thermal viscosity

μ_{eff}	Effective viscosity
ν	Kinematic viscosity
Ω	Rotational speed of the inducer
ω	Angular frequency
ω	Specific dissipation rate of the turbulent kinetic energy
ω_k	Angular rotation vector
Ω_{ij}	Rate of rotation tensor
Π_{ij}	Pressure-strain correlation
ψ	Amplitude of oscillation for the bubble radius
ρ	Density
ρ_w	Near wall density
ρ_{mix}	Mixture density
ρ_l	Density of liquid
ρ_V	Density of vapour
Σ	Thermodynamic parameter
σ	Cavitation number
σ_ε	Constant in the dissipation rate equation
σ_i	Incipient cavitation number
σ_k	Constant in the turbulent kinetic energy equation
$\sigma_{C_{min}}$	Modified cavitation number
σ_{rr}	Net force per unit area in the radial direction
τ_w	Wall shear stress
τ_{ij}	Shear stress
ε	Dissipation rate of the turbulent kinetic energy
$\zeta(x,t)$	Function to denote continuous phase
$\bar{u}$	Mean velocity
$\dot{m}^+$	Condensation source term
$\dot{m}^-$	Evaporation source term
$\mathcal{A}$	Thermal diffusivity
$\mathcal{R}_{gas}$	Gas constant
C_D	Drag coefficient
C_L	Coefficient of lift
c_l	Speed of sound in liquid
C_p	Specific heat at constant pressure
c_m	Isothermal harmonic speed of sound
C_ρ	Speed of sound
$C_{\varepsilon 1}$	Constant in the dissipation rate equation
$C_{\varepsilon 2}$	Constant in the dissipation rate equation
c_{sat}	Saturated concentration
C_{am}	Added mass coefficient

C_{dest}	Evaporation empirical production constant
$C_{p_{min}}$	Coefficient of Pressure at minimum pressure
C_{prod}	Condensation empirical production constant
d_b	Bubble diameter
e_{ikm}	Alternator in the rotational transport term
F_1 and F_2	Blending functions
F_{drag}	Drag force
g_o	Acceleration due to gravity
k_H	Henry's law constant
k_l	Thermal conductivity of the liquid
k_{BI}	Bubble induced turbulent kinetic energy
l_c	Characteristic cavity size
m_g	Mass of non-condensable gas
M_t	Turbulent Mach number
p_c	Critical pressure
p_i	Inlet pressure
P_k	Turbulent kinetic energy production
p_o	Characteristic pressure
P_t	Turbulence production
p_∞	Freestream pressure
p_∞	Pressure at a point far away from the bubble
p_∞^c	Constant freestream pressure
p_B	Pressure inside the bubble
p_g	Pressure of the non-condensable gas
p_v	Vapour pressure
p_{min}	Minimum pressure
$p_{C_{min}}$	Minimum cavity pressure
R^*	Constant
R_o	Initial bubble radius
r_T	Impeller tip radius
R_{eq}	Equilibrium bubble radius
R_{max}	Maximum bubble radius
S_ω	Source term for specific dissipation rate of turbulent kinetic energy
S_ε	Source term for dissipation rate of turbulent kinetic energy
S_k	Source term for turbulent kinetic energy
S_{ij}	Rate of strain tensor
T_B	Temperature inside the bubble
T_∞	Temperature at a point far away from the bubble
t_{c1}	Critical time for a significant thermal term magnitude
u^+	Non-dimensional near wall velocity

U_∞	Free stream velocity
U_o	Characteristic velocity
$U_{I,n}$	Interface velocity
V_1	Liquid phase velocity
V_2	Vapour phase velocity
V_r	Relative velocity between phases
w_V	Vapour mass fraction
$W_{i,j}$	Interfacial work term
y^+	Non-dimensional wall distance
u'	Fluctuating velocity
C	Constant
C(n)	Constant
D	Mass diffusivity
f	Frequency of oscillation for a sheet cavity
H	Head
h	Specific enthalpy
k	Turbulent kinetic energy
L	Characteristic length
N	Pump speed
n	Constant
NPSH	Net Positive Suction Head
Pr	Prandtl number
Q	Volume flow rate
R	Bubble radius
r	Radial distance
S	Surface tension
T	Temperature
t	Time
u	Velocity

Chapter 1

Introduction

In Liquid Rocket Propulsion Systems, the liquid propellants stored in low-pressure tanks are delivered to the high-pressure combustion chamber by the turbopump assemblies. The system mass and precise control over propellant delivery are some of the most important parameters which influence the overall design. Every kilogram of mass saved in the launch vehicle results in enhanced performance of the vehicle and also gives way to an increased payload mass. Also, prevention of erratic delivery will preclude numerous thrust related problems. Owing to their great advantage in drastically reducing the required feed system mass, especially the tank mass, turbopump assemblies are widely used in large rocket applications. A turbopump assembly consists of one or two centrifugal pumps driven by a turbine. The turbine itself is driven by a high pressure gas generated from a gas generator or a pre-burner. There are multiple configurations for turbopump assemblies and they greatly depend upon the choice of propellants, the cycle of operation, thrust chamber requirements, and overall mission requirements.

However, owing to the complexity involved in controlling the mass flow rate, temperature, and pressure of the propellants, the design of turbopumps is highly complicated. The rotation speeds of the turbopump parts are very high and they are located close to the thrust chamber [1]. This is a source for large vibrations and noise, and eventually lead to certain flow instabilities. In fact, turbopumps are so important and problematic that the launch vehicles bearing them have been caustically described as "Turbopump with rocket attached." Upto 50% of the launch vehicle design budget is ascribed to this area [2].

Early turbopump assemblies included a single rotating shaft for both the fuel and the oxidiser [1]. These prove to be disadvantageous because the optimum points of operation are different for different fluids and a single shaft operation compromises on the performance of both and leads to an increase in overall system mass. This problem is especially significant when the fuel and oxidiser have a large difference in density. Thus, the launch vehicles in the last two decades have included separate turbopump assemblies for fuel and oxidiser to optimise the performance and reduce systems mass. Figure 1-1 shows some common turbopump assemblies.

Turbopumps need to have high rotating speeds because that improves pumping performance and reduces the size and mass of the assembly. However, high rotational speeds will lead

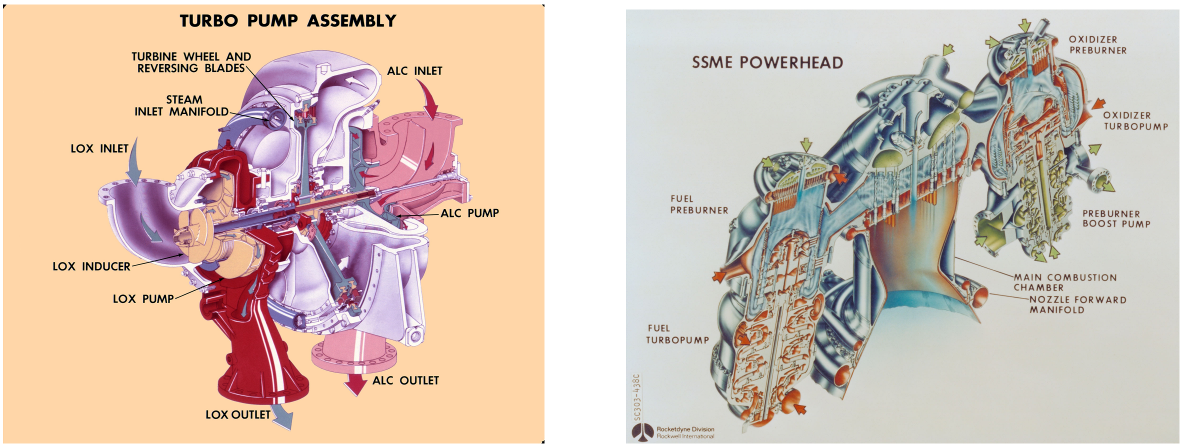

(a) Redstone - 1958

(b) Space Shuttle Main Engine - 1982

Figure 1-1: The turbopump assemblies of Redstone rocket [1958] and of the Space Shuttle Main Engine (SSME) [1982] are shown in this figure. We could observe the single shaft operation used in the older Redstone rocket and the separate assemblies for the later SSME. Figure courtesy - Rocketdyne

to problems such as cavitation, large vibrations, and excessive friction in the bearings which hold the shafts. Cavitation, which is the formation of vapour cavities in liquids, occurs when the static pressure of the liquid falls below its vapour pressure.

Cavitation occurring in cryogenic turbopumps is the central theme of this work. High shaft speeds lead to a rapid fall in pressure at the suction side of the pump impeller. This leads to the formation of cavitation bubbles (vapour bubbles) at the suction side. These bubbles travel with liquid bulk and then proceed on to collapse (implode) at the discharge side of the impeller because the pressure is recovered there. The amount of cavitation depends upon the rate and extent of fall in the local pressure, the initial number of bubbles in the flow, and the surface defects in flow domain. Extensive cavitation may give rise to mixing losses, insufficient power imparted to the fluid, erratic mass flow rate of the propellant, significant damage on the surface of the impeller, and dangerous vibrations owing to shock waves released by the collapsing cavity [3]. Considering these, the need to avoid cavitation drives the rotational speed requirements. Also, the usage of low density propellants in high speed rotating pumps means that there is high pump headrise thus requiring multiple impeller stages [1]. The turbopump design has to be optimized based on performance and weight. For example, high efficiency and low mass usually mean that there are small design margins and thus lower reliability. High shaft speed leads to low turbopump mass but it cavitates more and requires higher tank pressure (subsequently heavier tank mass) which negates the mass savings in the turbopump.

In the pump assembly, a special type of axial pump stage with helical or spiral impeller called *inducer* is placed upstream of the main pump impeller on the same shaft with the same rotating speed. There is a small propellant pressure increase (∼5-10%) due to this setup which is sufficient to avoid cavitation when the flow enters the main impeller. The inducer impeller, in some cases, is designed to operate at slightly cavitating conditions (2% head loss) [1] to improve the performance of the pump assembly.

In the inducer, multiple cavitating flow regimes are found. Some common types are attached leading edge cavitation, cloud cavitation due to the presence of a large number of bubbles in the flow, tip vortex cavitation occurring at the blade tips, backflow cavitation due to excessive pressure difference between discharge and suction sides, cavitating flow in the blade passages, and bluff body cavitation in the forward hemispherical head. The first four are shown in figure 1-2

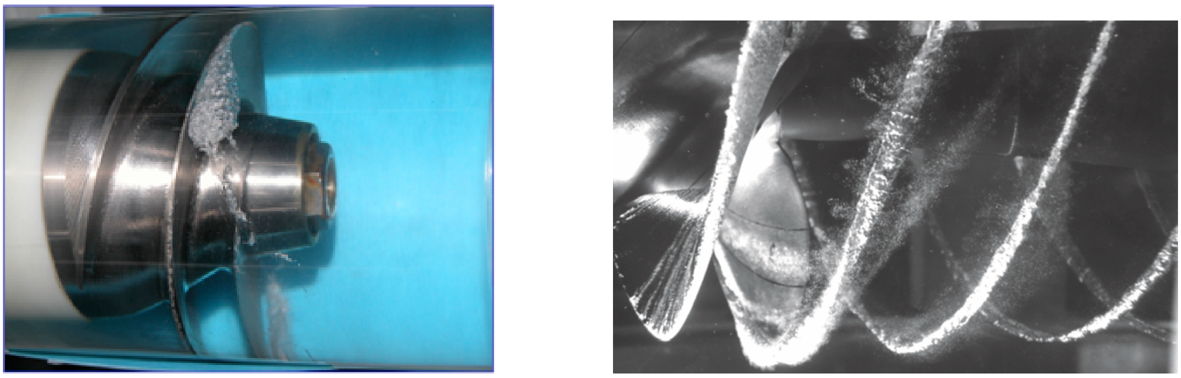

(a) Attached leading edge cavitation

(b) Tip vortex cavitation

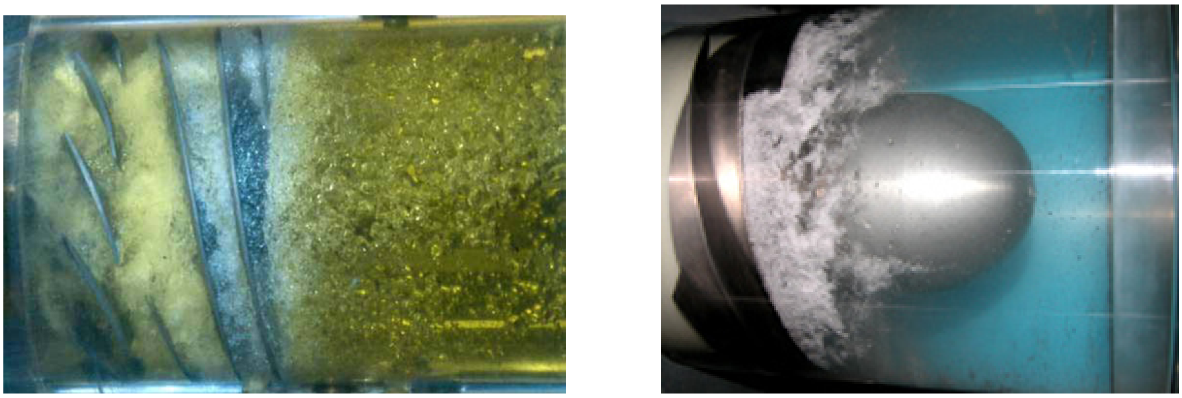

(c) Cloud cavitation

(d) Backflow cavitation

Figure 1-2: Typical cavitating regimes in inducers. (a) Attached leading edge cavitation occurs due to a negative pressure gradient along the surface and also due to rotation. (b) Tip vortex cavitation occurs at the blade tips of the inducer at significant rotational speeds. (c) Cloud cavitation occurs when a mixture of water and air bubbles flows through a variable pressure field. (d) backflow cavitation occurs due to the large pressure difference between discharge and suction sides. Image courtesy: C. Brennan, L. d'Agostino, and A. Cervone

To understand the complex cavitation phenomena occurring in turbopump inducers, several experimental works have been carried out. Most notable authors are L. B. Stripling and Acosta [3, 4]; A. Cervone, R. Testa, L. d'Agostino, and L. Torre [5, 6, 7, 8]; and Y. Tsujimoto, Y. Yoshida, S. Watanabe, K. Kikuta, T. Hashimoto etc [9, 10]. The experimental methods, although robust and accurate, are very expensive considering the computational, temporal, and monetary costs involved. We have to model, design, test, analyse, and iterate to achieve the required design point. These multiple design iterations are spread over a longer time and incur heavy costs.

Numerical modelling of cavitation shall help in expediting the study of cavitation phenomena that occur in turbopump inducers. Using numerical simulations, we can achieve faster cavitation predictions but while compromising on the accuracy (when compared to experimental investigations). These data regarding cavitation phenomena can be used while trying to design and test inducers thereby reducing the time and costs of design iterations for inducers. Notable works on cavitation simulations with similar characteristics to the flow regimes found in turbopumps have been carried out by authors such as Utturkar [11, 12], M. Deshpande [13] A. Hosangadi [14, 15, 16], V. Ahuja [17, 18], Coutier-Delgosha[19], J.L. Reboud [20, 21, 22], and E. Goncalves [23, 24, 25].

One of the areas where there is a large amount of uncertainty is the turbulence modelling of cryogenic cavitating flows. Turbulence modelling of cavitating flows can be carried out using Direct Numerical Simulations, Large Eddy Simulations, or Reynolds Averaged Navier-Stokes simulations. The typical flow Reynolds number based on blade-tip velocities lie in the range of 6 - 22 × 10^6. With such high Reynolds numbers, application of Large Eddy Simulations or Direct Numerical Simulations are impossible to implement on an industrial scale as they require very high computational power, time, and memory [26]. Thus, the viable solution is the usage of Reynolds Averaged Navier-Stokes equations based turbulence modelling approaches.

RANS-based approaches are the most computationally and monetarily feasible approaches with regards to turbopump cavitating flow modelling. These turbulence models, although having limitations, are applicable on a wide scale and have been thoroughly validated. To account for multiple flow phenomena while modelling, appropriate empirical and numerical correction terms/sources are used. Reynolds Averaging of the Navier-Stokes equations leads to the formation of an unresolved Reynolds Stress term which has to be modelled in order to provide *closure* to the problem. Thus, we use a specific set of extra equations to provide such a closure. Based on the number of additional equations used, these closure models are classified as One-Equation models (Spalart-Allmaras, Prandtl), Two-Equation Models ($k-\varepsilon$, $k-\omega$, $k-\omega$ SST, RNG $k-\varepsilon$ etc), and Second Moment Closures which use 7 equations.

Although RANS-based turbulence modelling is advantageous, a full three-dimensional simulation of a turbopump inducer flow will prove to be disadvantageous. In a full 3D flow, mutually coupled effects such as fluid-structure interactions, multiphase flow turbulence, thermosensitive cavitation, turbulence cavitation interactions, pulsating backflow, blade-tip leakage, rotation and cavitation induced unsteadiness must be addressed by the models. These effects are far too complex to be addressed together. Thus, to systematically investigate the turbulence modelling in cryogenic turbopump inducers, the complex cavitating flow regimes are isolated by decomposing them into simplified flow problems which are similar to certain canonical cavitating flow regimes where cavitation is well understood.

Some top level requirements for turbulence models are listed below. Quantification of requirements is especially hard in this case because of the uncertainty involved in turbulence modelling and also the lack of specific literature on turbulence modelling in real inducer geometries. To this extent, the following requirements should be used as rule of thumb.

- The models shall yield an accuracy of ±15% in cavitation length predictions compared to the corresponding literature.

- The simulations shall not take more than 10 hours time in a nominal personal computer setup having 8 gigabytes RAM and 4 cores of processors with 3.2 GHz frequency in total.
- The models shall be widely validated in canonical flow problems.
- The models shall have less approximations and shall closely emulate the physics of the problem in the investigated flow regimes.
- The models shall have good numerical stability.

These requirements shall serve as guidelines for gauging the performance of turbulence models in our simulations.

1-1 Motivation and objective

This project focuses on the numerical modelling of cavitating flows in cryogenic turbopump inducers. From a wide range of literature surveyed, many studies have investigated the effect of the choice of flow solvers and cavitation models on cavitation prediction, yet to the knowledge of the author, no one has specifically addressed the uncertainty regarding the choice of turbulence models on the prediction of cavitation in the multiple flow regimes found in cryogenic turbopump inducers. Also, the study of cavitation dynamics in a real world cryogenic flow through a rotating inducer and their influence on flow turbulence seems to be unavailable. To this extent, we investigate the turbulence influence on cavitation and conversely the cavitation dynamics influence on flow turbulence.

Thus, the motivation and subsequently the objectives behind this work are:

1. To address the uncertainty associated with the choice of turbulence models while modelling cavitating flows in cryogenic turbopumps.

2. To quantify and analyse the characteristics of bubble dynamics and their impact on flow turbulence in an actual turbopump inducer.

With these come the third and main objective:

3. To transpose the knowledge of turbulence modelling and bubble dynamics to assist the turbopump designers in their modelling strategies thus reducing overall costs and number of iterations while improving the predictive capabilities for cavitation.

To achieve these objectives, first a literature study on cavitation bubble dynamics, numerical modelling of cavitation, and on turbulence modelling is carried out. This shall provide a good theoretical understanding of the topics at hand. Secondly, the analysis of influence of control parameters on cavitation prediction in multiple flow regimes pertaining to cryogenic turbopump inducers is carried out. Thirdly, the cavitation bubble dynamics are characteristed and investigated by applying the Rayleigh-Plesset equation for bubble dynamics for a three-dimensional cryogenic bubbly flow through an inducer. Finally, the turbulence-cavitation interaction is studied and specific recommendations are made to the turbopump designers which shall assist them in optimizing their numerical simulations, account for actual flow physics, and reduce the number of iterations and costs in order to achieve their desired design point.

The next section highlights the main and subordinate research questions. Although all research questions are answered in the upcoming chapters, the answers to the main research questions are exclusively highlighted in the concluding chapter. The sub-questions have their answers in the concluding sections of the corresponding chapters.

1-2 Research questions and hypothesis

1-2-1 Main research questions

- What is the relative importance of turbulence modelling in cryogenic turbopumps?
    - Hypothesis: Apriori assessment is that the turbulence models should play an important role in influencing cavitation predictions. This is based on the variation in the formulation of the multiple RANS based turbulence models under consideration. However, owing to a multitude of interactions of physical phenomena, it is difficult to arrive at a strong conclusion apriori. The importance of turbulence models could vary under different conditions.
    - How much, by magnitude, do the results among the turbulence models vary?
- What is the most *accurate* RANS based turbulence model to predict the size and onset of attached cavitation bubbles in cryogenic turbopump inducers?
    - Hypothesis: Accuracy encompasses physical and computational accuracy. The approximate requirement for accuracy for any parameter is ±15% of the corresponding literature value. However, only canonical problems can be investigated for which we could define the accuracy of a turbulence model. Literature specific to cryogenic inducers are classified or unavailable. Theoretically, the Reynolds Stress Model should yield the most *accurate* result because it has the least modelling assumptions and provides the highest level of closure which is computationally feasible. However, the sensitivity of Reynolds Stress Model to the physical phenomena occurring in inducers are still unknown. Thus, the accuracy of a particular turbulence model will heavily depend upon the flow regime.
    - How accurate, with respect to the literature, are the cavitation predictions by multiple turbulence models?
- What are the characteristics of bubble dynamics in an inducer flow and how do they affect flow turbulence?
    - Hypothesis: The primary characteristics to be quantified and analysed are bubble oscillation time and length scales. The bubble oscillations and corresponding dynamics do have an effect on flow turbulence. However, the magnitude of effects are unknown. The hypothesis here is that the bubble oscillations will either augment or attenuate flow turbulence proportional to their magnitude. However, it could be heavily dependent upon operating conditions.

- What are the recommendations for turbopump designers with regards to turbulence modelling in order to improve predictive modelling capabilities?

1-2-2 Sub-questions based on the analysis of influence of parameters

- Which parameters or flow conditions have a significant influence on cavitation prediction?
    - Control parameters: Turbulence models, flow solver, turbulence intensity, operating fluid, Reynolds number, cavitation model, and compressibility model

1-2-3 Sub-questions based on cavitation bubble dynamics

- What are the characteristics frequencies and time scales of bubble oscillations in an inducer?
- How do the thermal effects affect the characteristic scales of oscillation?
- What are the strategies to account for turbulence-cavitation interaction?

1-2-4 Questions based on aposteriori analysis

- What are the problems and limitations that currently exist for numerical and turbulence modelling techniques for cavitating flows?

Chapter 2

Literature review and theoretical background

This chapter contains the theoretical background regarding cavitation bubble dynamics, cavitation modelling approaches, and turbulence models. In the first case, the behaviour of cavitation bubbles, especially their growth and collapse in non-cryogenic and cryogenic flows under a variable pressure field are discussed. The dynamics of cavitating bubbles are governed by the Rayleigh-Plesset equation for bubble dynamics. Thermal effects which happen in the case of cryogenic fluids and heated fluids are also discussed. In the section regarding cavitation modelling, the current state-of-the-art approaches towards interface tracking and modelling of cavitating flows are described. Finally, RANS-based turbulence models and their advantages/disadvantages are laid out in detail.

2-1 Cavitation bubble dynamics

To measure the extent of cavitation, a dimensionless quantity known as Cavitation Number is used. It is defined using the formula (2-1)

$$\sigma = \frac{(p_\infty - p_c)}{\frac{1}{2}\,\rho\,U_\infty^2} \tag{2-1}$$

In hydrofoils, turbine blades, and aerofoils, another useful quantity to define is the coefficient of pressure.

$$C_{p_{\min}} = \frac{(p_{\min} - p_\infty)}{\frac{1}{2}\,\rho\,U_\infty^2} \tag{2-2}$$

Where, p_∞ is the ambient pressure, p_c is the critical pressure or vapour pressure, p_{min} is the minimum pressure, ρ is the density, and U_∞ is the freestream velocity. In simple terms, when $\sigma = C_{p_{min}}$, then cavitation is said to occur. However, there are multiple parameters which influence cavitation inception, topology, and extent. The general explanation that cavitation occurs when the pressure of the liquid falls below its vapour pressure is inadequate to describe the actual physics of it. Arndt [27] states that the inception of cavitation occurs due to the rapid growth in small vapour bubbles (nuclei) that become unstable due to a change in ambient pressure. These nuclei are either embedded in the flow or originate at certain cracks or crevices on the surface of the pump parts.

Also, cavitation is an unsteady phenomenon and is usually oscillating with an associated frequency. For a flow over a hydrofoil, a strong dynamic sheet cavitation occurs. The frequency of oscillation of this sheet cavitation layer is given by [27] :

$$\frac{f\,l_c}{U_\infty} = \frac{1}{4}\sqrt{1-\sigma} \tag{2-3}$$

Here, f is the frequency of oscillation, l_c is the characteristic length or size of the cavity, and U_∞ is the characteristic velocity of the flow. It is good to note that the cavitation number σ here is defined by the pressure in the cavity which may or may not be equal to the vapour pressure [27]. In unsteady cavitation, there are additional pressure losses at the inducer which in turn produce periodic surges in flow with the size of the cavity fluctuating (increasing and decreasing) [3].

The dynamics of a cavitation bubble are governed by the Rayleigh-Plesset equation (2-4) [28] [29]. In cryogenic cavitation and high temperature cavitation, thermal effects play a significant role. The thermal effects are discussed in section 2-1-1

$$\overbrace{\frac{p_V(T_\infty)-p_\infty(t)}{\rho_l}}^{\text{Instantaneous tension term}} + \overbrace{\Sigma\frac{dR}{dt}\sqrt{t}}^{\text{Thermal effects term}} \overbrace{+\frac{p_g}{\rho_l}\left(\frac{T_B}{T_\infty}\right)\left(\frac{R_o}{R}\right)^{3\gamma}}^{\text{Non-condensable gas}}$$
$$= \underbrace{R\frac{d^2R}{dt^2}+\frac{3}{2}\left(\frac{dR}{dt}\right)^2}_{\text{Inertial terms}} + \underbrace{\frac{4\nu_l}{R}\frac{dR}{dt}}_{\text{Viscous term}} + \underbrace{\frac{2S}{R\,\rho_l}}_{\text{Surface tension term}} \tag{2-4}$$

The term p_V is the vapour pressure, p_∞(t) is the pressure of the liquid far from the bubble, p_B(t) is the pressure inside the bubble, T_B is the bubble temperature, p_{g0} is the non-condensable gas pressure, Σ is the thermal effects coefficient, R(t) is the radius of the bubble, ν_l is the kinematic viscosity of the liquid, ρ_l is the density of the liquid, and S is the surface tension of the bubble. The quantity p_∞ is an already known input value. From the Rayleigh-Plesset equation, we can find the bubble radius R(t), provided we know the bubble pressure p_B. This equation assumes a perfectly spherical bubble and in reality that is not always the case.

The thermal effects coefficient or the thermodynamic parameter is defined using the formula [29],

$$\Sigma = \left[\frac{\lambda_{vap}^2}{T_\infty C_{pl}\sqrt{\mathcal{A}_l}}\right]\left[\frac{\rho_v}{\rho_l}\right]^2 \tag{2-5}$$

Here, λ_{vap} is the latent heat of vapourisation of the liquid, C_{pl} is the specific heat capacity of the liquid, $\mathcal{A}$ is the thermal diffusivity. Sometimes, this definition is not adequate to accurately model the thermal effects. Thus we use a technique listed in [6] to estimate an iterated value.

The primary mechanisms involved in bubble dynamics are bubble growth and collapse. When the pressure falls, the bubbles grow and reach their maximum size when the pressure is minimum. Then, when there is pressure recovery, the bubble collapse occurs. Owing to pressure fluctuations, the bubbles grow and collapse rapidly and there are oscillations in bubble radii. However, the process is usually non-linear and analytical solutions seldom exist. The asymptotic growth rate of the bubble is defined as,

$$\frac{dR}{dt} \rightarrow \left\{ \frac{2}{3} \frac{(p_V - p_\infty)}{\rho_l} \right\}^{\frac{1}{2}} \tag{2-6}$$

Initially, there is a period of acceleration. Then, the velocity of the interface becomes relatively constant. The equation (2-6) denotes an explosive bubble growth when $p_\infty > p_V$.

2-1-1 Thermal effects in bubble dynamics

Thermal effects play a major role in altering the bubble dynamics. Sustenance of the cavity size is by the continuous vapourisation process. The physical properties of the operating fluid and the local flow conditions determine the size and shape of the cavity. In cryogenic fluids, the ratio between the densities of liquid and vapour phases is lower than non-cryogenic fluids such as water. Thus more liquid mass has to evaporate to sustain the cavity [30]. Thermal effects in cryogenic fluids correspond to the substantial depression in temperature in the vicinity of the liquid-vapour interface compared to the freestream temperature because the latent heat of vapourisation is drawn from the liquid bulk. This temperature depression is significant in cryogenic fluids because the point of operation is very close to its critical point. The temperature depression in the vicinity of the liquid-vapour interface reduces the local vapour pressure of the fluid. Thus, when cryogenic and non-cryogenic fluids flow through the same variable pressure field, the cavity size in the case of cryogenic fluids is smaller than the corresponding size observed in non-cryogenic fluids where there is no temperature depression [13, 30].

The thermal term in equation (2-4) is initially negligible in magnitude and grows as time progresses. At a certain time, it will have a significant effect on the bubble dynamics. The increase in the magnitude of thermal term leads to the reduction in cavitation bubble size and its growth rate. For a rapidly growing bubble, there exists a thin thermal boundary layer but when the growth rate is slow, a critical time for the thermal effects to achieve a magnitude comparable to the rest of terms is defined. The expression for critical time is,

$$t_{c1} = \frac{(p_V - p^c_\infty)}{\rho_l} \cdot \frac{1}{\Sigma^2} \tag{2-7}$$

Here, p^c_∞ is the constant freestream pressure. Now, this critical time, depends upon the tension $\left(p_V - p^c_\infty\right)/\rho_l$ and the thermodynamic parameter $\Sigma(T_\infty)$. The thermodynamic parameter is defined by equation (2-5). Since the thermodynamic parameter purely depends upon the liquid properties, especially the temperature, even a minor change in T_∞ (even from triple point to critical point) would cause drastic changes in Σ^2 term as Σ is directly proportional to (ρ_V^2/ρ_l^2). This in turn affects the critical time which will vary by many orders of magnitude. The thermal effects inhibit the bubble growth and the ensuing collapse is less intense compared to a non-cryogenic liquid such as water. When the first critical time has been crossed, the magnitude as well as the relative contribution of each term in the Rayleigh-Plesset equation, represented in equation (2-4), changes. The thermal term and the driving term take precedence over the inertial terms. The rate bubble growth decreases and the bubble continues to grow slowly. In cryogenic fluids, the bubble growth is thermally inhibited. Now, the asymptotic growth of a bubble in a liquid bulk without boundary effects is given by,

$$\frac{dR}{dt} = \frac{\left(p_V - p^c_\infty\right) t^{1/2}}{\frac{1}{2}\rho_L \, \Sigma\left(T_\infty\right)} \tag{2-8}$$

The thermally controlled growth of bubbles are also affected by non-equilibrium effects [31]. These effects occur when the evaporation rate is very high and the liquid-vapour interface ceases to have thermal equilibrium [32]. Convective heat transfer at the bubble surface also plays an important role in establishing a thermal boundary condition. Non-equilibrium occurs when $T_B \neq T_\infty$ and $p_V \neq p_{sat,L}$; where T_B and T_∞ are bubble and liquid bulk temperatures respectively and p_V and $p_{sat,L}$ are vapour pressure and saturation pressure of the liquid. The saturation pressure $p_{sat,L}$ is defined at the interface temperature T_L [31].

2-2 Cavitation Modelling

In cavitation modelling, the tracking of the liquid-vapour interface plays a crucial role in capturing the physics of cavitation. Cavitation modelling, especially the interface modelling strategy, through the computation of the Navier-Stokes equations, is broadly classified into two categories: the explicit interfacing tracking methods and the homogeneous flow models [33]. In explicit tracking methods used by Deshpande et al [13], the cavity region is assumed to have a constant pressure equal to the corresponding liquid vapour pressure. They explicitly update the liquid-vapour interface at each time step by measuring the pressure. Although the model is quite robust in simulating sheet cavitation, it is not quite useful in modelling the bubble growth and detachment mechanism. Also, the model is confined only to 2D simulations because the explicit tracking of the interface in a 3D flow is difficult and computationally expensive.

In homogeneous flow models, the liquid and the vapour phases are assumed to exist as a homogeneous two-phase mixture in a single fluid. The homogeneous flow modelling approaches are investigated in three different ways,

1. By using a barotropic relation to compute the density based on static pressure [34].

2. By using a bubbly two-phase flow model in which the density evolution is linked to the void fraction calculated from the motion and dynamics of bubbles in the flow. [35, 36, 37].

3. By using a transport equation for the liquid volume fraction α_l; which is the ratio of the volume of liquid and the volume of vapour. The interface density is calculated as a function of this volume fraction. [38, 39, 40, 41, 33, 11]

In the barotropic model, the density of the fluid is treated only as the function of pressure, $\rho = f(p)$. Barotropic compressibility effects are accounted for by using speed of sound models. In the approach where the density evolution is linked to the void fraction, the Rayleigh-Plesset equation is used to determine the bubble radius. The void fraction is calculated from the bubble radius and the density evolution is then calculated using the void fraction. The assumption here is that the bubbles have a spherical shape. This method is prone to instabilities because of the high pressure-density dependence and doesn't converge for non-cavitating flows. Chen et al [37] developed this work and derived a time and pressure dependent differential equation of density.

A transport equation model, which accounts for a flexible cavitation dynamics, is developed to model the volume fraction and the source terms for vapourisation and condensation to control the mass transfer between the two phases [38, 39, 40, 41]. In this model, the volume or the mass fraction of the liquid is convected. The advantage of this model is that the convective nature of the equation allows for the modelling of the impact of inertial forces on cavities such as elongation, detachment, and drift of bubbles [33]. The source terms for cavitation production and destruction are modelled.

Transport equation based cavitation models can be employed in a pressure based flow solver or a density based flow solver. While using pressure based solvers, the computational issues such as numerical stability and convergence in simulating unsteady flows is a major issue. Singhal et al [38] use a pressure based algorithm but they provide no information on stability and convergence of the model. In the pressure based solvers, the pressure field is solved by combining the mass and momentum continuity equations to form a pressure (or pressure correction) equation. Senocak et al [33] use a pressure based solver, with conservative formulation, multiblock, and curvilinear grid systems to compute cavitating flows. They discuss the pressure-velocity-density coupling to formulate the pressure correction equations for cavitating flows. Also, in the case of pressure based methods, modelling the speed of sound in the mixture region is an issue.

In the case of density based solvers, a special preconditioning formulation or artificial density approach is required. Merkle et al [39] and Kunz et al [40, 41] have employed an artificial compressibility method with special attention given to pre-conditioning formulation. Ahuja et al [18] developed an algorithm to account for the compressibility effects in the context of artifical compressibility with the use of adaptive unstructured meshes. Venkateswaran et al [42] studied the preconditioning methods by Kunz et al [40, 41] and Merkle et al [39], and summarised that the three preconditioning formulations are the same with minor differences.

In the context of cryogenic cavitation, the problem of cavitation modelling becomes even more complex because of the low liquid-vapour density ratio. The interface is not clearly defined and it is considered mushy [11]. The governing equations for cryogenic cavitation under single fluid modelling method includes four sets of equations: the Navier-Stokes equations which are Favre averaged and in conservative form, the energy equation, the two-equation $k-\varepsilon$ turbulence model closure (or second order moment closure), and an equation for liquid volume fraction transport.

The conservative form of the continuity, momentum, energy and the liquid volume fraction transport for the mixture are,

$$\frac{\partial \rho_{mix}}{\partial t} + \frac{\partial (\rho_{mix}\, u_j)}{\partial x_j} = 0 \tag{2-9}$$

$$\frac{\partial (\rho_{mix}\, u_i)}{\partial x_i} + \frac{\partial (\rho_{mix}\, u_i\, u_j)}{\partial x_j} = \frac{\partial p}{\partial x_i} + \frac{\partial}{\partial x_j}\left[(\mu + \mu_t)\left(\frac{\partial u_i}{\partial x_j} + \frac{\partial u_j}{\partial x_i} - \frac{2}{3}\frac{\partial u_k}{\partial x_k}\delta_{ij}\right)\right] \tag{2-10}$$

$$\frac{\partial}{\partial t}\left[\rho_{mix}\ (h + w_V \lambda)\right] + \frac{\partial}{\partial x_j}\left[\rho_{mix}\, u_j\ (h + w_V \lambda)\right] = \frac{\partial}{\partial x_j}\left[\left(\frac{\mu}{\mathrm{Pr}_{lam}} + \frac{\mu_t}{\mathrm{Pr}_t}\right)\frac{\partial h}{\partial x_j}\right] \tag{2-11}$$

$$\frac{\partial \alpha_l}{\partial t} + \frac{\partial (\alpha_l\, u_j)}{\partial x_j} = \dot{m}^+ + \dot{m}^- \tag{2-12}$$

Here, ρ_{mix} is the mixture density, x_i, x_j and x_k denote the coordinate axes with i, j, k denoting the components of the axes. Velocity is denoted by u_i, time by t, pressure by p, sensible enthalpy by h, mass fraction of the vapour by w_V, latent heat by λ, Prandtl number by Pr_{lam} (laminar) and Pr_t (turbulent), viscosity by μ (laminar) and μ_t (turbulent), liquid volume fraction by α_l, and condensation and evaporation source terms by $\dot{m}^+$ and $\dot{m}^-$ respectively.

The mixture density, sensible enthalpy, vapour mass fraction, and the turbulent viscosity are expressed as:

$$\rho_{mix} = \rho_l\, \alpha_l + \rho_V (1 - \alpha_l) \tag{2-13}$$

$$h = C_{P,l} T \tag{2-14}$$

$$w_V = \frac{\rho_V (1 - \alpha_l)}{\rho_{mix}} \tag{2-15}$$

$$\mu_t = \frac{\rho_{mix}\, C_\mu\, k^2}{\varepsilon} \tag{2-16}$$

The subscripts l and V denote liquid and vapour phases respectively. Also, $C_{P,l}$ is the specific heat, T is the temperature, k is the turbulent kinetic energy, and ε is the dissipation rate of k. In the case of cryogenic cavitation, the viscous dissipation and compressible effects are neglected from the energy equation because the temperature variation occurs due to evaporative cooling [11].

Authors	$\dot{m}^+$ term	$\dot{m}^-$ term
Singhal et al [43]	$\dfrac{C_{prod} MAX(p-p_V,0)(1-\alpha_l)}{(0.5\,\rho_l\,U_\infty^2)\,t_\infty}$	$\dfrac{C_{dest} MIN(p-p_V,0)\,\alpha_l}{(0.5\,\rho_l\,U_\infty^2)\,\rho_V\,t_\infty}$
Singhal et al [38]	$C_{prod}\dfrac{U_\infty}{\gamma}\rho_l\,\rho_V\left[\dfrac{2}{3}\dfrac{MAX(p-p_V,0)}{\rho_l}\right]^{0.5}$ $C_{prod}/\gamma, = 3.675E3$	$C_{dest}\dfrac{U_\infty}{\gamma}\rho_l\,\rho_V\left[\dfrac{2}{3}\dfrac{MIN(p-p_V,0)}{\rho_l}\right]^{0.5}$ $C_{dest}/\gamma, = 1.225E3$
Merkle et al [39]	Same as Singhal et al [43] with $C_{prod} = 80$	Singhal et al [43] with $C_{dest} = 1$
Kunz et al [41]	$\dfrac{C_{prod}\,\alpha_l^2(1-\alpha_l)}{\rho_l\,t_\infty}$	$\dfrac{C_{dest}\rho_V MIN(p-p_V,0)\,\alpha_l}{(0.5\,\rho_l\,U_\infty^2)\,\rho_l\,t_\infty}$
Senocak et al [33]	$\dfrac{C_{prod} MAX(p-p_V,0)(1-\alpha_l)}{(0.5\,\rho_l\,U_\infty^2)\,t_\infty}$	$\dfrac{C_{dest} MIN(p-p_V,0)\,\alpha_l}{(0.5\,\rho_l\,U_\infty^2)\,\rho_V\,t_\infty}$
Utturkar et al [12]	$\dfrac{C_{prod}}{0.5\,\rho_l\,U_\infty^2} = \dfrac{1}{(\rho_l-\rho_V)(U_{V,n}-U_{I,n})^2}$ $\dot{m}^+ = \dfrac{\rho_l MAX(p-p_V,0)(1-\alpha_l)}{\rho_+(U_{m,n}-U_{I,n})^2(\rho_l-\rho_V)t_\infty}$ $\dfrac{\rho_l}{\rho_+} = \dfrac{\rho_l}{\rho_{mix}}$	$\dfrac{C_{dest}}{0.5\,\rho_l\,U_\infty^2} = \dfrac{1}{(\rho_l-\rho_V)(U_{V,n}-U_{I,n})^2}$ $\dot{m}^- = \dfrac{\rho_l MIN(p-p_V,0)\alpha_l}{\rho_-(U_{m,n}-U_{I,n})^2(\rho_l-\rho_V)t_\infty}$ $\dfrac{\rho_l}{\rho_-} = \dfrac{\rho_l}{\rho_V} + \left(1.0-\dfrac{\rho_l}{\rho_V}\right)e^{-(1-\alpha_l)/\beta}$ $\beta, = O(0.1)$

Table 2-1: Condensation and evaporation source terms for different cavitation models

For solving the liquid volume transport equation, represented in (2-12), we use different *cavitation models* which vary by the formulation of the source terms for condensation ($\dot{m}^+$) and evaporation ($\dot{m}^-$). The different formulations as tabulated in Utturkar et al [11] is given in table 2-1

The source term models of Singhal et al [38, 43], Kunz et al [41, 40], and Merkle et al [39] are derived empirically. However, Senocak et al [33] have developed a semi-empirical model which relies on interface mass and momentum transfer. Although they look similar to the model developed by Singhal et al [38], the empirical condensation constant (production coefficient) C_{prod} and empirical evaporation constant (destruction coefficient) C_{dest} are physically more representative. In the work of Utturkar et al [12], the cavitation model of Senocak [33] was adopted and transformed to accommodate a mushy interface boundary condition for the liquid-vapour interface in the case of cryogenic cavitation. In a Mushy interfacial dynamics model, the vapour pressure is a function of the local temperature and the cavitation itself is less intense. As a consequence, existence of a pure vapour phase inside the cavity has a very low probability.

2-3 Turbulence Modelling

Turbulence modelling and simulation of cavitating flows can be done by Direct Numerical Simulation (DNS), Large Eddy Simulation (LES), Reynolds Averaged Navier-Stokes (RANS) Simulation, and a hybrid RANS/LES. In the case of Direct Numerical Simulation (DNS), all scales, the largest to the smallest, are resolved. No modelling is required because the Navier Stokes equations are directly solved. It is the simplest approach and has the highest accuracy. However, it not easily applicable for large Reynolds Number flows [26]. In cavitating flows, where multiple phases are present the DNS approach resolves the scales for each fluid phase and the interface. The pseudo-DNS approach resolves the scales for each fluid phase and tracks the interface. However, this is very difficult task even for simple 3D problems because of very high computational requirements[44, 22].

In LES, the large scales of turbulent motion are resolved and the small scales are modelled. LES is not as computationally expensive as DNS and is useful in calculating the turbulent statistics such as velocity and pressure fluctuations in the flow. A filter is used in LES to allow the passing of large scales and remove the small scales into the solution for the Navier Stokes equations. However, in turbulence modelling of cavitating flows, it introduces more problems in modelling because there are more sub-grid scale terms introduced which makes it very complex [44].

The most pursued turbulence modelling approach for cavitating flows is the RANS-based approach. In this, the mean flow is resolved and the turbulence is modelled. These are classified into Linear Eddy Viscosity Models, non-Linear Eddy Viscosity Models, and Second Moment Closures.

For the derivation of RANS equations, we take the continuity and momentum equations apply Reynolds decomposition (ex: $u(t) = \bar{u} + u'$), and obtain an average of the equations. Thus, the RANS equations look like,

$$\rho \left[\frac{\partial \bar{u}_i}{\partial t} + \frac{\partial \left(\bar{u}_i \, \bar{u}_j \right)}{\partial x_j} \right] = -\frac{\partial \bar{p}}{\partial x_i} + \frac{\partial}{\partial x} \left(\mu \frac{\partial \bar{u}_i}{\partial x} \right) - \frac{\partial}{\partial x_j} \left(\rho \, \overline{u_i' u_j'} \right) \tag{2-17}$$

The last term in equation (2-17) is the Reynolds stress term. This term arises due to Reynolds averaging. The Reynolds stress term consist of six unknown components and thus requires *closure*. This closure is obtained with the use of additional equations and the turbulence models are classified according to the number of additional equations that they use. The models are listed in table 2-2

In this chapter, we shall focus on the standard $k - \epsilon$ model, RNG $k - \epsilon$, Wilcox's $k - \omega$, Menter's $k - \omega$ Shear Stress Transport, and Reynolds Stress Models.

No. of extra equations	Model
0	Mixing Length Model (Zero equation model)
1	Spalart-Almaras model Prandtl One equation model
2	Standard $k-\varepsilon$ model Re-Normalisation Group (RNG) $k-\varepsilon$ model $k-\omega$ model Realizable $k-\omega$ model $k-l$ model
7	Reynolds Stress Model

Table 2-2: Turbulence models with classified according to the number of additional equations. The zero, one, and two equation models are called the Linear Eddy Viscosity models.

2-3-1 The $k-\varepsilon$ model

In the standard $k-\varepsilon$ model, we solve two additional transport equations for the turbulent kinetic energy k and the energy dissipation rate ε. These quantities are physically important because of the energy cascading mechanism [26]. From these quantities, we can form the turbulent length scale $l = k^{3/2}/\varepsilon$, time scale $\tau = k/\varepsilon$, and a dimensional quantity $\nu_t k^2/\varepsilon$, where ν_t is the turbulent kinematic viscosity.

The turbulent kinetic energy and the energy dissipation rate are expressed as,

$$k = \frac{\overline{u_1'^2} + \overline{u_2'^2} + \overline{u_3'^2}}{2} \tag{2-18}$$

$$\varepsilon = \nu \left[\overline{\frac{\partial u_i}{\partial x_j} + \frac{\partial u_j}{\partial x_i}}\right] \tag{2-19}$$

We shall now write the transport equations for k and ε in the context of cavitating flows with homogeneous single-fluid method. In this, the density that is to be used in the transport equation shall be the mixture density ρ_{mix}

$$\overbrace{\frac{\partial\left(\rho_{mix}k\right)}{\partial t}}^{\text{Rate of k change}} + \overbrace{\frac{\partial\left(\rho_{mix}\,u_j\,k\right)}{\partial x_j}}^{\text{Convective transport}} = \underbrace{\frac{\partial}{\partial x_j}\left[\left(\mu + \frac{\mu_t}{\sigma_k}\right)\frac{\partial k}{\partial x_j}\right]}_{\text{Diffusive transport}} + \underbrace{P_t}_{\substack{\text{Turbulence}\\ \text{production}\\ \text{rate}}} - \underbrace{\rho_{mix}\,\varepsilon}_{\substack{\text{Dissipation}\\ \text{Rate}}} \tag{2-20}$$

$$\frac{\partial\left(\rho_{mix}\varepsilon\right)}{\partial t} + \frac{\partial\left(\rho_{mix}\,u_j\,\varepsilon\right)}{\partial x_j} = \frac{\partial}{\partial x_j}\left[\left(\mu + \frac{\mu_t}{\sigma_\varepsilon}\right)\frac{\partial k}{\partial x_j}\right] + C_{\varepsilon 1}\frac{\varepsilon}{k}P_t - C_{\varepsilon 2}\,\frac{\varepsilon^2}{k}\,\rho_{mix} \tag{2-21}$$

The turbulence production term P_t is expressed as,

$$P_t = -\overline{\rho_{mix}\, u'_i u'_j}\frac{\partial u_i}{\partial x_j} \tag{2-22}$$

$$\overline{\rho_{mix}\, u'_i u'_j} = -\frac{2\,\rho_{mix}\,\delta_{i,j}}{3} + \mu_t\left[\frac{\partial \bar{u}_i}{\partial x_j} + \frac{\partial \bar{u}_j}{\partial x_i}\right] \tag{2-23}$$

$$\mu_t = \frac{\rho_{mix} C_\mu\, k^2}{\varepsilon};\;\; C_\mu = 0.09 \tag{2-24}$$

Here, $C_{\varepsilon 1}$, $C_{\varepsilon 2}$, σ_k, σ_ε, and C_μ are constants. The values of these constants listed in Utturkar et al [11] are shown in table 2-3.

Author	$C_{\varepsilon 1}$	$C_{\varepsilon 2}$	σ_k	σ_ε
Launder et al [45]	1.44	1.92	1.3	1.0
Shyy et al [46]	$1.15 + 0.25\frac{P_t}{\varepsilon}$	1.9	1.15	0.89
Kunz et al [41]	$1.15 + 0.25\frac{P_t}{\varepsilon}$	$1.45{+}0.45\frac{P_t}{\varepsilon}$	0.8927	1.15
Johansen et al [47]	1.44	1.92	1.3	1.0
	$\mu_t = \frac{\rho_{mix} C_\mu\, k^2}{\varepsilon} F;\; F = Min\left[1, C_\Delta \frac{\Delta\varepsilon}{k^{1.5}}\right]$	$C_\Delta = 1$		

Table 2-3: The constants of the $k-\varepsilon$ model are given below. Launder and Spalding [45] calculated these for shear flows. The values by Shyy et al [46] account for the non-equilibrium effects by introducing a small turbulent time scale in $C_{\varepsilon 1}$. Kunz et al [41] also account for the non-equlibrium effects by adding a turbulent time scale in $C_{\varepsilon 1}$ and $C_{\varepsilon 2}$. Johansen et al [47] use the same values as that of Launder and Spalding but use a filter function F, which depends upon the filtersize Δ, in the turbulent viscosity.

The standard $k-\varepsilon$ model assumes equilibrium conditions for the turbulent kinetic energy and its dissipation rate and the model constants are calculated for such conditions [26]. However, in the case of recirculating and rotating flows, the equilibrium between turbulent production and dissipation is not maintained. Shyy et al [46] and Kunz et al [41] have accounted for the non-equilibrium effects in the flow and have modified the constants. Johansen et al [47] use a filter based method and apply a filter for the turbulent viscosity (although they retain the constant values from Launder and Spalding [45]) because the standard $k-\varepsilon$ model over predicts the turbulent viscosity. For coarse grids, the Launder Spalding model is recovered, and the filter function F is set to 1 in the near wall region to model the shear layer. However, in the far field region, the solution is computed directly with $\mu_t \approx 0$ when the filter size is able to address the turbulent length scale. This filter based model produces a significant amount of unsteady characteristics while simulating a cavitating flow around a hydrofoil [48].

Some of the advantages of $k-\varepsilon$ model are its relatively simple implementation and numerically stable calculations. It is also a model which is widely validated. The disadvantages of this model are that it poorly predicts swirling and rotating flows, flows with strong separation, unconfined flows, and fully developed flows in non-circular ducts. It is valid only for fully developed turbulent flows and performs poorly in prediction transitional and developing flows.

Although it is sufficiently accurate for simple flow problems, it is quite inaccurate when it comes to complex flow patterns owing to the turbulent viscosity hypothesis and the inaccuracy of the ε equation. However, the accuracy of the model, depending upon the flow problem, can be improved by adjusting the model constants.

2-3-2 Re-Normalisation Group $k-\varepsilon$ model

One of the improvements made to the $k-\varepsilon$ model is called the Re-Normalisation Group $k-\varepsilon$ model. In this model, there is an additional term in the ε equation for the interaction between turbulence dissipation and mean shear.

One of the major criticisms of the $k-\varepsilon$ model is that it is not derived from the Navier-Stokes equations in any systematic fashion. Yakhot et al [49] applied Renormalization Group (RNG) methods to derive the $k-\varepsilon$ equations. In this approach, an expansion is made about an equilibrium state with known Gaussian statistics using the correspondence principle that the effects of the mean strains can be represented by a random force. Bands of high wave numbers (small scales) are systematically removed and space is rescaled in a manner analogous to that used in phase transitions. The successive removal of larger scales ultimately leads to a different formulation from the $k-\varepsilon$. It includes terms for

- Interaction between turbulence dissipation and mean shear in ε equation.
- The effect of swirl on turbulence.
- Analytical formula for turbulent Prandtl number.
- Differential formula for effective viscosity.

It also results in improved predictions for high streamline curvature and strain rate, transitional and separated flows, wall heat and mass transfer, and time dependent flows with large scale motions such as vortex shedding.

$$\frac{\partial\left(\rho_{mix}k\right)}{\partial t}+\frac{\partial\left(\rho_{mix}\,u_j\,k\right)}{\partial x_j}=\frac{\partial}{\partial x_j}\left[\left(\mu+\frac{\mu_t}{\sigma_k}\right)\frac{\partial k}{\partial x_j}\right]+P_t-\rho_{mix}\,\varepsilon \tag{2-25}$$

$$\frac{\partial\left(\rho_{mix}\varepsilon\right)}{\partial t}+\frac{\partial\left(\rho_{mix}\,u_j\,\varepsilon\right)}{\partial x_j}=\frac{\partial}{\partial x_j}\left[\left(\mu+\frac{\mu_t}{\sigma_\varepsilon}\right)\frac{\partial \varepsilon}{\partial x_j}\right]+C_{\varepsilon 1}\frac{\varepsilon}{k}P_t-C^*_{\varepsilon 2}\,\frac{\varepsilon^2}{k}\,\rho_{mix} \tag{2-26}$$

Where,

$$P_t = -\overline{\rho_{mix}\, u'_i u'_j} \frac{\partial u_i}{\partial x_j}; \qquad \overline{\rho_{mix}\, u'_i u'_j} = -\frac{2\,\rho_{mix}\,\delta_{i,j}}{3} + \mu_t \left[\frac{\partial \bar{u}_i}{\partial x_j} + \frac{\partial \bar{u}_j}{\partial x_i}\right];$$

$$\mu_t = \frac{\rho_{mix} C_\mu\, k^2}{\varepsilon}; \qquad C^*_{\varepsilon 2} = C_{\varepsilon 2} + \frac{C_\mu\, \eta^3\, \left(1 - {}^{\eta}/_{\eta_0}\right)}{1 + \beta\, \eta^3}; \qquad \eta = \frac{Sk}{\varepsilon};$$

$$S = \sqrt{2\, S_{ij}\, S_{ij}}; \qquad S_{ij} = \frac{1}{2}\left[\frac{\partial u_i}{\partial x_j} + \frac{\partial u_j}{\partial x_i}\right]$$

Here, the constants are $C_\mu = 0.0845$, $C_{\varepsilon 1} = 1.42$, $C_{\varepsilon 2} = 1.68$, $\sigma_k = 0.7194$, $\sigma_\varepsilon = 0.7194$, $\eta_0 = 4.38$, and $\beta = 0.012$

The advantage of this model is that it offers improved predictions for rotating cavities, high streamline curvature and strain rate, and transitional flows. However, for the prediction of vortex evolution, it doesn't perform better than the standard $k - \varepsilon$ model.

2-3-3 The $k - \omega$ model

The $k - \omega$ model, first proposed by Wilcox [50] is a two equation model and solves for the turbulent kinetic energy k and the dissipation rate per unit kinetic energy or specific dissipation ω. The equation for k is a modified version of the k equation in the $k - \varepsilon$ model. This model takes into account the history effects like convection and diffusion of turbulent kinetic energy.

$$\frac{\partial\left(\rho_{mix} k\right)}{\partial t} + \frac{\partial\left(\rho_{mix} k\, u_j\right)}{\partial x_j} = P_t - \rho_{mix}\, \beta^* k\, \omega + \frac{\partial}{\partial x_j}\left[\left(\mu + \frac{\mu_t}{\sigma_k}\right)\frac{\partial k}{\partial x_j}\right] \tag{2-27}$$

$$\frac{\partial\left(\rho_{mix}\, \omega\right)}{\partial t} + \frac{\partial\left(\rho_{mix}\, \omega\ u_j\right)}{\partial x_j} = \alpha\frac{\omega}{k} P_t - \rho_{mix}\, \beta\omega^2 + \frac{\partial}{\partial x_j}\left[\left(\mu + \frac{\mu_t}{\sigma_\omega}\right)\frac{\partial \omega}{\partial x_j}\right] \tag{2-28}$$

Where, the constants $\alpha = 0.553$, $\beta^* = 0.09$, $\beta = 0.075$, $\sigma_k = 2.0$, and $\sigma_\omega = 2.0$; with the turbulent viscosity modelled as,

$$\mu_t = \rho_{mix} \frac{k}{\omega} \tag{2-29}$$

The modified formulation of the $k - \omega$ model has the same equations for k and ω but the constants are changed.

$$\beta = \beta_0 f_\beta;\ \beta^* = \beta^*_0 f_{\beta^*};\ f_\beta = \frac{1 + 70\chi_\omega}{1 + 80\chi_\omega};\ \chi_\omega = \left|\frac{\Omega_{ij}\Omega_{jk}S_{ki}}{\left(\beta^*_0\omega\right)^3}\right|;\ \alpha = 0.52;\ \beta_0 = 0.072;\ \beta^*_0 = 0.09;$$

$$f_{\beta^*} = \left\{\ 1,\quad \chi_k \leqslant 0; \frac{1 + 680\chi_k^2}{1 + 80\chi_k^2},\quad \chi_k > 0\ \right. ; \qquad \chi_k \equiv \frac{1}{\omega^3}\frac{\partial k}{\partial x_j}\frac{\partial \omega}{\partial x_j}; \qquad \varepsilon = \beta^*\omega k; \qquad l = \frac{\sqrt{k}}{\omega};$$

$$\Omega_{jk} \equiv \frac{1}{2}\left(\frac{\partial u_k}{\partial x_j} - \frac{\partial u_j}{\partial x_k}\right);\ \Omega_{ij} \equiv \frac{1}{2}\left(\frac{\partial u_j}{\partial x_i} - \frac{\partial u_i}{\partial x_j}\right);\ S_{ki} = \frac{1}{2}\left[\frac{\partial u_k}{\partial x_i} + \frac{\partial u_i}{\partial x_k}\right];$$

Here, l is the turbulent length scale and ε is the energy dissipation rate. The $k-\omega$ model is superior to the $k-\varepsilon$ in primarily two ways: the viscous-wall treatment and for the accounting of streamwise pressure gradients [26]. It allows for more accurate near wall treatment with an automatic switch from wall models to low Reynolds number formulation based on grid spacing. It predicts flow transitions well and has options to account for free shear and compressible flows.

2-3-4 SST $k-\omega$ model

The Shear Stress Transport (SST) $k-\omega$ is a two equation model which serves as a combination of $k-\varepsilon$ and $k-\omega$ models. It was first proposed by Menter in 1994 to deal with strong freestream sensitivity of $k-\omega$ model and to improve predictions under strong pressure gradients. He then proposed a modified model in 2003. It uses the $k-\varepsilon$ formulation in the free stream region that is outside the boundary layer and uses the $k-\omega$ formulation inside the boundary layer. This combines the best of both worlds and avoids the $k-\omega$ problem of being too sensitive to the inlet free-stream turbulence properties and the $k-\varepsilon$ problem of inability to simulate the turbulent kinetic energy in the near wall region (in the viscous sub-layer). It behaves well in adverse pressure gradients and separating flows. Also, it can be used as a low Reynolds number turbulence model without any extra damping functions. However, it produces excessive turbulence in the regions with normal strain. These regions include stagnation regions and strong acceleration regions.

$$\frac{\partial(\rho_{mix}k)}{\partial t}+\frac{\partial(\rho_{mix}u_jk)}{\partial x_j}=P-\beta^*\rho_{mix}\omega k+\frac{\partial}{\partial x_j}\left[(\mu+\sigma_k\mu_t)\frac{\partial k}{\partial x_j}\right] \tag{2-30}$$

$$\frac{\partial(\rho_{mix}\omega)}{\partial t}+\frac{\partial(\rho_{mix}u_j\omega)}{\partial x_j}=\frac{\alpha}{\nu_t}P-\beta\rho_{mix}\omega^2+\frac{\partial}{\partial x_j}\left[(\mu+\sigma_\omega\mu_t)\frac{\partial\omega}{\partial x_j}\right]+2(1-F_1)\frac{\rho_{mix}\sigma_{\omega 2}}{\omega}\frac{\partial k}{\partial x_j}\frac{\partial\omega}{\partial x_j} \tag{2-31}$$

Where the turbulent eddy viscosity μ_t and production P are given by,

$$\mu_t=\frac{\rho_{mix}a_1k}{\max(a_1\omega,\Omega F_2)} \tag{2-32}$$

$$P=\left[\mu_t\left(2S_{ij}-\frac{2}{3}\frac{\partial u_k}{\partial x_k}\delta_{ij}\right)-\frac{2}{3}\rho_{mix}k\delta_{ij}\right]\frac{\partial u_i}{\partial x_j} \tag{2-33}$$

$$S_{ij}=\frac{1}{2}\left(\frac{\partial u_i}{\partial x_j}+\frac{\partial u_j}{\partial x_i}\right)$$

The function F_2 and another function F_1 are blending functions. The parameter α in the ω equation is expressed as,

$$\alpha=F_1\alpha_1+(1-F_1)\alpha_2 \tag{2-34}$$

Here, α_1 and α_2 are constants. All other additional functions are given by,

$$F_1 = \tanh\left(\arg_1^4\right); \qquad F_2 = \tanh\left(\arg_2^2\right)$$

$$\arg_1 = \min\left[\max\left(\frac{\sqrt{k}}{\beta^*\omega d}, \frac{500^{mu}/_{\rho_{mix}}}{d^2\omega}\right), \frac{4\rho_{mix}\sigma_{\omega 2}k}{\mathrm{CD}_{k\omega}d^2}\right]$$

$$\mathrm{CD}_{k\omega} = \max\left(2\rho_{mix}\sigma_{\omega 2}\frac{1}{\omega}\frac{\partial k}{\partial x_j}\frac{\partial \omega}{\partial x_j}, 10^{-20}\right)$$

$$\arg_2 = \max\left(2\frac{\sqrt{k}}{\beta^*\omega d}, \frac{500^{mu}/_{\rho_{mix}}}{d^2\omega}\right)$$

$$\Omega = \sqrt{2\Omega_{ij}\Omega_{ij}} \qquad \Omega_{ij} = \frac{1}{2}\left(\frac{\partial u_i}{\partial x_j} - \frac{\partial u_j}{\partial x_i}\right)$$

Production limiter on the k equation takes the form,$P_k = \min(P, 20\beta^*\rho_{mix}\omega k)$.

The constants in these equations are given by,

$$\alpha_1 = \frac{\beta_1}{\beta^*} - \frac{\sigma_{\omega 1}\kappa^2}{\sqrt{\beta^*}} \qquad \alpha_2 = \frac{\beta_2}{\beta^*} - \frac{\sigma_{\omega 2}\kappa^2}{\sqrt{\beta^*}}$$

$$\sigma_{k1} = 0.85 \qquad \sigma_{\omega 1} = 0.5 \qquad \beta_1 = 0.075 \qquad \sigma_{k2} = 1.0 \qquad \sigma_{\omega 2} = 0.856$$

$$\beta_2 = 0.0828 \qquad \beta^* = 0.09 \qquad \kappa = 0.41 \qquad a_1 = 0.31$$

The nearest distance to the wall is given by d; the SST calibration parameters are σ_{k1}, $\sigma_{\omega 1}$, σ_{k2}, $\sigma_{\omega 2}$, β_1, β_2, β^*, κ , and a_1

The SST model puts a limitation on the shear stress when under adverse pressure gradients. It accounts for the turbulent shear stress transport and predicts accurately the onset and extent of separation. It is original form, the SST model does not account for compressibility. Also, since it is highly dependent on the wall distance, it poorly predicts free shear flows. It also underperforms in accounting for rotation and high strain rates. However, Smirnov and Menter [51] proposed a correction for rotation and curvilinear effects. This correction is primarily applied for flows in turbomachinery.

An empirical function multiplies the production term P in both k and ω equations. That function is given by,

$$f_{r1} = \max\left[\min\left(f_{rotation}, 1.25\right), 0.0\right] \tag{2-35}$$

$$f_{rotation} = (1 + c_{r1})\frac{2r^*}{1 + r^*}\left[1 - c_{r3}\tan^{-1}(c_{r2}\hat{r})\right] - c_{r1} \tag{2-36}$$

A reference frame is defined, which may be rotating with a rotation rate Ω^r, and all variables and their derivatives are defined according to this rotating frame.

$$
\begin{gathered}
r^{*} = {}^{S}\!/_{\Omega} \qquad c_{r1} = 1.0 \qquad c_{r2} = 2.0 \qquad c_{r3} = 1.0 \\
\hat{r} = \frac{2W_{ik}S_{jk}}{WD^{3}} \left(\frac{DS_{ij}}{Dt} + \left(\varepsilon_{imn} S_{jn} + \varepsilon_{jmn} S_{in} \right) \Omega_{m}^{r} \right) \\
S_{ij} = \frac{1}{2} \left(\frac{\partial u_i}{\partial x_j} + \frac{\partial u_j}{\partial x_i} \right) \qquad \Omega_{ij} = \frac{1}{2} \left[\left(\frac{\partial u_i}{\partial x_j} - \frac{\partial u_j}{\partial x_i} \right) + 2\varepsilon_{mji} \Omega_{m}^{r} \right] \\
\Omega = \sqrt{2\Omega_{ij}\Omega_{ij}} \qquad S^{2} = 2S_{ij}S_{ij} \qquad D^{2} = \max\left(S^{2}, 0.09\omega^{2} \right)
\end{gathered}
$$

Here, ${}^{DS_{ij}}\!/_{Dt}$ denotes the components of the Langevin derivative of the strain rate tensor, and $\Omega^{r} = 0$ when the whole reference frame is not rotating.

2-3-5 Reynolds Stress Model

The Reynolds Stress Model (RSM) is a higher order closure turbulence model in which the model transport equations are solved for individual Reynolds stresses in the RANS equation (2-17) and for the dissipation of turbulent kinetic energy ε or the specific dissipation ω or any other quantity from which turbulent time scales and length scales can be obtained. In total, there are 7 extra equations used to model these. This model is also called the second order closure model.

Owing to the presence of these extra equations, the need for Boussinesq hypothesis for the turbulent eddy viscosity is no longer present. In the previous sections on two-equation turbulence models, we have seen that the turbulent eddy viscosity is at times over-predicted. This causes the model to yield non-physical results. Since this is no longer needed, the RSM is devoid of such inaccuracies. Also, the two equation models are unable to account for the streamline curvature, rotational strains, body force effects, and the strong non-local and history effects of Reynolds stress anisotropies [52].

The RSM is based on the Reynolds Stress Transport equation. This model accounts for the strong non-local and history effects of the Reynolds stress anisotropies. The Reynolds Stress Transport equation is represented as

$$
\underbrace{\frac{\partial \left(\rho \, \overline{u_i' u_j'} \right)}{\partial t}}_{\text{Rate of change}} + \underbrace{C_{ij}}_{\substack{\text{Convective}\\ \text{Transport}}} = \underbrace{P_{ij}}_{\text{Production}} + \underbrace{D_{ij}}_{\substack{\text{Diffusive}\\ \text{Transport}}} - \underbrace{\varepsilon_{ij}}_{\substack{\text{Dissipation}\\ \text{Rate}}} + \underbrace{\Pi_{ij}}_{\substack{\text{Transport due}\\ \text{to Pressure-Strain}\\ \text{Interaction}}} + \underbrace{\Omega_{ij}}_{\substack{\text{Transport due}\\ \text{System Rotation}}} \tag{2-37}
$$

The convective transport term and the production terms, which include stress and buoyancy production, automatically adjust themselves to the rotation of the system and the streamline curvature in turbulent flows. Although the RSM is theoretically a simple approach, we still have to model the diffusion transport term D_{ij}, the pressure-strain interaction term Π_{ij}, and the dissipation rate term ε_{ij}.

The diffusion transport term D_{ij}, being a third order diffusion correlation, is modelled using a gradient transport hypothesis. That is, the rate of transport of Reynolds stresses by diffusion is proportional to the gradients of Reynolds stresses. However, this is based on the assumption that there are discrete separation scales between the mean and fluctuating scales at the second order Reynolds stress tensor. The pressure-strain interaction term Π_{ij} is the most important term to model. This term, along with the dissipation rate term ε_{ij}, is modelled based on homogeneous turbulence. In this, the deviation from isotropy is assumed to be small enough.

The convective term C_{ij} is given by,

$$C_{ij} = \frac{\partial}{\partial x_k}\left(\rho_{mix} u_k \overline{u'_i u'_j}\right) \tag{2-38}$$

The production term P_{ij} has two parts, a stress production term and a buoyancy production term. They are given by,

$$(P_{ij})_{stress} = \rho_{mix}\left(\overline{u'_i u'_k}\frac{\partial u_j}{\partial x_k} + \overline{u'_j u'_k}\frac{\partial u_i}{\partial x_k}\right) \tag{2-39}$$

$$(P_{ij})_{buoyancy} = \rho_{mix}\beta\left(g_i\overline{u'_j\theta} + g_j\overline{u'_i\theta}\right) \tag{2-40}$$

Here, β is the volumetric expansion and g is the acceleration due to gravity.

The diffusion term D_{ij} is expressed as,

$$D_{ij} = \frac{\partial}{\partial x_k}\left(\frac{\mu_t}{\sigma}\frac{\partial\left(\overline{u'_i u'_j}\right)}{\partial x_k}\right); \qquad \mu_t = \rho_{mix} C_\mu \frac{k^2}{\varepsilon}; \qquad C_\mu = 0.09; \qquad \sigma = 1 \tag{2-41}$$

This formula is implemented in wide range of CFD codes [53].

The dissipation rate ε_{ij} is modelled assuming isotropy of small dissipative eddies. It is set a value such that only the normal Reynolds stresses are affected and only in an equal measure.

$$\varepsilon_{ij} = \frac{2}{3}\varepsilon\,\delta_{ij} \tag{2-42}$$

Here, ε is the dissipation rate of the turbulent kinetic energy described by the equation,

$$\frac{\partial(\rho_{mix}\,\varepsilon)}{\partial t} + \frac{\partial(\rho_{mix}\,u_j\varepsilon)}{\partial x_j} = \frac{\partial}{\partial x_j}\left[C_\varepsilon\,\rho_{mix}\,\overline{u'_j u'_k}\,\frac{k}{\varepsilon}\frac{\partial\varepsilon}{\partial x_k}\right] + \frac{\varepsilon}{k}\left(C_{\varepsilon 1}P_t - C_{\varepsilon 2}\,\rho_{mix}\,\varepsilon\right)P_t \tag{2-43}$$

$$P_t = -\rho_{mix}\,\overline{u'_i u'_j}\,\frac{\partial u_i}{\partial x_j}$$

Where $C_\varepsilon = 0.18$, $C_{\varepsilon 1} = 1.44$, $C_{\varepsilon 2} = 1.92$

The Reynolds stresses are affected by the pressure-strain interactions by two main physical processes. The fluctuation of pressure of an eddy due to its interaction with another eddy and the fluctuation in pressure of an eddy due to its interaction with a region having a different mean velocity. Owing to these interactions and pressure fluctuations, there is a redistribution of energy among the Reynolds stresses. This makes them more isotropic and there is a reduction in Reynolds shear stresses. The treatment of wall flows also plays a major role in affecting the Reynolds stresses. The wall effects increase the anisotropy of the Reynolds stresses and reduce the Reynolds shear stresses [54] [53].

Correction terms are required to account for influence of the wall proximity to the pressure-strain terms [53]. The wall damping functions are different from those applied in the $k - \varepsilon$ model and should be used irrespective of the Reynolds number of the mean flow.

The pressure strain correlation, in its simplest form, which accounts for all the effects are given in Launder et al [54]

$$\Pi_{ij} = -C_1 \rho_{mix} \frac{\varepsilon}{k} \left(\overline{u'_i u'_j} - \frac{2}{3} k \delta_{ij} \right) - C_2 \left(\rho_{mix} \left(\overline{u'_i u'_k} \frac{\partial u_j}{\partial x_k} + \overline{u'_j u'_k} \frac{\partial u_i}{\partial x_k} \right) - \frac{2}{3} P \delta_{ij} \right) \tag{2-44}$$

Where, $C_1 = 1.8$; $C_2 = 0.6$ and P is the pressure

The rotation term Ω_{ij} is given by

$$\Omega_{ij} = -2 \rho_{mix} \, \omega_k \left(\overline{u'_j u'_m} e_{ikm} + \overline{u'_i u'_m} e_{jkm} \right) \tag{2-45}$$

Here, the quantity ω_k is the rotation vector and e_{ijk} is an alternator. The quantity $e_{ijk} =$ 1 if the i,j, and k are in cyclic order, $e_{ijk} =$ -1 if they are in anti-cyclic order, and $e_{ijk} = 0$ when there are two same indices. The turbulent kinetic energy required in the corresponding equations is derived from equation (2-18).

The exact form of the Reynolds stress transport equations with the appropriate models for convective transport, turbulent and molecular diffusion, stress and buoyancy production, pressure rate-of-strain correlation, and transport due to rotation terms is:

$$\begin{aligned}\frac{\partial}{\partial t}\left(\rho_{mix}\overline{u'_i u'_j}\right)+\overbrace{\frac{\partial}{\partial x_k}\left(\rho_{mix}u_k\overline{u'_i u'_j}\right)}^{\text{Convection}} &= \overbrace{-\frac{\partial}{\partial x_k}\left[\rho_{mix}\overline{u'_i u'_j u'_k}+\overline{p'\left(\delta_{kj}u'_i+\delta_{ik}u'_j\right)}\right]}^{\text{Turbulent Diffusion}}+\overbrace{\frac{\partial}{\partial x_k}\left[\mu\frac{\partial}{\partial x_k}\left(\overline{u'_i u'_j}\right)\right]}^{\text{Molecular Diffusion}}\\
&\quad \underbrace{-\rho_{mix}\left(\overline{u'_i u'_k}\frac{\partial u_j}{\partial x_k}+\overline{u'_j u'_k}\frac{\partial u_i}{\partial x_k}\right)}_{\text{Stress Production}}\underbrace{-\rho_{mix}\beta\left(g_i\overline{u'_j\theta}+g_j\overline{u'_i\theta}\right)}_{\text{Buoyancy Production}}\\
&\quad \underbrace{+\overline{p'\left(\frac{\partial u'_i}{\partial x_j}+\frac{\partial u'_j}{\partial x_i}\right)}}_{\text{Pressure rate-of-strain}}\underbrace{-2\mu\overline{\frac{\partial u'_i}{\partial x_k}\frac{\partial u'_j}{\partial x_k}}}_{\text{Dissipation}}\\
&\quad \underbrace{-2\rho_{mix}\,\omega_k\left(\overline{u'_j u'_m}e_{ikm}+\overline{u'_i u'_m}e_{jkm}\right)}_{\text{Production due to rotation}} \qquad (2\text{-}46)\end{aligned}$$

The modelled form is,

$$\begin{aligned}\frac{\partial}{\partial t}\left(\rho_{mix}\overline{u'_i u'_j}\right)+\frac{\partial}{\partial x_k}\left(\rho_{mix}u_k\overline{u'_i u'_j}\right) &= \frac{\partial}{\partial x_k}\left(\frac{\mu_t}{\sigma}\frac{\partial\left(\overline{u'_i u'_j}\right)}{\partial x_k}\right)+\rho_{mix}\left(\overline{u'_i u'_k}\frac{\partial u_j}{\partial x_k}+\overline{u'_j u'_k}\frac{\partial u_i}{\partial x_k}\right)\\
&\quad +\rho_{mix}\beta\left(g_i\overline{u'_j\theta}+g_j\overline{u'_i\theta}\right)-C_1\rho_{mix}\frac{\varepsilon}{k}\left(\overline{u'_i u'_j}-\frac{2}{3}k\delta_{ij}\right)\\
&\quad -C_2\left(\rho_{mix}\left(\overline{u'_i u'_k}\frac{\partial u_j}{\partial x_k}+\overline{u'_j u'_k}\frac{\partial u_i}{\partial x_k}\right)-\frac{2}{3}P\delta_{ij}\right)\\
&\quad -\frac{2}{3}\varepsilon\,\delta_{ij}-2\rho_{mix}\,\omega_k\left(\overline{u'_j u'_m}e_{ikm}+\overline{u'_i u'_m}e_{jkm}\right) \qquad (2\text{-}47)\end{aligned}$$

2-3-6 Multiphase Flows

Multiphase flows are characterised by the presence of multiple fluids or single fluids with multiple phases having different density, viscosity, and other thermofluid properties. The interface boundary between the two phases is mobile and possibly stochastic.

In a two-phase flow, there is a continuous or a carrier phase which is continuously connected. Then there is the dispersed phase which is embedded in the carrier phase which has particle like characteristics. In a cavitating flow, the liquid phase is the carrier phase and the dispersed phase is the vapour phase (bubbles). When there are very few bubbles in the main flow such that dispersed phase has no significant effect on the carrier phase, it is called one-way coupling. When there are enough bubbles such that there is a momentum exchange between the dispersed and carrier phases which alters the dynamics of the carrier phase, it is called two-way coupling. In the case of a high density flow, when there is a significant momentum interchange between the dispersed and carrier phases, we call it the four-way coupling.

In this section, the primary focus is on two-phase coupling. Mashayek et al [55] provided an analytical description of two-phase turbulent flows. Cokljat et al [56] developed a Reynolds

Stress Model for Eulerian multiphase flows and Beishuizen et al [57] evaluated a modified RSM for turbulent dispersed two-phase flows with two-way coupling.

The momentum exchange that happens between the carrier and the dispersed phase appears as a source term in the Navier-Stokes equations. The mean momentum equation, the Reynolds stress equation, and the dissipation equations can be derived from averaging the multiphase Navier-Stokes equations. The two-way coupling terms in these equations are the ones which describe the effect of dispersed phase on the carrier phase.

The continuity and momentum equations for the continuous phase are,

$$\frac{\partial \left(\rho \zeta\right)}{\partial t} + \frac{\partial \left(\rho u_k \zeta\right)}{\partial x_k} = 0 \tag{2-48}$$

$$\frac{\partial \left(\rho u_i \zeta\right)}{\partial t} + \frac{\partial}{\partial x_k} \left(\rho u_i u_k \zeta\right) = -\frac{\partial \left(p \zeta\right)}{\partial x_i} + \frac{\partial \left(\tau_{ij} \zeta\right)}{\partial x_k} + \left(\rho \zeta\right) g_i + S_{u_i} \tag{2-49}$$

$$\tau_{ij}\zeta = \mu\zeta \left[\left(\frac{\partial u_i \zeta}{\partial x_j} + \frac{\partial u_j \zeta}{\partial x_i} \right) - \frac{2}{3} \frac{\partial u_k \zeta}{\partial x_k} \delta_{ij} \right] \tag{2-50}$$

In the above equation, the $\zeta(x,t)$ function denotes the presence of a continuous phase. $\zeta = 1$ in the presence of a continuous phase at (x,t) and $\zeta = 0$ in the absence of the continuous phase. The term S_{u_i} is the two-way coupling source term. The stress at the interface serves as the source for the momentum exchange.

To obtain the mean flow equations we have to obtain a Favre average of the equations (2-48) and (2-49). The mean flow equations are expressed as:

$$\frac{\partial \zeta \bar{\rho}}{\partial t} + \frac{\partial \zeta \bar{\rho} \tilde{u}_k}{\partial x_k} = 0 \tag{2-51}$$

$$\frac{\partial \zeta \bar{\rho} \tilde{u}_i}{\partial t} + \frac{\partial \zeta \bar{\rho} \tilde{u}_k \tilde{u}_i}{\partial x_k} = -\frac{\partial \zeta \bar{\rho} \widetilde{u_i'' u''_k}}{\partial x_k} - \zeta \frac{\partial \bar{p}}{\partial x_i} + \zeta \frac{\partial \overline{\tau_{ik}}}{\partial x_k} + \langle S_{u_i} \rangle \tag{2-52}$$

where, $\langle S_{u_i} \rangle$ is the averaged source term and $\bar{\tau}_{ik}$ is the time averaged Reynolds stress term. It is often attributed to the drag force that occurs at the interface. The quantities bearing an overbar superscript are Reynolds averaged and the '$\sim$' superscript denotes Favre averaging.

In the case of a two-phase cavitating flow, the quantity ζ is replaced with the quantity α which is the volume fraction of the liquid (continuous phase).

The Reynolds stress transport equation for the continuous phase is then expressed as,

$$\frac{\partial}{\partial t} \left(\alpha \bar{\rho} \widetilde{u''_i u''_j} \right) + \frac{\partial}{\partial x_k} \left(\alpha \bar{\rho} \widetilde{u''_i u''_j} \, \tilde{u}_k \right) = \alpha \left(P_{ij} + D_{ij} + \Pi_{ij} - E_{ij} \right) + \left\langle S_{u_i u_j} \right\rangle \tag{2-53}$$

Here,

$$P_{ij} = -\,\bar{\rho}\widetilde{u''_i u''_k}\frac{\partial \tilde{u}_j}{\partial x_k} - \,\bar{\rho}\widetilde{u''_j u''_k}\frac{\partial \tilde{u}_i}{\partial x_k} \tag{2-54}$$

$$D_{ij} = -\frac{\partial}{\partial x_k}\left[\bar{\rho}\widetilde{u''_i u''_j u''_k} - \overline{p' u''_i}\,\delta_{jk} - \overline{p' u''_j}\,\delta_{ik}\right] \tag{2-55}$$

$$\Pi_{ij} = \overline{p'\left(\frac{\partial u''_i}{\partial x_j} + \frac{\partial u''_j}{\partial x_i}\right)} \tag{2-56}$$

$$E_{ij} = \frac{2}{3}\bar{\rho}\varepsilon\delta_{ij} = \frac{2}{3}\overline{\left[\mu\frac{\partial u''_i}{\partial x_k}\frac{\partial u''_j}{\partial x_k}\right]} \tag{2-57}$$

$$\langle S_{u_i u_j}\rangle = \langle u''_{I,i} S_{u_j}\rangle + \langle u''_{I,j} S_{u_i}\rangle \tag{2-58}$$

The terms P_{ij}, D_{ij}, Π_{ij}, and E_{ij} are production, diffusion, pressure-dilation or pressure rate-of-strain correlation, and dissipation terms respectively. The quantity $u''_{I,i}$ is the velocity fluctuation at the interface. The source term for the two-way coupling is essentially a Stokes drag relation when there is no mass transfer between the two phases [55].

2-3-7 Turbulence modelling summary

The two-equation models are either applied as they are or certain modifications are applied to these models to predict cavitating flows. Some of those corrections are the Reboud correction which limits the value of turbulent eddy viscosity in order to prevent its over-prediction. The over-prediction of the eddy viscosity leads to the regeneration of stable cavities and prevention of formation of the re-entrant jet. The Menter Shear Stress Transport (SST) correction is applied to these models to model the flow in the viscous sublayer without any extra wall damping functions. The realisability correction is applied to correct for the stagnation point anomaly. However, no such corrections are made for Reynolds stress models.

Table 2-4: Turbulence models: Advantages and Disadvantages

Model	Advantages	Disadvantages
Standard $k-\varepsilon$	• Simple implementation • Computationally inexpensive • Widely validated • Suitable for mean flow calculations	• Valid only for fully turbulent flows • Numerical stiffness and instability in the viscous sublayer • Requires wall functions • Over-prediction of μ_t in highly strained flows and cavitating flows. • Poorly predicts: – Flows with streamline curvature – Rotational and swirling flows – Phasic interaction between turbulence and multiphase. – Flows with separation – Unconfined flows – Fully developed flows in non-circular ducts – Reynolds stress anisotropies – Body forces

RNG-$k-\varepsilon$	• Improved form of standard $k-\varepsilon$ wielding more advantages. • Improved predictions for – High streamline curvature – Transitional and separated flows – Wall and heat transfer – Time dependent flows with large scale motions	• Poor predictions for spreading of the round jet. • Same as that of $k-\varepsilon$ except for some improved predictions.
Wilcox $k-\omega$	• Superior performance for wall-bounded flows with an automatic switch from wall fuction to low Reynolds number formulation based on grid spacing. • Improved predictions for free shear flows and low-Re flows. • Suitable for complex boundary layer flows (ex. turbomachinery) with strong pressure gradients. • Also suitable for transitional flows	• Suffers from the drawbacks of eddy viscosity concept. • Predicts early transition in transitional flows. • Sensitive to adverse freestream pressure gradients. • In flows with separation, the separation is over-predicted and predicted early. • Requires a high mesh resolution near the wall.

SST model	• It is a combination of $k-\varepsilon$ (in freestream) and $k-\omega$ (near the wall). • Shares the advantages of $k-\varepsilon$ and $k-\omega$. • Puts a limit on shear stresses in the occurrence of large pressure gradients. • Accounts for turbulent shear stress transport and accurately predicts the onset and extent of flow separation under adverse pressure gradients. • Suitable for accurate boundary layer flows.	• Shares some of the drawbacks of $k-\varepsilon$ and $k-\omega$. • Does not include compressibility. • Poorly predicts free shear flows because of its dependency on wall distance. • Poor predictions for rotating flows and flows with sudden change in strain rate.
Reynolds Stress Model	• Physically, it is the most complete model • Accounts for non-local and history effects of the Reynolds stress tensor anisotropies, switling, rotation, streamline curvature, high strain rate and is devoid of isotropic eddy viscosity assumption. • Superior predictions of: – Swirling combustor flows. – Flows in turbomachinery. – Rotating flow passages and secondary flows. – Flows with separation. – Two-phase flows.	• High computational costs. • Implementation is not simple. • Momentum and turbulence equations are tightly coupled. • Shares modelling problems for ε with the $k-\varepsilon$ model and performs the same way as that in some problems.

With the listed advantages and disadvantages, we shall create a rough trade-off table. The trade-off table is constructed only for the turbulence models and not for the models for cavitation source terms. The primary requirement of a turbulence model is to model a physically representative cryogenic cavitating flow in a turbopump inducer. This flow will have turbulence-multiphase interactions and strong rotational body forces since the turbopump rotates at 20000-30000 rpm. The model should also be computationally feasible and relatively simple to implement. However, implementation of such a model is not simple and direct. The choice of the model heavily depends upon the application and the level of accuracy needed for flow modelling.

The essential trade-off criteria for the turbulence models are

- Simplicity of implementation
- Computational effort
- Physical accuracy
- Computational accuracy
- Computational stability

By simplicity of implementation, we mean the easiness with which the model equations are discretised and implemented in a computer code in order to model and simulate the flow. Computation effort means the computer memory, CPU power requirements, and the physical time taken for simulations. We desire less computational effort. Physical accuracy here means the ability to capture the actual physics of the problem. This would mean the ability to account for the anisotropies, rotation, multiphase regimes etc. We require very less approximations and assumptions, and very high predictive capability. The model should provide physically viable results. Computational accuracy would mean convergence of the model and production of 'accurate' results. Accuracy of a model is defined by its ability to reproduce experimental or DNS results of canonical flow problems. The approximate required accuracy for cavitation length predictions is 85-90% (the match between numerical and experimental results). Computational stability means the ability to obtain convergence of the solution without having any anomalous behaviour or numerical oscillations, and to avoid a 'blow-up' of the simulation which tends to non-physical results.

An approximate trade-off table is created by considering the advantages, disadvatanges, and the applicability of the turbulence models. It is represented in table 2-5

Models	Simplicity	Comp. Effort	Physical Accuracy	Comp. Accuracy	Comp. Stability
$k-\varepsilon$	Excellent	Excellent	Poor	Insufficient	Good
RNG $k-\varepsilon$	Excellent	Good	Insufficient	Sufficient	Good
$k-\omega$	Excellent	Good	Insufficient	Sufficient	Sufficient
$k-\omega$ SST	Good	Good	Sufficient	Good	Good
RSM	Sufficient	Sufficient	Excellent	Good	Good

Table 2-5: Simplified trade-off table for the turbulence models

From the trade-off table, we can say that the Reynolds Stress Model (RSM) has the best characteristics and capabilities to capture the actual physics of the problem. Although it has a few drawbacks in the fields of computational effort, it is the most viable model to physically represent the actual cavitating flow. Also, the standard formulations of $k-\varepsilon$, RNG-$k-\varepsilon$, and $k-\omega$ are not quite suitable for physically accurate modelling and simulation of cavitating flows, they can still be used to analyse such flows by employing the corrections for compressibility, eddy viscosity, shear stress transport, and realisability. This is purely because of their engineering applicability, i.e., the ability to produce the same solution in a repeatable fashion for engineering problems.

Right now, only the RANS based models are viable. It is very hard to perform Large Eddy Simulations and Direct Numerical Simulations of cavitating flows in turbopump because of the computational requirements such as memory, processing speed, and power.

Chapter 3

Analysis of influence of parameters

The goal of this chapter is to investigate the importance of the choice of turbulence models in modelling cavitating flows in cryogenic turbopump inducers. The effects of turbulence models and other critical parameters on the onset, size, and topology of cavitation are quantified and critically analysed. The quantities that are calculated and compared are length of the attached cavitation bubble, minimum coefficient of pressure, pressure contours, density contours, and liquid volume fraction contours.

To systematically investigate the turbulence modelling in cryogenic turbopumps, the geometry has to be simplified. Full 3D simulations of inducers are expensive and not very informative because there are multiple interactions and instabilities which are strongly coupled to one another. These effects are far too complex to be addressed together. The simulations are computationally expensive and produce large amounts of data which are hard to handle. Thus, the corresponding cavitating flow domains in an inducer are decomposed into simplified domains which are congruous with canonical cavitating flow problems. This isolates the different physical cavitation phenomena that occur in inducers.

Simplification and isolation inducer cavitating flow phenomena will help us in the following aspects:

- Cavitation in canonical flow problems is well understood and documented.
- The causes of certain flow behaviour can be tracked down easily and the uncertainty caused by unknown effects are eliminated.
- The transformation occurring in cavitation flow due to change in control parameters could be easily quantified and studied.
- Feasibility of computation increases.

The decomposition of inducer flow domains into simpler geometries resembling canonical flow problems is shown in figure 3-1. Four canonical cases are abstracted corresponding to the cavitation flow phenomena occurring in an inducer.

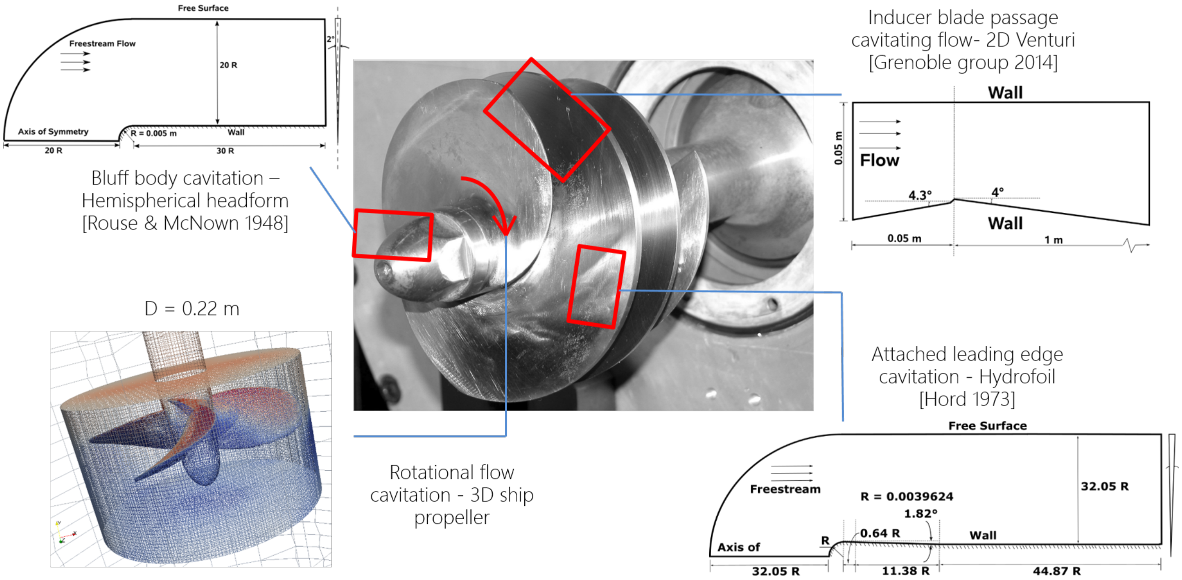

Figure 3-1: Simplification of the 3D inducer geometry into canonical flow problems. The four types are: 1. Bluff body cavitation at the inducer boss - hemispherical headform 2. Attached leading edge cavitation - hydrofoil 3. Inducer blade passage cavitating flow - 2D Venturi 4. Rotational flow cavitation - three-dimensional rotating canonical ship propeller.

- Bluff body cavitation : Flow over a hemispherical headform - Rouse and McNown (1948) [58]
  - The flow past a hemispherical headform occurs the front part (boss) of the inducer. This flow has zero-pressure gradient downstream of the flow and is similar to a cavitating flow past a bluff body. The canonical flow problem reflective of this type of flow has been investigated by Rouse and McNown (1948).
- Attached leading edge cavitation : Cryogenic flow over a hydrofoil - Hord (1973) [59]
  - This case deals with attached leading edge cavitation that is represented using a hydrofoil. The hydrofoil used is a symmetric hydrofoil that has been analysed by Hord (1973) [59]. This flow has a negative pressure gradient downstream due to the negative slope in the geometry. The default operating fluid is liquid Hydrogen.
- Cavitation in inducer blade passage : Cryogenic flow through a 2D Venturi (CREMHyG) - Grenoble Group (2014) [25]
  - This case deals with a cryogenic flow through a 2D Venturi which is representative of flows through inducer blade passages. Experimental investigation as well as numerical simulations of cryogenic cavitating flow through a 2D Venturi are carrioud out by the research group in CREMHyG (Centre de Recherche et d'Essai de Machines Hydrauliques de Grenoble) [25].
- Cavitation in rotating regimes : Three-dimensional rotating flow past a canonical ship propeller.

  - This case deals with a canonical ship propeller rotating at about 515 rpm. For this, we use a 3D simulation to understand how the choice of turbulence models affect the phase distribution when rotation is involved.

We have to establish baseline cases according to the aforementioned canonical cases to quantify and analyse the sensitivity of the assessed parameters such as cavitation length, onset distance, and the distributions of pressure, density, and liquid volume fraction due to changes in control parameters such as turbulence models, cavitation flow solver, operating fluid, Reynolds number, turbulence intensity, barotropic compressibility model, and cavitation source model.

The baseline cases have fixed parameters and the following parameters are changed from the baseline configuration.

- *Cavitation Flow Solver* : Two different solvers are used for the simulations: 1. A Barotropic Equation based Solver (BES) which solves for the pressure field and computes density by treating it as a function of pressure. 2. Transport Equation based Solver (TES) : a solver which uses a liquid volume fraction transport equation and computes the mixture density based on that. In OpenFOAM, the barotropic solver is implemented as cavitatingFoam and the tranport equation based solver is implemented as interPhaseChangeFoam. Thus, in the following sections, we use the abbreviation BES for the barotropic equation based solver and TES for the transport equation based solver.
  - *Barotropic Compressibility Model - BES* : The three types of compressibility models used are Wallis model, Chung model, and the Linear model along with the BES. These model formulations are discussed in section B-1-2. The variation in the results compared to the baseline configuration are studied.
  - *Cavitation Model - TES* : Three cavitation models are used along with TES. They are Merkle model [39], Kunz model [41], and Schnerr-Sauer model [36]. The effects of these models on cavitation is studied.
- *Turbulence models* : Multiple turbulence models are used to simulate the same flow and the variation in results are quantified and analysed. The turbulence models to be used are $k-\omega$ SST, $k-\omega$, $k-\epsilon$, Launder-Reece-Rodi Reynolds Stress Tensor Model, and RNG $k-\epsilon$
- *Reynolds number* : The effect of Reynolds number variation on the cavitation is studied. The Reynolds number is varied by changing the dynamic viscosity or the characteristic length scale of the problem.
- *Turbulence Intensity* : The effect of turbulence intensity on cavitation prediction is studied. This gives us some important information about turbulence-cavitation interaction.
- *Operating liquid* : For the cryogenic flows, the difference in cavitation size and onset are studied for fluids such as Liquid Hydrogen (LH2), Liquid Nitrogen (LN2), and Liquid Oxygen (LOX).

In the following sections, we analyse the influence of each of the control parameters in the canonical cavitating flow regimes. We then draw conclusions based on the results obtained.

3-1 Hemispherical headform : Bluff body cavitation

Experimental investigation of cavitation and pressure distributions on a flow over a hemispherical headform using water was first done in 1948 by Hunter Rouse and John S. McNown at State University of Iowa. Their work was primarily used for studying cavitation in submaries by the United States Navy. Velocity distribution, pressure distribution and cavitation over a 1-inch diameter hemispherical head with a cylindrical body is experimentally determined and plotted. The fluid used for the experiments is water and inlet velocity is varied to set the appropriate cavitation number. The ambient pressure used for the experiments was standard atmospheric pressure. This experimental investigation, using non-dimensionalised parameters, shall reflect the flow past a hemispherical headform in the front side of an inducer.

The numerical simulation case of the hemispherical headform is setup based on this experimental work. Since the experimental results are non-dimensional, the geometry of the case is modelled proportionally. The model is axisymmetric and the hemispherical headform has a radius (R) of 0.005 metres. The inlet of the entire domain is placed at a distance of $20R$ upstream of the hemispherical head (on the axis) and the outlet is placed at $30R$ downstream. The height of the domain is $20R$. Simulation in a 2D axisymmetric domain reduces the computation time and provides a good approximation of the real world flow domain (3D) [60]. The fluid used is water at a temperature (T_∞) of 298 K and an ambient pressure (P_∞) of 101325 N/m^2. The Reynolds number, 2.22×10^5, is defined using the diameter of the hemispherical headform and the freestream velocity. The reference parameters for simulations are tabulated in table 3-1

The simulations are carried out using open source CFD software, OpenFOAM. A velocity inlet condition is used with the inlet velocity and subsequent free stream velocity values being 19.84375 m/s. The free stream pressure is set to atmospheric pressure, i.e., 101325 Pa. The density of the freestream flow is set to 997.05 kg/m^3 based on the freestream pressure and the reference temperature 298 K. Figure 3-2 illustrates the domain size, the boundary conditions, and the mesh. The boundary conditions for turbulence parameters include: a turbulent intensity based kinetic energy inlet condition, which calculates the turbulent kinetic energy k according to the intensity I, and a turbulent mixing length scale based inlet condition for the the specific dissipation rate ω. The top flat surface is treated as a free surface (freestream BC), the outer arc is treated as the inlet region, and the hemispherical headform is treated as a wall. In order to create an axisymmetric profile, the domain is created using a wedge boundary condition and with an axis of symmetry. A no slip boundary condition is applied at the walls. Also, for k and ω, wall functions such as k-qR wall function and ω wall function are used respectively for the simulation. The pressure BC at the inlet is set as zero gradient and the density BC is fixed at 997.05 kg/m^3. At the freestream boundary, the velocity, pressure, and the density BCs are set as zero gradient. At the outlet, the velocity BC is set as zero gradient, and pressure and density BCs as fixed values with 101325 Pa and 997.05 kg/m^3 respectively.

In the following sections, optimal mesh resolution for analyses is first obtained by achieving convergence of predicted cavitation parameters. The optimal mesh shall require the best affordable computational effort for which the results are converged. After selecting an optimal mesh resolution, baseline cases are setup to analyse the influence of control parameters, mainly the turbulence model, on the cavitation parameters. The analysis of influence of turbulence

Parameter	Value
Radius, R [m]	0.005
Ambient Pressure, P_∞ [Pa]	101325
Cavitation No. σ [-]	0.5
Freestream Velocity, U_∞ [m/s]	19.84375
Freestream Density, ρ_∞ [kg/m^3]	997.05
Reynolds No, Re [-]	2.22×10^5
Liquid Dyn. Viscosity, μ_l [Pa-s]	8.899×10^{-4}
Vapour Dyn. Viscosity, μ_v [Pa-s]	9.8671×10^{-6}
Saturation Pressure, P_{sat} [Pa]	3171.8
Liquid Saturation Density, $\rho_{l,sat}$ [kg/m^3]	997.0
Vapour Saturation Density, $\rho_{v,sat}$ [kg/m^3]	0.023088
Liquid Compressibility, ψ_l [s^2/m^2]	4.46406×10^{-7}
Vapour Compressibility, ψ_v [s^2/m^2]	5.5296×10^{-6}
Turbulence Model	$k - \omega$ SST
Turbulence Intensity, I [-]	0.05
Turbulent Kinetic Energy (inlet), k [m^2/s^2]	1.47665
Turbulent Mixing Length, l [m]	0.0005
Specific Dissipation, ω [s^{-1}]	4437.1973
Flow Solver 1	BES
Flow Solver 2	TES
Courant No (Max)	0.45
Acoustic Courant No (Max)	50
Time step, Δt [s]	1×10^{-6}

Table 3-1: Hemipherical headform baseline simulation parameters

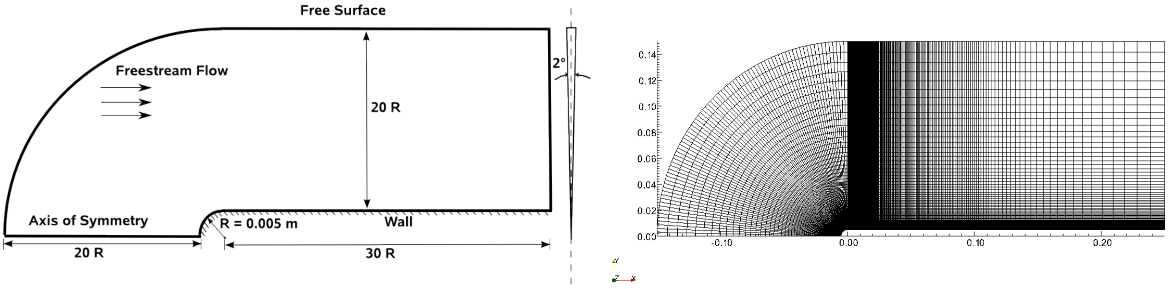

(a) Domain and Boundary Conditions **(b)** Mesh

Figure 3-2: Hemispherical headform domain, boundary conditions, and mesh intensity, barotropic compressibility model, and cavitation models are described in section B-1.

3-1-1 Grid convergence

The mesh for the baseline case should have converged results for the predicted cavitation parameters. The goal of this analysis is to check the variation of results due to mesh resolution, obtain convergence by adjusting the resolution, and use the optimal grid resolution for further analyses. For this purpose, we use four different meshes, namely, a very coarse mesh with 3297 points and a y^+ of 331.25, a coarse mesh with 12751 points and y^+ of 237, a nominal mesh with 50301 points and y^+ of 87.5, and a fine mesh with 199801 points and y^+ of 44. The X and Y axes have multiple cells and the Z-axis is one cell deep. A simple grading is applied on the mesh such that the resolution at and in the vicinity of the wall is high. The grading is also applied in such a manner that the estimated cavitating region has higher resolution than the domain downstream. The test cases are run with the same boundary conditions and flow parameters. The meshing parameters are the same for simulations using both the solvers.

Case	Points	y^+_{wall}
Very Coarse	3297	331.25
Coarse	12751	237
Nominal	50301	87.5
Fine	199801	44

Table 3-2: Test cases - grid convergence

The simulation is run from the initial time of 0 seconds to 0.1 seconds with a time step of 1×10^{-6} seconds. Field averaging is done for pressure, density, and velocity fields. Since two solvers, Barotropic Equation based Solver (BES) and Transport Equation based Solver (TES), are involved, convergence of results for two sets of simulations has to be achieved. The turbulence model in use is $k - \omega$ SST, which treats the flow under $k - \omega$ formulation near the walls and switches to $k - \epsilon$ formulation in the freestream region. Probes are placed at the hemispherical and cylinder walls to extract the mean values of pressure, density and velocity. Figure 3-3 shows the normalized pressure, density ratio, and liquid volume fraction distribution over the surface of the hemispherical headform.

For BES, in the normalized pressure distribution plot, C_p vs s/d, all four test cases yield results which are similar. The $C_{p,min}$ predicted using the very coarse, coarse, nominal, and fine meshes are -0.456454, -0.466117, -0.467342, and -0.458718 respectively. The difference in $C_{p,min}$ prediction among the test cases lie within a range of 2% compared to the nominal mesh. The density ratio distribution plot shows the extent to which the varying density of the flow is captured by the mesh. As the y^+ decreases, the drop in density is better captured due to better interpolation between very close points. The interpolation is improved in both the wall normal and the streamwise direction. Although variations are observed in the ability to capture the lowest density ratio, the analysed parameters such as cavitation length and onset distance have very minor variations ($< 2\%$) between nominal and fine meshes.

With respect to TES, the $C_{p,min}$ predicted by the very coarse, coarse, and fine meshes lie within a range of 0.87% of the nominal mesh. Similar to BES density distribution, the TES

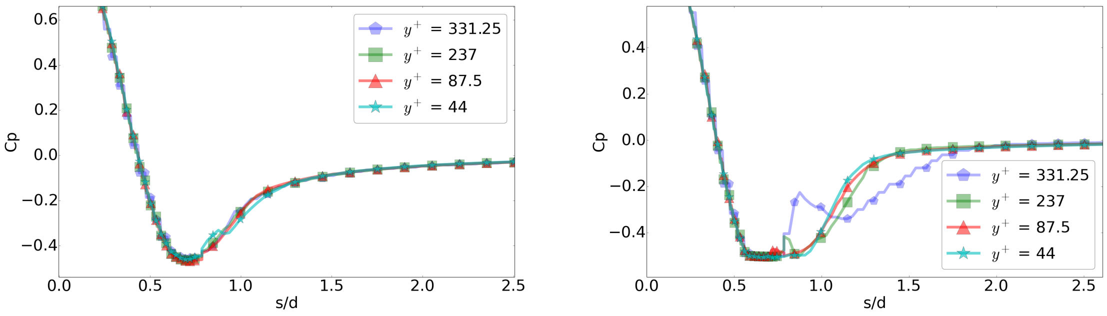

(a) Normalized pressure distribution - BES **(b)** Normalized pressure distribution - TES

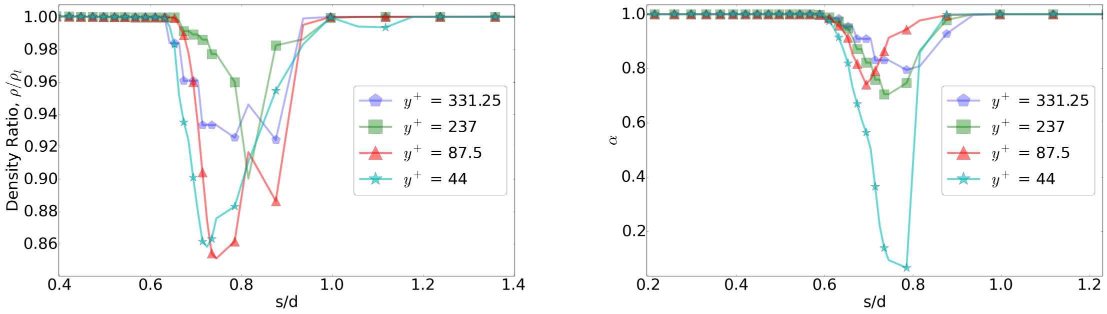

(c) Density ratio distribution - BES **(d)** liquid volume fraction distribution

Figure 3-3: Normalized pressure and density ratio distribution over the surface of the hemispherical headform are shown for the grid convergence analysis. Figure (a) The test cases yield similar results for $C_{p,min}$ which are within 2% of the nominal case. The distribution patterns are comparable for all meshes. Figure (b) The test cases yield results for $C_{p,min}$ which are within 0.87% compared to the nominal mesh (TES simulation). Figure(c) & (d) The meshes with lower y^+ values capture the drop (downward spike) in density and liquid volume fraction better because of better resolution and interpolation. Overall, for both BES and TES, good convergence for cavitation lengths, onset distances, and pressure distributions are obtained for baseline and fine meshes.

liquid volume fraction distribution is captured better as the y^+ reduces. Negligible variation is observed in pressure distribution, minimum C_p, cavitation length, and cavitation onset distance for the nominal and fine meshes in both BES and TES simulations. Thus, the convergence criteria (variation for quantified variables less than 2%) is satisfied. In order to save valuable computational time and memory, further analyses will use the nominal mesh resolution with a y^+ value of 87.5 as the baseline.

The cavitation length, onset distance, and $C_{p,min}$ are listed in table 3-3.

	BES		
Case	Cavity Length	Onset Distance	$C_{p,min}$
Very Coarse $y^+ = 331.25$	0.299399 d	0.636753 d	-0.456454
Coarse $y^+ = 237$	0.338699 d	0.657754 d	-0.466117
Baseline $y^+ = 87.5$	0.450153 d	0.636753 d	-0.468363
Fine $y^+ = 44$	0.458571 d	0.626154 d	-0.460556
	TES		
Very Coarse $y^+ = 331.25$	0.397139 d	0.599314 d	-0.502135
Coarse $y^+ = 237$	0.388869 d	0.577433 d	-0.503774
Baseline $y^+ = 87.5$	0.377880 d	0.588424 d	-0.502942
Fine $y^+ = 44$	0.377867 d	0.588424 d	-0.507321

Table 3-3: Hemispherical Headform - cavity Length, onset distance, and $C_{p,min}$ grid convergence. The length and the onset distance are represented as a measure of the diameter of the hemispherical headform.

	BES		
Case	Δ Cav. Length	Δ Cav. Onset	$\Delta C_{p,min}$
$y^+ = 331.25$	-0.150754 d (-33.49%)	-0.000000 d (-0.00%)	0.011908 d (-2.54%)
$y^+ = 237$	-0.111454 d (-24.76%)	0.021001 d (3.30%)	0.002246 d (-0.48%)
$y^+ = 44$	0.008418 d (1.87%)	-0.010599 d (-1.66%)	0.007806 d (-1.67%)
	TES		
$y^+ = 331.25$	0.019260 d (5.10%)	0.010890 d (1.85%)	0.000806 d (-0.16%)
$y^+ = 237$	0.010989 d (2.08%)	-0.010990 d (-1.87%)	-0.000832 d (0.17%)
$y^+ = 44$	-0.000013 d (-0.003%)	-0.000000 d (-0.00%)	-0.004380 d (0.87%)

Table 3-4: Hemispherical Headform - Grid convergence of cavity Length, onset distance, and $C_{p,min}$. The values for very coarse, coarse, and fine meshes are compared with the values obtained for the nominal mesh. The length and the onset distance are represented as a measure of the diameter of the hemispherical headform.

3-1-2 Baseline cases and validation

Two baseline cases are setup for each flow solver, BES and TES, with the nominal structured mesh having a $y^+ = 87.5$ and 45441 points in total. The parameters used for both the baseline cases are listed in table 3-1. Although the flow solvers differ in their implementation, they are both homogeneous flow models with a two-phase mixture of liquid and vapour. These models also assume that there is no slip between the two-phases [22].

The Barotropic Equation based Solver (BES) is a fully compressible cavitating flow solver which uses a barotropic equation of state (EOS) for density modelling. The primary assumption with this model is that the density varies only with the pressure and is independent of other parameters. The barotropic compressibility models included are linear, Wallis, and Chung models.

The Transport Equation based Solver (TES) is a applicable for two incompressible, isothermal immiscible fluids with phase change that incorporates the Volume of Fluid (VoF) phase fraction based interface capturing methods. It uses a liquid volume fraction α transport equation to model the mixture density; which includes cavitation source terms. This model allows for the modelling of the impact of inertial forces on cavities such as elongation, detachment, and drift of bubbles [33]. This model incorporates the cavitation models such as Kunz [41], Merkle [39], and SchnerrSauer [36] models in order to simulate the phase change for cavitation.

BES and TES require barotropic compressibility and cavitation models respectively (for explanation, see section B-1-2). Linear Barotropic Compressibility Model is used in BES baseline and Kunz Cavitation Model is used in TES Baseline.

Regarding the BES baseline case, figures 3-4a and 3-4b represent the mean pressure and mean density contours respectively. Figure 3-4c represents the non-dimensionalised pressure distribution (coefficient of pressure) vs the surface distance normalized by the diameter (s/d). Cavitation is said to occur, in simple terms, when $-C_{p,min} = \sigma$. It is observed that the difference between the $C_{p,min}$ value of the BES baseline case and the literature ($C_{p,min} = -\sigma =$ -0.5) is 0.0358. Figure 3-4d represents the density ratio vs s/d. The cavity length is calculated by taking the surface distance over which the density ratio ρ/ρ_l falls below 1 (pure liquid phase). The value of cavity length is calculated to be 0.450 diameters of the hemispherical head.

Regarding the TES baseline case, figures 3-5a and 3-5b represent mean relative pressure and mean liquid volume fraction contours. The probe points are placed along the surface and the mean relative pressure ($p_{rgh,mean}$) and mean liquid volume fraction (α_{mean}) are extracted along the probe points. The non-dimensionalized pressure distribution over the surface is given by the normalized pressure distribution plot. Since the mean pressure calculated during the simulation is relative rather than absolute, it is converted into absolute pressure by adding the product $\rho \cdot g \cdot h$ to it, i.e., $p = p_{rgh} + \rho \cdot g \cdot h$; here, g is the acceleration due to gravity and h is the height. The α_{mean} vs s/d plot gives us an estimate of the cavity length. The cavity length is calculated by measuring the surface distance over which the the α value drops below 1 (pure liquid phase). The cavity length is calculated to be 0.37788 d. The difference in the prediction of $C_{p,min}$ between the literature and TES is 0.001. The physical time taken for the simulation is 5 times shorter than that of BES case.

The BES result varies by -6.33% and the TES result varies by +0.588% from the ideal value of -0.5 (-σ). Both the BES and TES pressure distributions show good agreement with the profile obtained from Rouse & McNown (1948) [58]. The TES result fits the best with respect to the literature. The cavitation length and onset distance calculated by the two flow solvers are listed in table 3-5. Figure 3-6 shows the comparison between the results obtained using the two solvers.

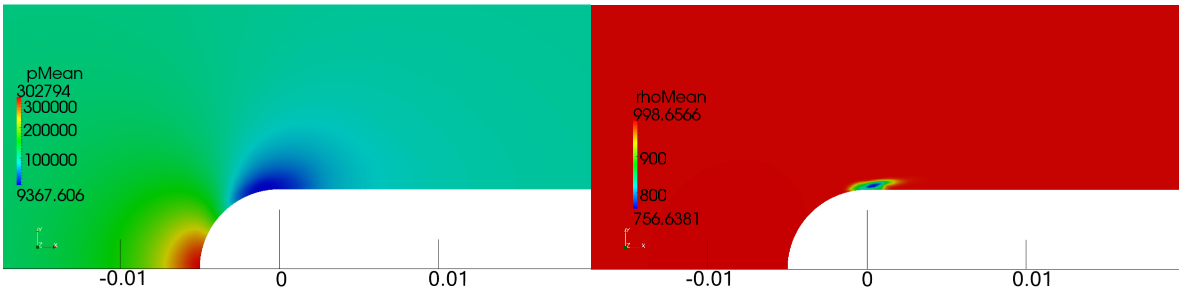

(a) Mean Pressure distribution (Pa) (distance in m)

(b) Mean Density distribution (kg/m^3)

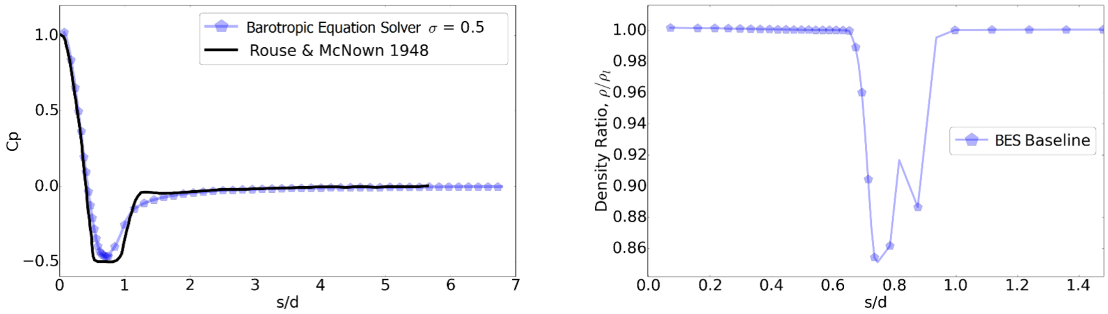

(c) Normalized pressure distribution

(d) Density ratio distribution over the surface

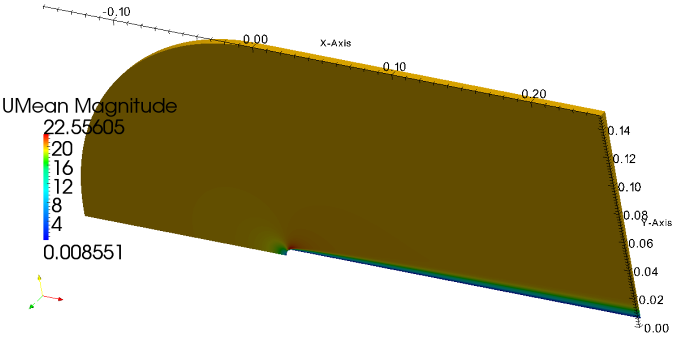

(e) Mean Velocity distribution

Figure 3-4: Mean pressure, density, and velocity distributions for the flow over a hemispherical headform are shown. Figures (a) and (b) show the distribution of mean pressure and mean density respectively over the surface of the headform for the modelled BES baseline case. The stagnation region and the cavitating region are clearly observed. The pressure is indicated in Pascals and the density in kg/m^3. Figure (c) shows the coefficient of pressure (C_p) vs the surface distance normalized by the diameter (s/d) for the modelled BES baseline configuration and the literature [58]. The quantity C_p is $(p - p_o)/(0.5\,\rho U^2)$. Figure (d) shows the density distribution over the surface. The cavity length associated is calculated using ρ/ρ_l vs s/d plot and has a value of 0.450 diameters (of the hemispherical headform). Figure (e) represents the mean velocity distribution. The high velocity region just above the hemispherical head is observed.

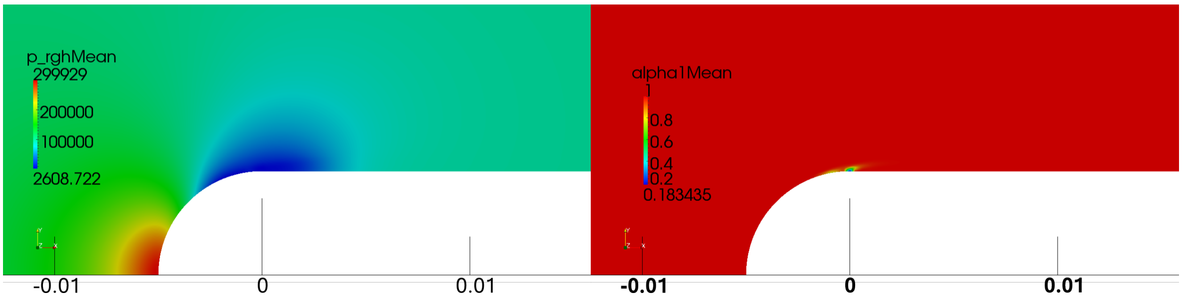

(a) Mean relative pressure distribution (Pa) (distance in m)

(b) Mean liquid volume fraction distribution

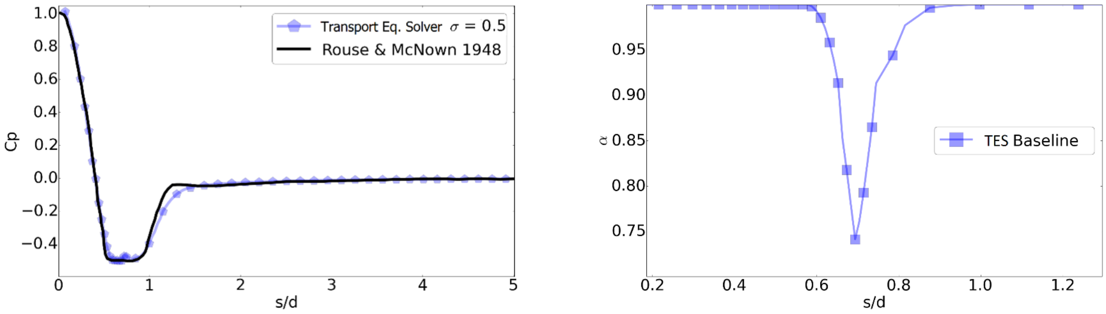

(c) Normalized pressure distribution

(d) liquid volume fraction distribution over the surface

Figure 3-5: Mean relative pressure and liquid volume fraction distributions are shown. Figures (a) and (b) show the distribution of mean relative pressure and liquid volume fraction respectively over the surface of the headform for the modelled TES baseline case. Figure (c) shows the coefficient of pressure (C_p) vs the surface distance normalized by the diameter (s/d) for the modelled TES baseline configuration and the literature [58]. The pressure used for the calculation of C_p is the absolute mean pressure obtained using $p = p_{rgh} + \rho gh$; where p_{rgf} is the mean relative pressure, g is the gravitational acceleration, and h is the height. Figure (d) shows the liquid volume fraction distribution vs s/d. The calculated cavity length (surface distance where $\alpha < 1$) has a value of 0.37788 diameters (of the hemispherical headform).

Solver	Cav. Length	Cav. Onset Distance	$C_{p,min}$
BES Baseline	0.450153 d	0.636753 d	-0.468363
TES Baseline	0.377880 d	0.588424 d	-0.502942

Table 3-5: Hemispherical Headform - Cavitation Solver Comparison

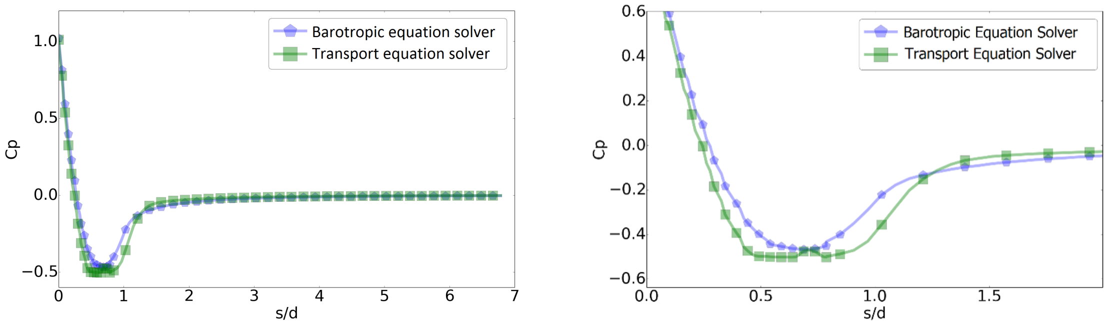

(a) BES vs TES normalized pressure distribution

(b) Close up: BES vs TES normalized pressure distribution

Figure 3-6: Comparison of normalized mean pressure distribution over the surface of the hemispherical headform are shown for BES and TES solvers. BES predicts a lower $|C_{p,min}|$ than that of TES. The $C_{p,min}$ of BES is -0.468363 and that of TES is -0.502942

3-1-3 Turbulence model influence

Addressing the uncertainty with regards to the choice of turbulence model on its influence on cavitation parameters is the primary focus of our analysis. The baseline parameters listed in table 3-1 except the turbulence models are kept unchanged. The BES and TES simulations are carried out separately and the change in cavitation parameters predictions from their respective baseline cases are quantified and compared. The $k-\omega$ SST turbulence model is used in the baseline case and the varied turbulence models are $k-\omega$, $k-\varepsilon$, RNG $k-\varepsilon$, and Launder-Reece-Rodi Reynolds Stress Model. The turbulence models and the corresponding parameters that are implemented and tested are listed in table 3-6. The governing equations of the turbulence models are listed in section 2-3.

Turbulence Model	k	ω	R	ϵ
$k-\omega$ SST (Base)	1.47665	4437.1973	-	-
$k-\epsilon$	1.47665	-	-	589.69
$k-\omega$	1.47665	4437.1973	-	-
Reynolds Stress Model	1.47665	-	(1.47665 0 0 0.738325 0 0.738325)	589.69
RNG $k-\epsilon$	1.47665	-	-	589.69
Laminar	-	-	-	-

Table 3-6: Hemispherical Headform - turbulence model influence test cases

Figures 3-7a and 3-7b represent the normalized pressure distributions for BES and TES simulations respectively. Figures 3-7c and 3-7d represent the density ratio and liquid volume fraction distributions respectively.

In BES simulations, the $k-\omega$ model and laminar pressure distributions follow a similar pattern with marginal variations with respect to the baseline. The RSM pressure distribution is similar but a minor difference exists. The $k-\epsilon$ model differs significantly and a discontinuous cavitation bubble is observed. The $k-\omega$, laminar, and the $k-\omega$ SST baseline cases have similar density ratio distribution pattern. The RSM model predicts the onset and the end of

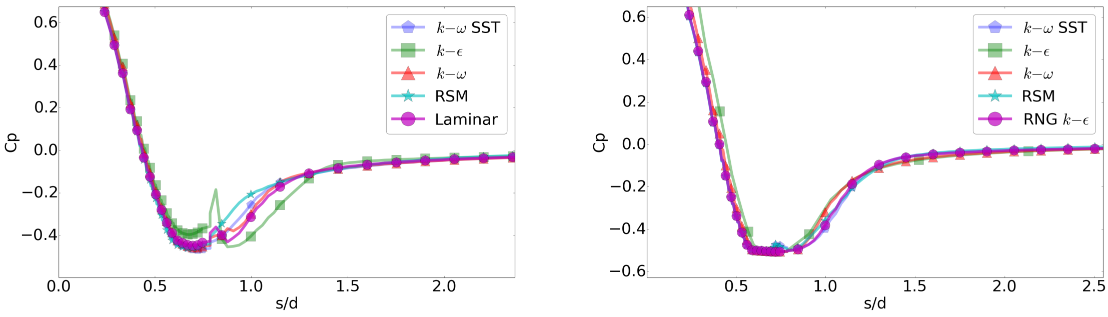

(a) Normalized pressure distribution - BES

(b) Normalized pressure distribution- TES

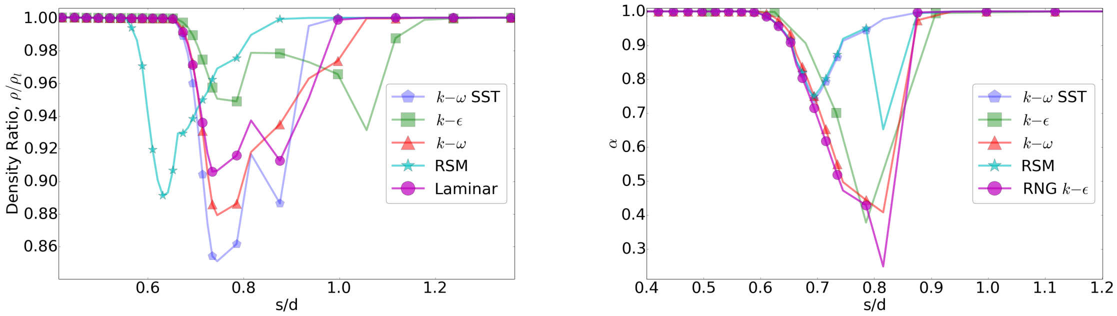

(c) Density ratio distribution - BES

(d) liquid volume fraction distribution - TES

Figure 3-7: Normalized Pressure, Density ratio, and liquid volume fraction distribution over the surface of the hemispherical headform are shown for the turbulence model influence analysis. Figure (a)The $k - \epsilon$ model in BES simulation results in a discontinuous cavitation bubble off the surface. The rest of the models follow a similar pattern. Figure (b) The TES simulations result in similar distribution patterns with marginal variation. Figure (c) A significant variation in the density distribution patterns are observed for all the turbulence models. Figure (d) The turbulence models show similar liquid volume fraction distribution patterns.

cavitation earlier than rest of the models and cavitation length predicted is also ~27% lower. The $k - \epsilon$ model predicts a late onset (discontinuity) and an elongated cavitation length.

In TES simulations, all turbulence models have very similar pressure distributions. The deviation in results, from the baseline case, is within 0.62%. A similarity in liquid volume fraction distributions is also observed for all turbulence models. The $k - \epsilon$ and $k - \omega$ models predict larger cavity lengths whereas the RSM and RNG $k - \epsilon$ models predict the exact value with respect to the baseline.

The turbulence model influence is significant in the case of BES simulations. However, it is low in the case of TES simulations.

Case	Cav. Length	Cav. Onset	$C_{p,min}$
	BES		
$k - \omega$ SST	0.450153 d	0.636753 d	-0.468363
$k - \epsilon$	0.579905 d	0.657754 d	-0.454417
$k - \omega$	0.459302 d	0.657754 d	-0.457510
RSM	0.326383 d	0.549467 d	-0.461148
Laminar	0.450153 d	0.636753 d	-0.447891
	TES		
$k - \omega$ SST	0.377880 d	0.588424 d	-0.502942
$k - \epsilon$	0.405554 d	0.624744 d	-0.505660
$k - \omega$	0.427290 d	0.599314 d	-0.504912
RSM	0.377880 d	0.588424 d	-0.502886
RNG $k - \epsilon$	0.377880 d	0.588424 d	-0.506073

Table 3-7: Hemispherical Headform - turbulence model influence Cases

Case	Δ Cav. Length	Δ Cav. Onset	$\Delta C_{p,min}$
		BES	
$k - \epsilon$	0.129752 d (28.82%)	0.021001 d (3.30%)	0.013946 d (-2.98%)
$k - \omega$	0.009149 d (2.03%)	0.021001 d (3.30%)	0.010853 d (-2.32%)
RSM	-0.123770 d (-27.50%)	-0.087286 d (-13.71%)	0.007215 d (-1.54%)
Laminar	-0.000000 d (-0.00%)	-0.000000 d (-0.00%)	0.020472 d (-4.37%)
		TES	
$k - \epsilon$	0.027674 d (7.32%)	0.036321 d (6.17%)	-0.002718 d (0.54%)
$k - \omega$	0.049411 d (13.08%)	0.010890 d (1.85%)	-0.001970 d (0.39%)
RSM	-0.000000 d (-0.00%)	-0.000000 d (-0.00%)	0.000055 d (-0.01%)
RNG $k - \epsilon$	-0.000000 d (-0.00%)	-0.000000 d (-0.00%)	-0.003131 d (0.62%)

Table 3-8: Hemispherical Headform - turbulence model influence Cases

3-2 Hydrofoil : Attached leading edge cavitation

The attached leading edge cavitation on the inducer blade surface is simplified and represented using a flow past a symmetrical hydrofoil. Experimental investigation of a cryogenic flow past a symmetrical hydrofoil was carried out by Hord (1973) [59]. The dimensions of the hydrofoil used in the experiments are given in figure 3-8. Owing to the shape of the hydrofoil, a negative pressure gradient exists downstream of the flow. The cryogenic liquid that is used for the flow simulation is LH2 at 18 K. The numerical setup is exactly based on the hydrofoil geometry used by Hord [59]. The reference simulation parameters are listed in the table 3-9.

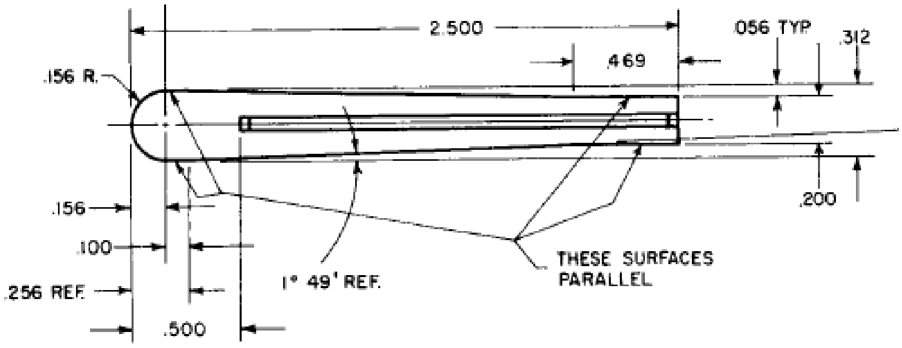

(a) Dimensions in inches (From Hord (1973) [59])

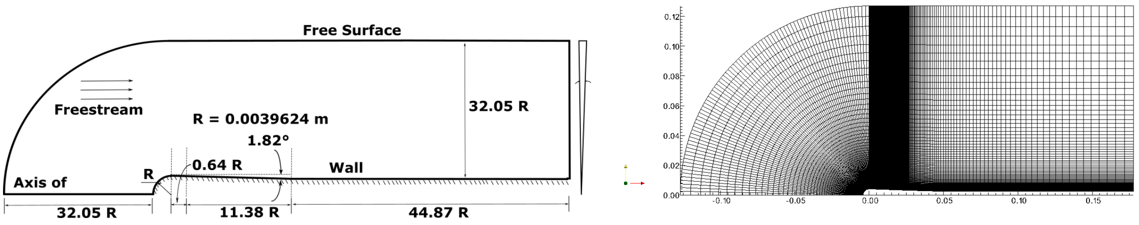

(b) Domain and Boundaries

(c) Mesh

Figure 3-8: Hydrofoil dimensions, domain, boundary conditions, and mesh. In figure (a) the dimensions are in inches and in figure (b) the dimensions are in metres with equivalent converted values.

The ambient pressure is set at 84239 Pa, the inlet velocity at 53.9305 m/s, the density at 73.437 kg/m^3, and the subsequent Reynolds number at 1.921×10^6. The corresponding fluid properties are obtained from [61].

In the following sections, grid convergence of results are obtained and an optimal mesh resolution is selected. This optimal mesh when used shall yield converged results while requiring acceptable computational time (less than 15 hours physical time). Then, baseline cases are setup for BES and TES simulations using the optimal resolution and the influence of flow solver on cavitation parameters is analysed. Finally, the influences of operating fluid and turbulence model are quantified and analysed.

The turbulence intensity, barotropic compressbility model, and Reynolds number sensitivity analyses are not pursued. It is presumed that the turbulence intensity and barotropic compressibility model will not have a major effect. The reason behind this assumption comes

Parameter	Value
Fluid	liquid Hydrogen (LH2)
Radius, R [m]	3.9624×10^{-3}
Ambient Pressure, P_∞ [Pa]	84239
Ambient Temperature, T_∞ [K]	18
Cavitation No. σ [-]	≈ 0.35
Freestream Velocity, U_∞ [m/s]	53.9305
Freestream Density, ρ_∞ [kg/m^3]	73.437
Reynolds No, Re [-]	1.921×10^6
Liquid Dyn. Viscosity, μ_l [Pa-s]	1.634×10^{-5}
Vapour Dyn. Viscosity, μ_v [Pa-s]	9.3507×10^{-7}
Saturation Pressure, P_{sat} [Pa]	46602
liquid Saturation Density, $\rho_{l,sat}$ [kg/m^3]	73.377 at T_∞ and P_∞
Vapour Saturation Density, $\rho_{v,sat}$ [kg/m^3]	0.6653
Liquid Compressibility, ψ_l [s^2/m^2]	7.1794×10^{-7}
Vapour Compressibility, ψ_v [s^2/m^2]	8.58575×10^{-6}
Turbulence Model	$k - \omega$ SST
Turbulence Intensity, I [-]	0.05
Turbulent Kinetic Energy, k [m^2/s^2]	10.90608
Turbulent Mixing Length, l [m]	0.0005
Specific Dissipation, ω [s^{-1}]	12059.226
Flow Solver 1	BES
Flow Solver 2	TES
Courant No (Max)	0.45
Acoustic Courant No (Max)	50
Time step, Δt [s]	1×10^{-6}

Table 3-9: Hydrofoil - reference parameters

from similar analyses of an external flow over a hemispherical headform. Also, the Reynolds numbers, as long as they are above the critical value and in the same order of magnitude, are presumed to have little effect on the cavitation size, onset, and pressure distribution.

3-2-1 Grid convergence

To select the optimal mesh, four simulations with different resolutions ranging from very coarse to fine are carried out and convergence of predicted cavitation parameters are checked for. These tests are carried out only for the TES because the corresponding simulations are fast. The corresponding y^+ and number of meshing points are listed in table 3-10.

Case	Points	y^+_{wall}	u^+_{wall}
Very Coarse	3633	2625	24.302
Coarse	13981	1360	22.700
Baseline	55161	692	21.050
Fine	219121	348.7	19.378

Table 3-10: Hydrofoil - test cases for grid convergence analysis - TES

The very coarse, coarse, and the fine meshes result in a similar pressure distribution pattern compared to the nominal mesh ($y^+ = 692$). The difference in $C_{p,min}$ values predicted by very coarse and coarse meshes are negligible and lie within a range of 0.81%. However, the fine mesh yielded a difference upto 7.72%. When investigated closely, it was found that there was a numerical anomaly, for which the exact reason is unknown, at one location and it resulted in such a value. Discarding the anomaly, the difference between the $C_{p,min}$ values of the fine and nominal meshes is 1.43%. The cavitation length predicted by the very coarse mesh lies within a moderately close range to that of the nominal mesh (7%). The difference in cavitation lengths between fine and nominal meshes are negligible.

The onset distance predicted by coarse and fine meshes range within 4.33% of the corresponding nominal mesh value. Eventhough the difference between the nominal and the fine meshes are such, it is considered to be a minor variation. The liquid volume fraction distribution patterns are similar between the baseline and the coarse grid. The fine mesh α distribution has a minor variation from that of the nominal mesh distribution but the global parameters such as length and onset distances satisfy the convergence criteria. Overall, a good convergence of cavitation lengths, onset distances, and pressure distributions is achieved between the nominal and the fine meshes. Thus, the nominal resolution is used for further analyses.

Case	Cav. Length	Cav. Onset	$C_{p,min}$
$y^+ = 2625$	1.073334 d	0.572090 d	-0.359124
$y^+ = 1360$	1.102848 d	0.590872 d	-0.359480
$y^+ = 692$	1.154157 d	0.566336 d	-0.356605
$y^+ = 348.7$	1.164261 d	0.590872 d	-0.361704

Table 3-11: Hydrofoil - cavitation length, onset distance, and $C_{p,min}$ - grid convergence

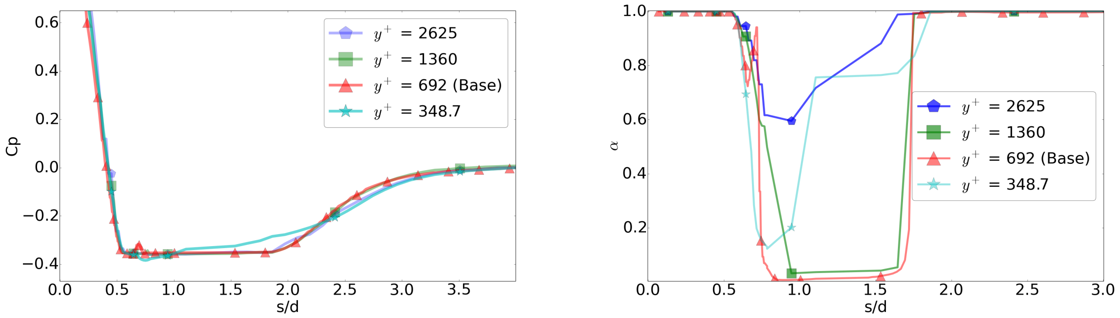

(a) Normalized pressure distribution **(b)** liquid volume fraction distribution

Figure 3-9: Normalized pressure and liquid volume fraction distributions over the surface of the hydrofoil are shown for TES grid convergence analysis. The pressure distribution patterns are observed to be similar with marginal variation.

Case	Δ Cav. Length	Δ Cav. Onset	$\Delta C_{p,min}$
$y^+ = 2625$	-0.080823 d (-7.00%)	0.005754 d (1.02%)	-0.002520 (0.71%)
$y^+ = 1360$	-0.051308 d (-4.44%)	0.024536 d (4.33%)	-0.002875 (0.81%)
$y^+ = 348.7$	0.010104 d (0.88%)	0.024536 d (4.33%)	-0.005099 (1.43%)

Table 3-12: Hydrofoil grid convergence check

3-2-2 Baseline cases and flow solver influence

Baseline cases are setup for both BES and TES with the nominal mesh resolution. The turbulence model in the baseline cases is $k-\omega$ SST. Linear barotropic compressibility model and Kunz cavitation model are used for BES and TES baseline cases respectively. The reference parameters are listed in table 3-9. Figures 3-10 and 3-11 show the pressure, density, and velocity distributions for BES and TES respectively.

The BES and TES simulations have a stark difference in the normalized pressure distribution curves. Significant difference in the cavitation length predictions are also observed between the two cases. The cavitation length predicted by BES is $\sim$0.9 diameters (hydrofoil head) higher than that of TES. The TES simulation results in an earlier onset than the BES simulation. However, the difference $C_{p,min}$ prediction is marginal. The computational time required for the TES simulation is 4 times lesser than that of BES simulation. The pressure distribution, density distribution, and liquid volume fraction distribution along the surface of the hydrofoil for BES and TES simulations are shown in figures 3-10 and 3-11. The differences are quantified in table 3-13.

Case	Cav. Length	Cav. Onset	$C_{p,min}$
BES Baseline	2.053299 d	0.577433 d	-0.355398
TES Baseline	1.154157 d	0.566336 d	-0.356605

Table 3-13: Hydrofoil - Baseline cases and flow solver influence

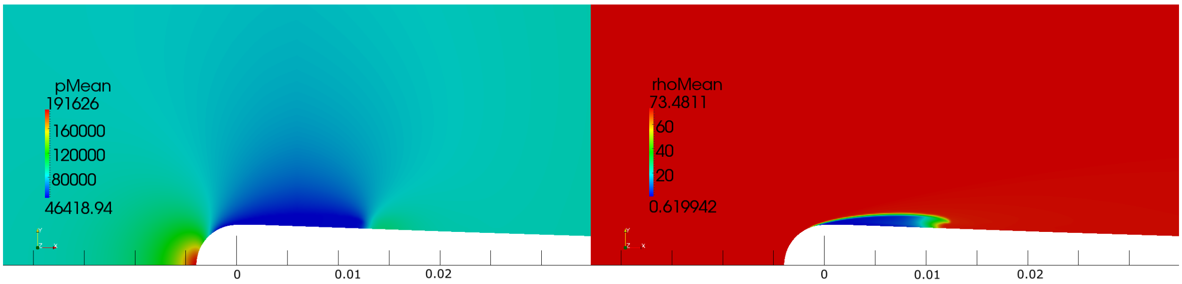

(a) Mean Pressure distribution (Pa) (distance in m) **(b)** Mean Density distribution (kg/m^3)

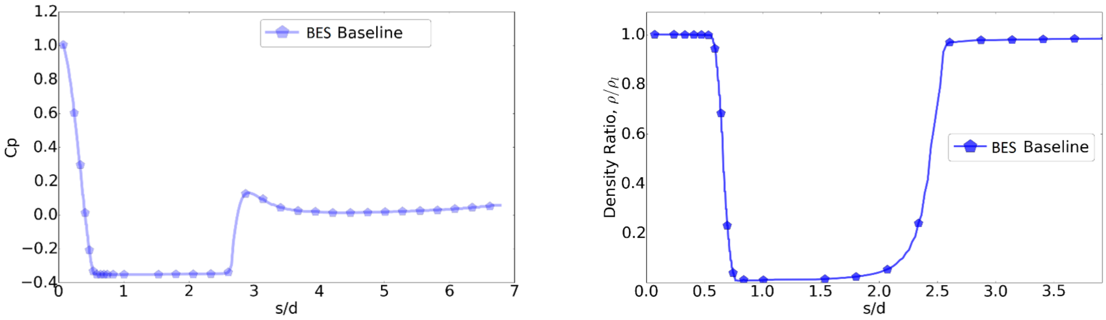

(c) Normalized pressure distribution **(d)** Density distribution over the surface

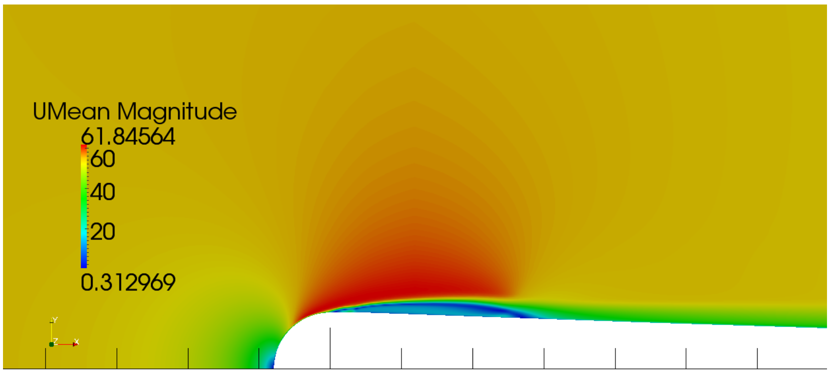

(e) Mean Velocity distribution

Figure 3-10: Mean pressure, density, and velocity distributions for cyrogenic flow over a hydrofoil are shown in this figure. Figures (a) and (b) show the distribution of mean pressure and density respectively over the surface of the hydrofoil for the modelled BES baseline case. Figure (c) shows the coefficient of pressure (C_p) vs the surface distance normalized by the diameter (s/d) for the modelled baseline configuration. The quantity C_p is $(p - p_o)/(0.5\,\rho\,U^2)$. Figure (d) shows the density distribution vs s/d. The cavity length is calculated to be 2.0533 diameters (of the hydrofoil head). Figure (e) represents the mean velocity distribution.

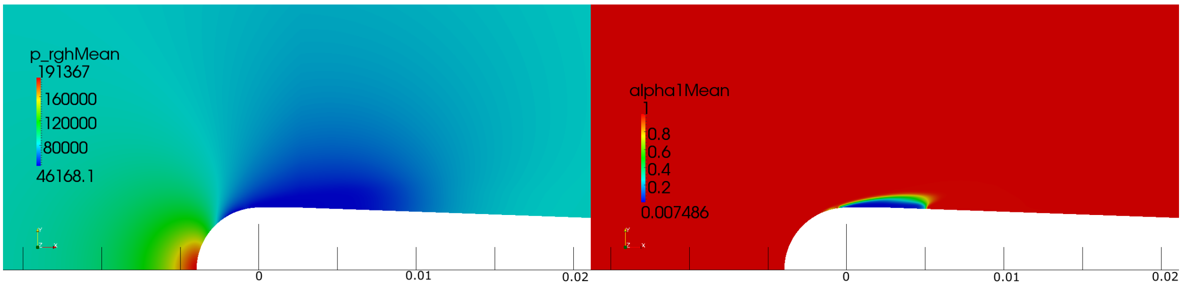

(a) Mean relative pressure distribution (Pa) (distance in m)

(b) Mean liquid volume fraction distribution

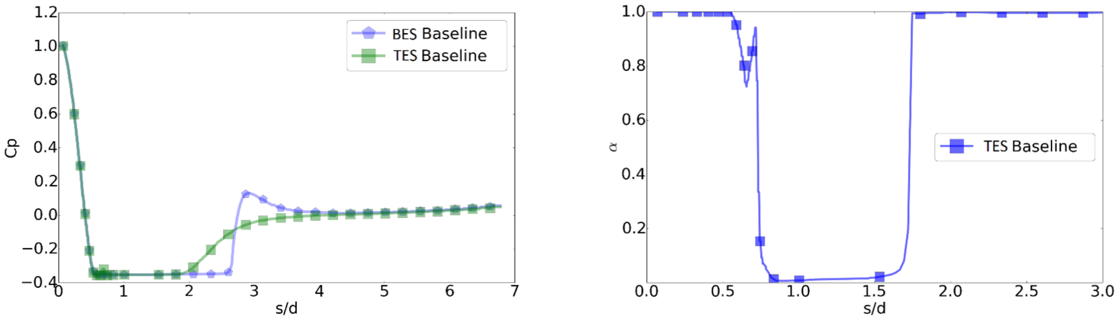

(c) Normalized pressure distribution

(d) Liquid volume fraction distribution over the surface

Figure 3-11: Mean relative pressure and liquid volume fraction distribution for a cyrogenic flow over a hydrofoil are shown. Figures (a) and (b) show the distribution of mean relative pressure and liquid volume fraction respectively over the surface of the hydrofoil for the modelled TES baseline case. Figure (c) compares the coefficient of pressure (C_p) vs the surface distance normalized by the diameter (s/d) for the modelled TES and BES baseline configurations. Figure (d) shows the liquid volume fraction distribution over the surface. The cavity length associated is calculated using the plot and has a value of 1.154157 diameters (of the hydrofoil head).

3-2-3 Operating fluid influence

In this section, we analyse the sensitivity of cavitation parameters in the cryogenic flow over the hydrofoil by changing the operating fluid. The fluids to be used are liquid Nitrogen (LN2), liquid Oxygen (LO2), and liquid Hydrogen (LH2 - Baseline). The properties settings for the two fluids, LN2 and LO2, are listed in table 3-14. The properties of LH2 are listed in table 3-9.

Parameter	Value	Value
Fluid	liquid Nitrogen (LN2)	liquid Oxygen (LO2)
Ambient Pressure, P_∞ [Pa]	81051.11	78325.52
Ambient Temperature, T_∞ [K]	70	80
Cavitation No. σ [-]	0.35	0.35
Freestream Velocity, U_∞ [m/s]	17.1206	15.31167
Freestream Density, ρ_∞ [kg/m^3]	838.64	1192.5
Reynolds No, Re [-]	5.174×10^5	5.387×10^5
Liquid Dyn. Viscosity, μ_l [Pa-s]	2.199×10^{-4}	2.6859×10^{-4}
Vapour Dyn. Viscosity, μ_v [Pa-s]	4.879×10^{-6}	6.1260×10^{-6}
Saturation Pressure, P_{sat} [Pa]	38545	30123
Liquid Saturation Density, $\rho_{l,sat}$ [kg/m^3]	838.51	1192.2
Vapour Saturation Density, $\rho_{v,sat}$ [kg/m^3]	1.8960	1.4684
Liquid Compressibility, ψ_l [s^2/m^2]	1.6687×10^{-6}	1.0256×10^{-6}
Vapour Compressibility, ψ_v [s^2/m^2]	3.5254×10^{-5}	3.5279×10^{-5}
Turbulence Intensity, I [-]	0.05	0.05
Turbulent Kinetic Energy, k [m^2/s^2]	1.09918	0.87917
Turbulent Mixing Length, l [m]	0.0005	0.0005
Specific Dissipation, ω [s^{-1}]	3828.2825	3423.7935

Table 3-14: Hydrofoil LN2 and LO2 Parameters

The pressure distribution patterns found in BES are similar with very small differences. Such type of similarity among the pressure distribution curves are also found in TES simulations. The $C_{p,min}$ values predicted by both BES and TES simulations for LN2 and LO2 fluids have minor differences with that of LH2 (baseline) predictions. The density ratio distributions follow similar patterns for all fluids. The cavitation length variations for LN2 and LO2 using BES simulations are small when compared to the LH2 values. They lie within 6.52%. The onset distance variations are negligible. With TES simulations, the cavitation lengh and onset distance variations are negligible. The liquid volume fraction distributions vary moderately although the length and onset predictions are identical to the baseline case. A small non-cavitating pocket of liquid is found in the cavitation zone for liquid Nitrogen TES Simulation.

The sensitivity of cavitation parameters due to the changes in fluids is not significant in this flow domain. However, one should exercise caution while setting the paramters for the fluids. The settings for LN2 and LO2 simulations which are similar to the baseline case are cavitation number and mesh resolution only. The fluid properties are obtained at standard temperatures and the simulation parameters are adjusted correspondingly to maintain the cavitation number (non-dimensional parameter) constant for all fluids. Since the domain is non-bounded, there aren't significant differences when the fluids are changed. Significant differences may occur for bounded flow problems due to the constraint on mass flow rate conservation (see section 3-3-3.

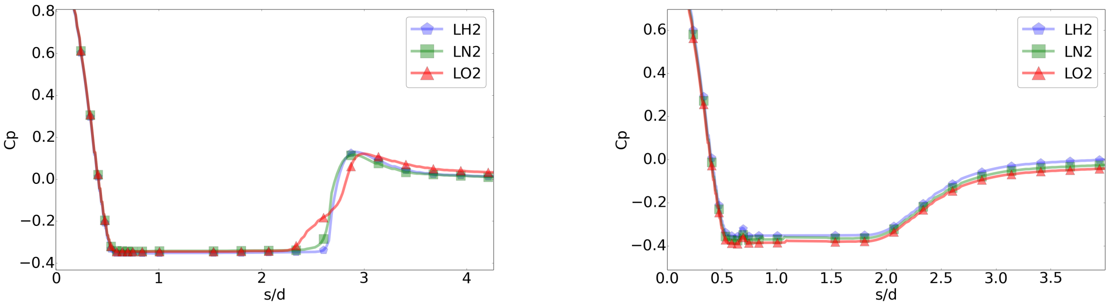

(a) Normalized pressure distribution - BES **(b)** Normalized pressure distribution - TES

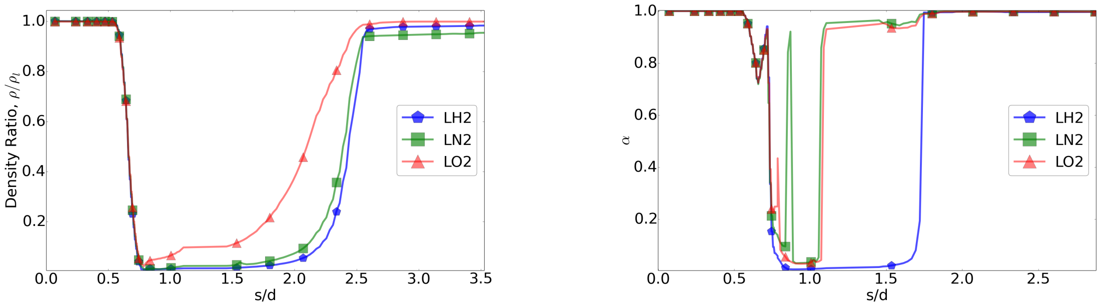

(c) Density ratio distribution **(d)** liquid volume fraction distribution

Figure 3-12: Normalized pressure, density ratio, and liquid volume fraction distributions over the surface of the hydrofoil are shown for for multiple fluids. The pressure distribution patterns are similar in BES simulations and also in TES simulations. The density distribution in BES simulations also follow a simular pattern. A moderate variation is found in the case of liquid volume fraction distributions for multiple fluids in TES simulations.

Case	Cav. Length	Cav. Onset	$C_{p,min}$
		BES	
LH2	2.053299 d	0.577433 d	-0.355398
LN2	1.919440 d	0.577433 d	-0.343571
LO2	1.919440 d	0.577433 d	-0.344964
		TES	
LH2	1.154157 d	0.566336 d	-0.356605
LN2	1.154157 d	0.566336 d	-0.374792
LO2	1.154157 d	0.566336 d	-0.389904

Table 3-15: Hydrofoil - cavitation length, onset distance, and $C_{p,min}$ for multiple fluids.

Case	Δ Cav. Length	Δ Cav. Onset	$\Delta C_{p,min}$
		BES	
LN2	-0.133859 d (-6.52%)	-0.000000 d (-0.00%)	0.011827 d (-3.33%)
LO2	-0.133859 d (-6.52%)	-0.000000 d (-0.00%)	0.010434 d (-2.94%)
		TES	
LN2	-0.000000 d (-0.00%)	-0.000000 d (-0.00%)	-0.018187 d (5.10%)
LO2	-0.000000 d (-0.00%)	-0.000000 d (-0.00%)	-0.033299 d (9.34%)

Table 3-16: Hydrofoil - change in cavitation length, onset distance, and $C_{p,min}$ for multiple fluids.

3-2-4 Turbulence model influence

The turbulence models influence analysis is pursued by using multiple turbulence models such as $k-\omega$ SST, $k-\epsilon$, $k-\omega$, RSM, and RNG-$k-\epsilon$. A laminar simulation is also pursued to test the importance of turbulence modelling. The parameter settings for the various turbulence models and the laminar case are listed in table 3-17.

Turbulence Model	k	ω	R	ϵ
$k-\omega$ SST (Base)	10.906	12059.2264	-	-
$k-\epsilon$	10.906	-	-	11836.271
$k-\omega$	10.906	12059.2264	-	-
Reynolds Stress Model (LRR)	10.906	-	(10.906 0 0 5.453 0 5.453)	11836.271
RNG $k-\epsilon$	10.906	-	-	11836.271
Laminar	-	-	-	-

Table 3-17: Hydrofoil - turbulence model influence Cases

In BES Simulations, the pressure distributions for various turbulence models vary by a large margin (Figure 3-13). A strong variation in pressure distribution is observed in the case of $k-\omega$ simulation, particularly in the divergent part of the hydrofoil. There is a negative pressure gradient downstream of the flow and it is conjectured that $k-\omega$ model predicts an early pressure recovery due to its sensitivity to adverse pressure gradients (positive or negative) in the flow. A similar pressure distribution pattern to that of $k-\omega$ is also observed in the laminar simulation. The laminar formulation uses a dummy turbulence model and supplies a value of 0 to the turbulent viscosity, thermal diffusivity, kinetic energy, Reynolds stress tensor etc. Laminarisation of the turbulent flow field leads to a higher sensitivity towards adverse pressure gradients. The RSM, $k-\epsilon$, and the baseline cases have nearly identical pressure distribution curves. The $k-\omega$ and laminar simulation also tend to have a similar density distribution. Again, the RSM and $k-\epsilon$ show similarity with that of the $k-\omega$ SST baseline case. The cavitation lengths and their variations are listed in tables 3-18 and 3-19. The variations in density distributions can be observed from the contour plots in figure 3-14.

In TES Simulations, the pressure distribution patterns for all turbulence models are near identical and the differences are negligible with respect to $k-\omega$ SST. In the liquid volume fraction plots, the $k-\omega$ and $k-\epsilon$ models follow similar patterns with that of the $k-\omega$ SST. The RSM and RNG $k-\epsilon$ models have a minor variation in α distribution. The cavitation layer detachment is observed in these two turbulence models (figure 3-14)

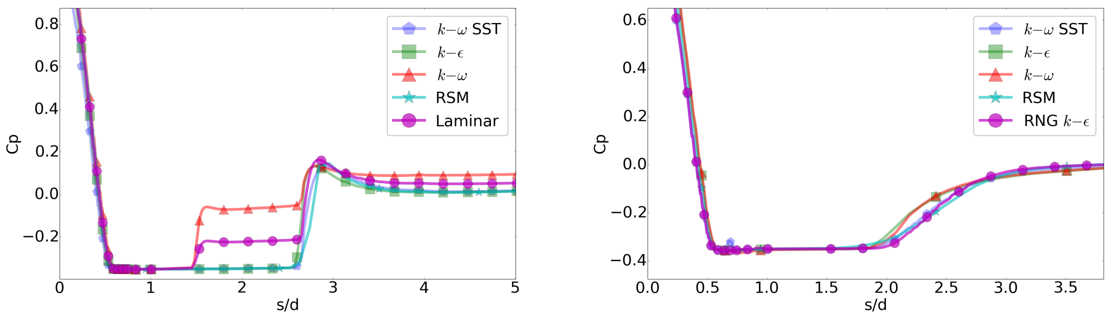

(a) Normalized pressure distribution - BES **(b)** Normalized pressure distribution - TES

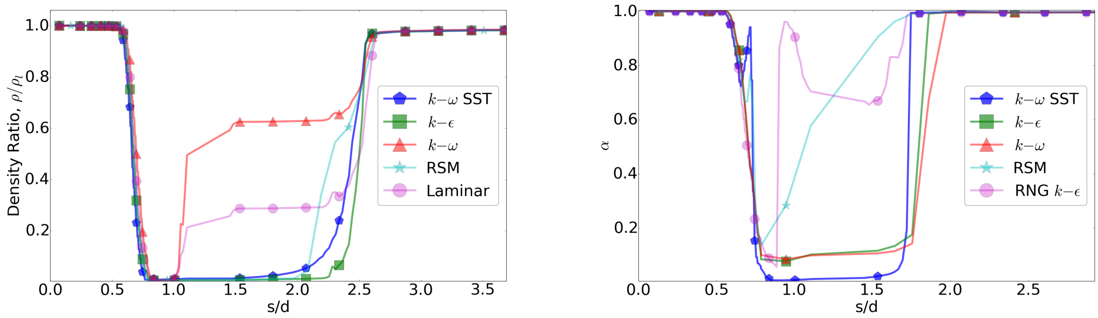

(c) Density ratio distribution **(d)** Liquid volume fraction distribution

Figure 3-13: Normalized pressure, density ratio, and liquid volume fraction distributions over the surface of the hydrofoil are shown for TES turbulence model influence analysis.

Case	Cav. Length	Cav. Onset	$C_{p,min}$
	BES		
$k-\omega$ SST	2.053299 d	0.577433 d	-0.355398
$k-\epsilon$	1.988766 d	0.588423 d	-0.354255
$k-\omega$	1.999237 d	0.604724 d	-0.354466
RSM	1.898117 d	0.623725 d	-0.354198
Laminar	2.031419 d	0.599314 d	-0.353751
	TES		
$k-\omega$ SST	1.154157 d	0.566336 d	-0.356605
$k-\epsilon$	1.164261 d	0.590872 d	-0.359614
$k-\omega$	1.271449 d	0.590872 d	-0.366981
RSM	1.054551 d	0.590872 d	-0.359007
RNG $k-\epsilon$	1.154157 d	0.566336 d	-0.357193

Table 3-18: Hydrofoil turbulence model influence

(a) $k-\omega$ SST - BES **(b)** $k-\omega$ SST - TES

(c) $k-\epsilon$ - BES **(d)** $k-\epsilon$ - TES

(e) $k-\omega$ - BES **(f)** $k-\omega$ - TES

(g) RSM **(h)** RSM

(i) Laminar **(j)** RNG $k-\epsilon$

Figure 3-14: Hydrofoil density and liquid volume fraction contours - turbulence model influence. The x axis dimensions are in metres. The quantities plotted are averaged.

Case	Δ Cav. Length	Δ Cav. Onset	$\Delta C_{p,min}$
		BES	
$k-\epsilon$	-0.064533 d (-3.14%)	0.010990 d (1.90%)	0.001143 d (-0.32%)
$k-\omega$	-0.054062 d (-2.63%)	0.027290 d (4.73%)	0.000933 d (-0.26%)
RSM	-0.155182 d (-7.56%)	0.046292 d (8.02%)	0.001200 d (-0.34%)
Laminar	-0.021880 d (-1.07%)	0.021880 d (3.79%)	0.001647 d (-0.46%)
		TES	
$k-\epsilon$	0.010104 d (0.88%)	0.024536 d (4.33%)	-0.003010 d (0.84%)
$k-\omega$	0.117292 d (10.16%)	0.024536 d (4.33%)	-0.010377 d (2.91%)
RSM	-0.099606 d (-8.63%)	0.024536 d (4.33%)	-0.002403 d (0.67%)
RNG $k-\epsilon$	-0.000000 d (-0.00%)	-0.000000 d (-0.00%)	-0.000588 d (0.16%)

Table 3-19: Hydrofoil turbulence model influence Variation

3-3 2D Venturi : Inducer blade passage cavitating flow

An internal flow (bounded) through a 2D Venturi represents a simplified form of flows through inducer blade passages. This flow has been experimentally and numerically investigated by the research group at CREMHyG laboratory in Institut Polytechnique de Grenoble [25] The domain and mesh are shown in figure 3-15. The fluid used is Freon R-114 at a reference temperature of ≈ 293 K.

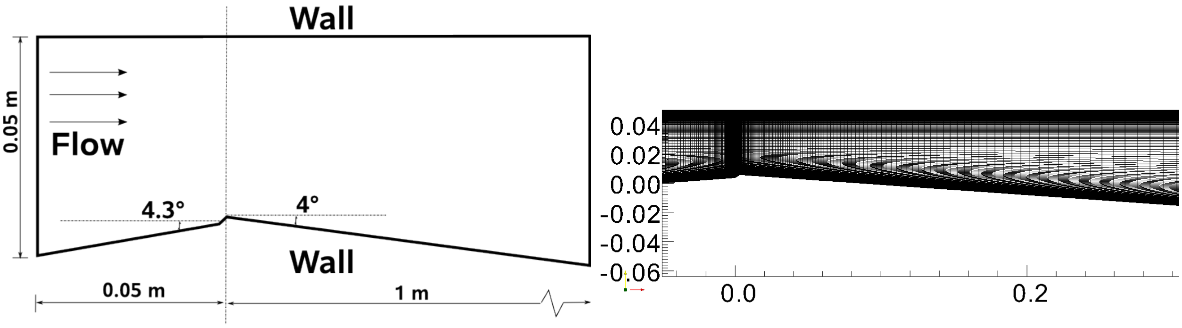

(a) Domain and Boundaries **(b)** Mesh

Figure 3-15: 2D Venturi domain, boundary conditions, and mesh

The two-dimensional setup of the Venturi is achieved by setting the Z-axis to be one cell deep. The top and bottom surfaces are treated as walls and the left and right surfaces are treated as inlet and outlet respectively. The ambient pressure is set at 265300 Pa. Almost all the parameters used are replicated from [25]. The inlet velocity is set at 14.4 m/s and the density is set at 1470.6 kg/m^3. The baseline configuration parameters are listed in table 3-20. The height of the domain at the inlet is 0.05 m. The divergence angle is 4° and the convergence angle is 4.3°. A small wedge of size 0.2 mm is placed between the converging and the diverging sections to fix the point of cavitation. The mesh uses a linear grading of points so that the maximum resolution lies near the small wedge and the wall region near that. A no slip boundary condition is applied at the walls. For the turbulence models, the turbulent intensity is set at 5% and the turbulent kinetic energy at 0.7776 m^2/s^2. For the $k-\omega$ SST formulation, the ω is set at 3219.938 s^{-1} based on the turbulent mixing length of 0.0005 m.

The reference parameters are listed in table 3-20.

Parameter	Value
Fluid	R-114 (1,2-Dichlorotetrafluoroethane)
Throat size, [m]	0.04424
Ambient Pressure, P_∞ [Pa]	265300
Cavitation No. σ [-]	0.55
Freestream Velocity, U_∞ [m/s]	14.4
Freestream Density, ρ_∞ [kg/m^3]	1470.6
Reynolds No, Re [-]	18.4×10^6
liquid Dyn. Viscosity, μ_l [Pa-s]	2.869×10^{-3}
Vapour Dyn. Viscosity, μ_v [Pa-s]	1.0527×10^{-4}
Saturation Pressure, P_{sat} [Pa]	181100
Liquid Saturation Density, $\rho_{l,sat}$ [kg/m^3]	1470.3
Vapour Saturation Density, $\rho_{v,sat}$ [kg/m^3]	13.521
Liquid Compressibility, ψ_l [s^2/m^2]	3.07344×10^{-6}
Vapour Compressibility, ψ_v [s^2/m^2]	7.27525×10^{-5}
Turbulence Model	$k-\omega$ SST
Turbulence Intensity, I [-]	0.05
Turbulent Kinetic Energy, k [m^2/s^2]	0.7776
Turbulent Mixing Length, l [m]	0.0005
Specific Dissipation, ω [s^{-1}]	3219.938
Flow Solver	TES
Courant No (Max)	0.45
Acoustic Courant No (Max)	50
Time step, Δt [s]	1×10^{-6}

Table 3-20: 2D Venturi - reference parameters

First the optimal mesh with converged cavitation parameters is selected after simulations with three different resolutions. That is followed by the setting up of a baseline case. Then the operating fluid and turbulence model influence tests on cavitation parameters are carried out. Owing to large computational costs, numerical stiffness, and late convergence, the simulations using BES are not carried out and only the TES simulations are done. The sensitivities of cavitation parameters are quantified and analysed by comparing the results the baseline case.

Oscillations of the attached cavitation bubble is observed during experiments. However, in our simulations the bubble oscillations are not clearly visible. The primary cause is that the two-equation models tend to over-predict the turbulent viscosity. The over-prediction of μ_t leads to the prevention of the formation of re-entrant jet and thus leads to stable cavities. Reboud et al [22] proposed an empirical correction to limit the eddy viscosity.

3-3-1 Grid convergence

The grid convergence of results is tested for by using three mesh resolutions: coarse, nominal, and fine meshes to find the optimal resolution for further analyses. The parameters are listed in table 3-21. The initial transient solutions are mapped from the nominal mesh onto the coarse and the fine meshes in order to save valuable simulation time and memory. The initial flow transients which lead to inaccurate averaging of results are removed. Table 3-21 lists the total mesh points and y^+ values for different resolutions.

Case	Points	y^+_{wall}	u^+_{wall}
Coarse	16472	60	10.50
Baseline	65142	38.5	9.41
Fine	259082	24	8.26

Table 3-21: 2D Venturi grid convergence parameters

The coarse and fine meshes predict cavitation lengths which are ~7% higher and ~0.017% lower than the nominal mesh cavitation length respectively. The cavitation length predicted using the nominal and fine meshes lie within the range of 0.075 - 0.08 m predicted by the Grenoble group [25]. The drop in liquid volume fraction is captured better as the y^+ decreases. This is expected because the finer resolution leads to better interpolation of values. However, the global parameter, cavitation length, differs by a negligible margin between the baseline and fine meshes. The liquid volume fraction distribution patterns are similar among all meshes. Overall, the variation of cavitation lengths due to the change in grid resolution is minor for coarse grid and negligible for the fine grid. Thus, the nominal resolution with a y^+ = 38.5 is used for further analyses. The simulations using the fine mesh take 4× more time than the nominal mesh simulation time.

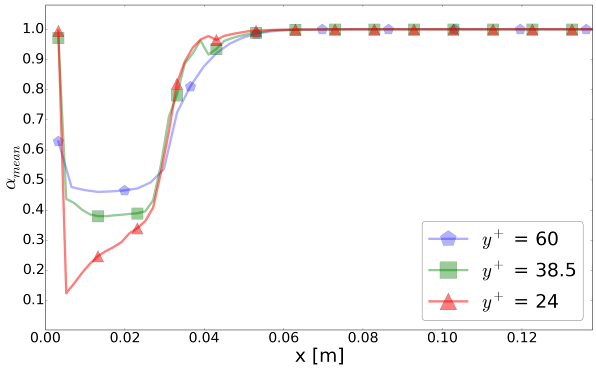

Figure 3-16: Liquid volume fraction distribution in a 2D Venturi are shown for TES grid convergence analysis.

Case	Cavity Length
$y^+ = 60$	0.082860 m
$y^+ = 38.5$	0.077387 m
$y^+ = 24$	0.077374 m

(a) Cavitation lengths

Case	Δ Cav. Length
$y^+ = 60$	0.005473 m (7.07%)
$y^+ = 24$	-0.000013 m (-0.017%)

(b) Percentage variation

Table 3-22: 2D Venturi cavity lengths - grid convergence

3-3-2 Baseline case

A baseline configuration is setup based on the nominal mesh resolution, geometry of the domain according to the literature, and the reference parameters listed in table 3-20. Figure 3-17 shows the mean relative pressure distribution and the mean liquid volume fraction distribution. The cavity length obtained during experiments is 75-80 mm [25]. The cavity length predicted by the simulation is 0.077387 m. The cavity length is calculated by taking the distance along the the lower wall over which the liquid volume fraction stays below 1.

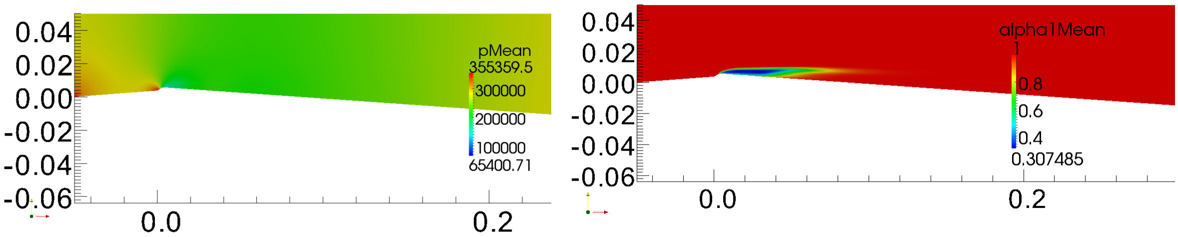

(a) Mean relative pressure distribution (Pa) (distance in m)

(b) Mean liquid volume fraction distribution

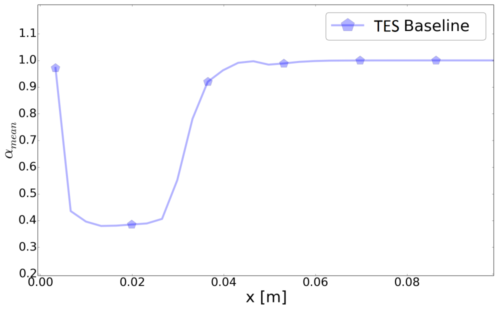

(c) α_{mean} vs x

Figure 3-17: Mean relative pressure and liquid volume fraction distribution for the baseline case of cyrogenic internal flow through a 2D Venturi are shown in this figure. Figures (a) and (b) show the distribution of mean relative pressure and liquid volume fraction respectively, over the bottom surface of the Venturi downstream of the throat, for the modelled TES baseline case. Figure (c) shows the liquid volume fraction vs axial distance. The cavity length calculated has a value of 0.077387 m

The influences of operating fluid and turbulence model are analysed in the following sections.

3-3-3 Operating fluid influence

Similar to the hydrofoil, in this section, we test the effect of change in operating fluid on cavitation prediction. We use LH2 and LO2 as the operating fluids and compare the calculated parameters with the baseline configuration (R-114). The baseline properties are given in table 3-20. The cavitation number and the ambient pressure are held constant while the rest of the parameters are subject to change. The parameters for LH2 and LO2 are listed in table 3-23. All data are obtained from [61] for LH2 and [62] for LO2.

Parameter	Value	Value
Fluid	liquid Hydrogen (LH2)	liquid Oxygen (LO2)
Ambient Pressure, P_∞ [Pa]	265300	265300
Ambient Temperature, T_∞ [K]	18	80
Cavitation No. σ [-]	0.5	0.5
Freestream Velocity, U_∞ [m/s]	109.007	28.105
Freestream Density, ρ_∞ [kg/m^3]	73.619	1192.5
Reynolds No, Re [-]	21.673×10^6	5.512×10^6
liquid Dyn. Viscosity, μ_l [Pa-s]	1.634×10^{-5}	2.6859×10^{-4}
Vapour Dyn. Viscosity, μ_v [Pa-s]	9.3507×10^{-7}	6.1260×10^{-6}
Saturation Pressure, P_{sat} [Pa]	46602	30123
liquid Saturation Density, $\rho_{l,sat}$ [kg/m^3]	73.377	1190.9
Vapour Saturation Density, $\rho_{v,sat}$ [kg/m^3]	0.6653	1.4684
liquid Compressibility, ψ_l [s^2/m^2]	7.1794×10^{-7}	1.0256×10^{-6}
Vapour Compressibility, ψ_v [s^2/m^2]	8.58575×10^{-6}	3.5279×10^{-5}
Turbulence Intensity, I [-]	0.05	0.05
Turbulent Kinetic Energy, k [m^2/s^2]	44.56	2.9622
Turbulent Mixing Length, l [m]	0.0005	0.0005
Specific Dissipation, ω [s^{-1}]	24374.69	6284.56

Table 3-23: 2D Venturi LH2 and LO2 Parameters

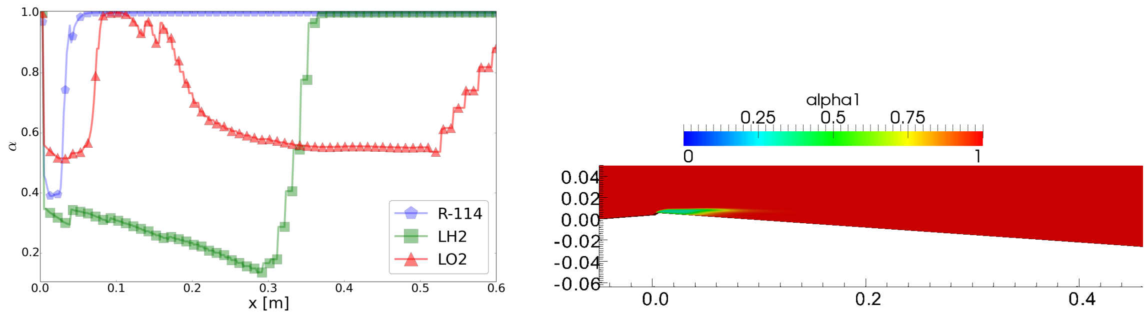

(a) Volume fraction distributions **(b)** R-114

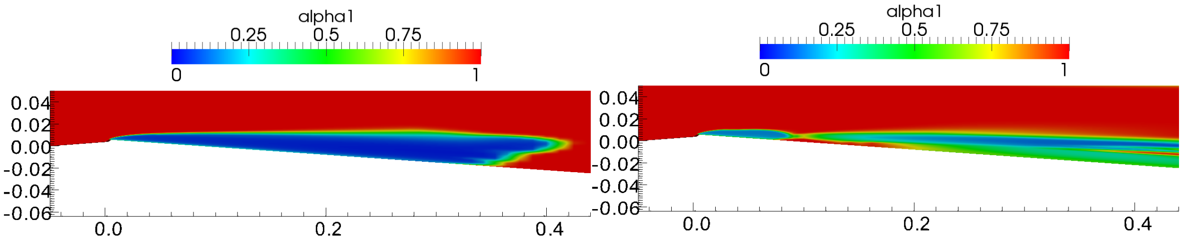

(c) LH2 **(d)** LO2

Figure 3-18: Liquid volume fraction distribution and contours in a 2D Venturi for R114, LH2, and LO2 - operating fluid influence

Case	Cavity Length
R-114	0.077387 m
LH2	0.365298 m
LO2	0.088254 m

(a) Cavity lengths

Case	Δ Cav. Length
LH2	0.287911 m (372.04%)
LO2	0.010867 m (14.04%)

(b) Cavity lengths % variations

Table 3-24: 2D Venturi - cavity lengths and their variations for LH2 and LO2

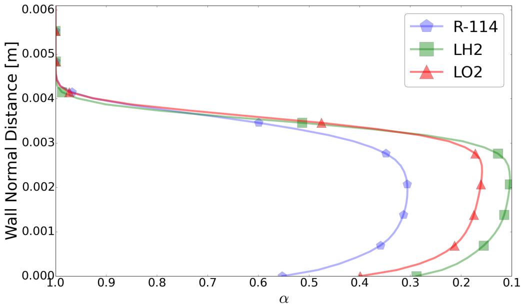

(a) Station 1 : x = 0.014 m

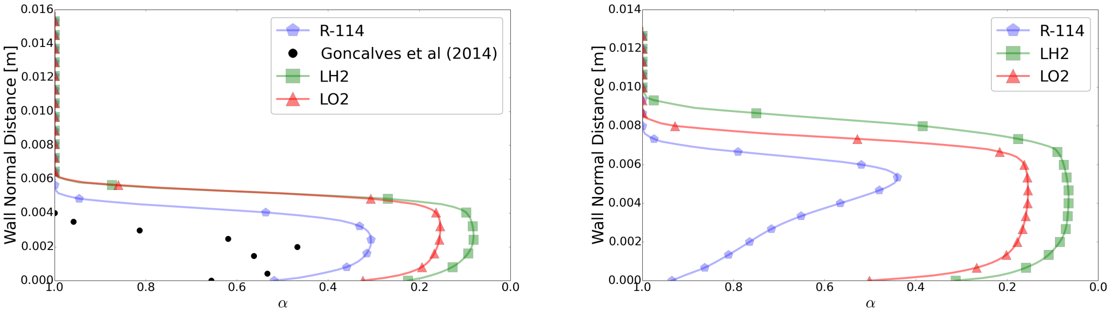

(b) Station 2 : x = 0.024 m **(c)** Station 3 : x = 0.048 m

Figure 3-19: 2D Venturi liquid volume fraction α vs Wall Normal Distance for R-114, LH2, and LO2. The experimental values are lower than the numerical values for R-114 because the thermodynamic effects are not included in the numerical calculations.

There is a large variation in cavity volume and length predictions among the fluids. The LH2 and LO2 cavity lengths vary by 372.24% and 14.04% respectively (table: 3-24). However, the cavity length of 0.088254 m associated with LO2 is only the initial part of the attached bubble. There is a detachment from the wall and a wake grows downstream as the ambient pressure rises. If one has to consider the entire region, the cavity length extends upto 0.992 m [$\sim$1180% change!] (see figure 3-18). The liquid volume fraction values used in the figures are instantaneous values at the last time step. Owing to the constraint on the conservation of mass flow rate in a bounded flow problem plus the difference in liquid-vapour density ratios among the operating liquid, there exists a large difference in cavitation length predictions. The liquid-vapour density ratios for R-114, LH2, and LO2 are $\sim$108,$\sim$110, and $\sim$812 respectively. Although the density ratios are similar for R-114 and LH2, the inlet velocities are much different. The R-114 case uses 14.4 m/s and LH2 case uses 109 m/s. Different velocities are input in order to maintain the cavitation number constant. The change in operating fluid has a drastic effect on cavitation in bounded flow problems. Thus, usage of similar blade profiles and spacings for different operating fluids will result in catastrophic changes in cavity formation.

3-3-4 Turbulence model influence

Turbulence model influence analysis is pursued with the same set of turbulence models as that of the hydrofoil. All simulations are carried out only using TES. The parameter settings of the different turbulence models are listed in table 3-25. The $k-\epsilon$, RSM, and RNG-$k-\epsilon$ models use standard wall functions for the evaluation of k and ε near the wall. The $k-\omega$ and SST models the standard wall functions for k and ω. The laminar formulation uses a dummy turbulence model which does not use any wall function and supplies a zero value for turbulent kinetic energy, turbulent viscosity, Reynolds stress tensor etc.

Turbulence Models	k	ω	R	ϵ
$k-\omega$ SST (Base)	0.7776	3219.938	-	-
$k-\epsilon$	0.7776	-	-	225.34
$k-\omega$	0.7776	3219.938	-	-
Reynolds Stress Model (LRR)	0.7776	-	(0.7776 0 0 0.3888 0 0.3888)	225.34
RNG $k-\epsilon$	0.7776	-	-	225.34
Laminar	0	0	0	0

Table 3-25: 2D Venturi - turbulence model influence cases

All turbulence models yield different results (figure 3-20). The quantity plotted is the instantaneous liquid volume fraction at the last time step. Nevertheless, there are no oscillations observed. The $k-\epsilon$ model yields a cavitation length which is 41% larger than that of the $k-\omega$ SST model. The $k-\omega$ however yields 15% less. Although, both $k-\omega$ and $k-\epsilon$ have similar liquid volume fraction distribution profiles with respect to the $k-\omega$ SST case.

The RSM model and the RNG $k-\epsilon$ model yield very high cavitation lengths when compared to the baseline case. The difference is in the order of 0.380983 m (492.31%) and 0.412731 m (533.33%) respectively for RSM and RNG $k-\epsilon$. The possible cause for RSM behaviour is that the modelled pressure-strain correlation is very sensitive to adverse pressure gradients.

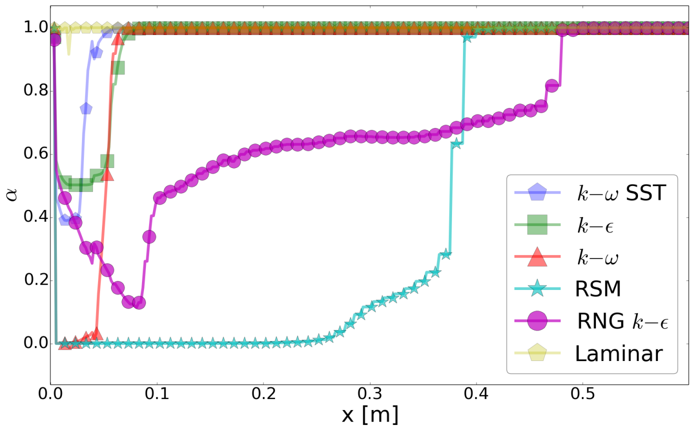

(a) α vs x

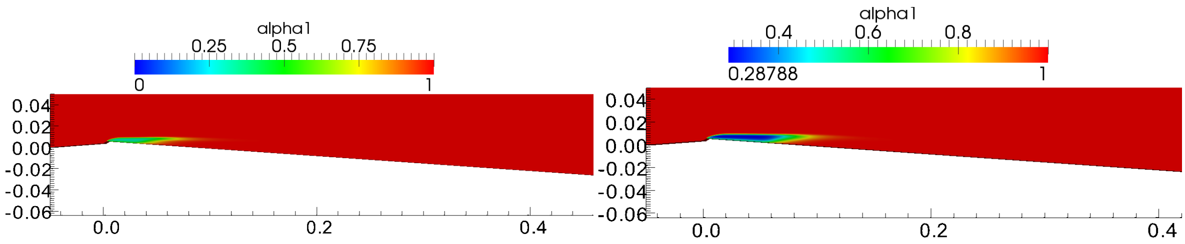

(b) $k-\omega$ SST

(c) $k-\epsilon$

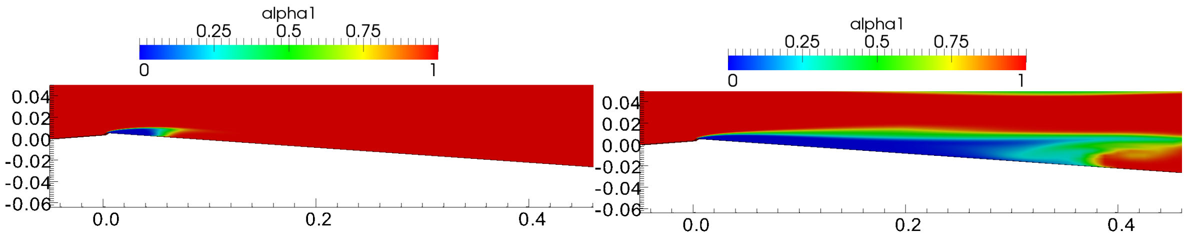

(d) $k-\omega$

(e) RSM

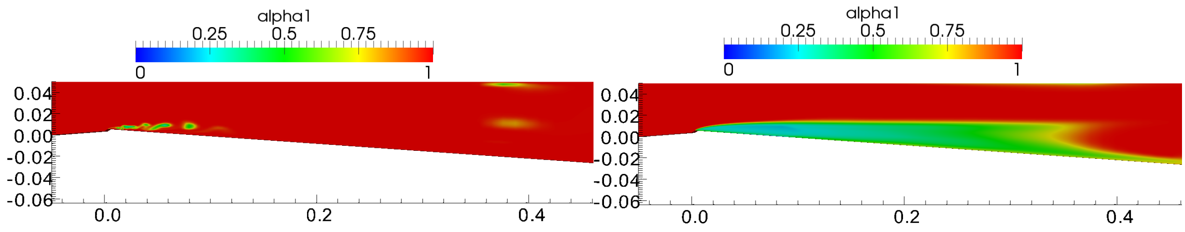

(f) Laminar

(g) RNG $k-\epsilon$

Figure 3-20: 2D Venturi α vs x distribution and contours for $k-\omega$ SST, $k-\epsilon$, $k-\omega$, RSM, and RNG-$k-\epsilon$ models - turbulence model influence. Significant variation in cavitation predictions are observed. The $k-\omega$ SST and $k-\omega$ models yield cavitation lengths that are similar to the experimental values (75-80 mm). However, their volume fraction distributions are different. The laminar simulation does not yield an attached cavitation bubble. The RSM and RNG $k-\varepsilon$ simulations show drastic changes.

Case	Cavity Length
$k-\omega$ SST	0.077387 m
$k-\epsilon$	0.109136 m
$k-\omega$	0.065481 m
RSM	0.458370 m
RNG $k-\epsilon$	0.490118
Laminar	0.119057 m

(a) Cavity length

Case	Δ Cav. Length
$k-\epsilon$	0.031749 m (41.03%)
$k-\omega$	-0.011906 m (-15.38%)
RSM	0.380983 m (492.31%)
RNG $k-\epsilon$	0.412731 m (533.33%)
Laminar	0.041670 m (53.85%)

(b) Change in cavity Length

Table 3-26: 2D Venturi cavity lengths and their variation for various turbulence models. Drastic changes are observed in cavitation length predictions among all turbulence models as well as laminar simulation.

Owing to the presence of walls in close proximity, the pressure reflected off the wall impacts the redistribution of turbulent kinetic energy in the flow. The increase in kinetic energy leads to the increase in the magnitude of the wall reflection term, which in turn leads to the increase in shear stress parallel to the wall. Thus, there is an elongation in the cavity. Another contributing factor is the increase in the velocity of the liquid phase which affects the slow part of the pressure-strain correlation, thus leading to further pressure drop and increased stretching of the vapour bubble. The behaviour in RNG $k-\varepsilon$ simulation can be explained as follows: The RNG $k-\varepsilon$ model differs from standard $k-\varepsilon$ formulation by using rigorous statistical technique (see section 2-3-2). A noticeable difference is the usage of differential turbulent viscosity and the constant $C^*_{\varepsilon 2}$ instead of $C_{\varepsilon 2}$. Also, the $C_{\varepsilon 2}$ value is lower for the RNG formulation. This leads to the decrease in production rate of k and dissipation rate ε. This effect reduces the value of μ_t and thereby leads to larger and more unstable cavities.

The laminar simulation does not yield an attached cavitation bubble like the rest of the models. In fact, it results in small bubbles generated at the wedge. The distribution of liquid volume fraction in the wall normal direction at three different locations (0.014 m, 0.024 m, 0.048 m) are shown in figure 3-21 and the corresponding cavity heights are listed in table 3-27. The variation in the α distribution along the wall normal direction is significant among the turbulence models. This analysis proves that the choice of the turbulence model carries very high importance while numerically simulating inducer flows.

Case	Cav Height S1	Cav Height S2	Cav Height S3
$k-\omega$ SST	0.004701 m	0.005645 m	0.008261 m
$k-\epsilon$	0.004977 m	0.006128 m	0.007995 m
$k-\omega$	0.004148 m	0.005967 m	0.009327 m
RSM	0.004562 m	0.006612 m	0.010793 m
RNG $k-\epsilon$	0.005530 m	0.007903 m	0.012392 m

Table 3-27: 2D Venturi - Height of at cavitation bubble at 3 different stations

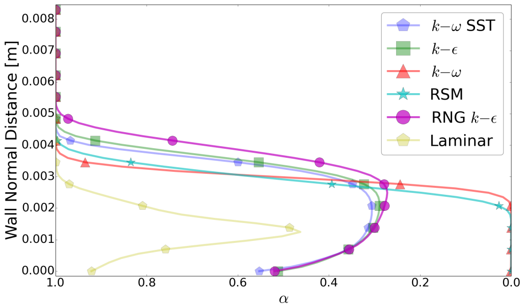

(a) Station 1 : x = 0.014 m

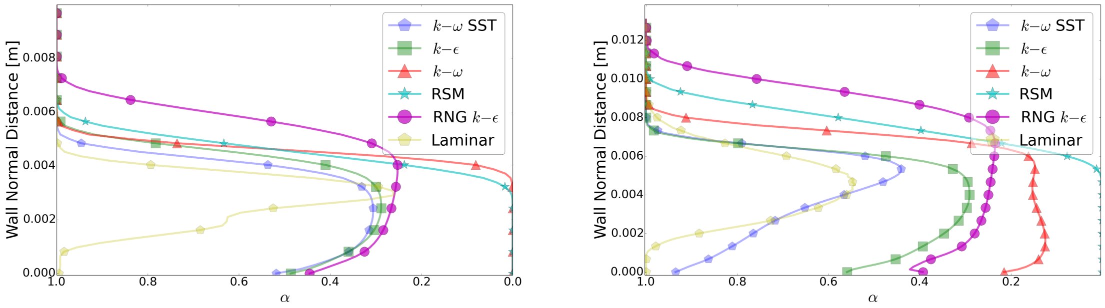

(b) Station 2 : x = 0.024 m

(c) Station 3 : x = 0.048 m

Figure 3-21: 2D Venturi liquid volume fraction α vs Wall Normal Distance for $k-\omega$ SST, $k-\epsilon$, $k-\omega$, RSM, and RNG $k-\epsilon$ models. Strong variations are observed among the turbulence models. The height of the cavitation bubble at all three locations are much higher for RNG $k-\varepsilon$ model and RSM. The Laminar simulation does not yield an attached cavity but rather a few bubbles.

3-4 Propeller : 3D rotational cavitating flow

The three-dimensional rotating flow over a canonical ship propeller is simulated to analyse the effect of turbulence models on phase distribution in rotating domains. The propeller geometry has four blades attached to the hub. The diameter of the propeller is 0.22 m. The propeller is placed inside a cylindrical casing which has a diameter of 0.24 m and a height of 0.14 m. The outer cylinder that is used has a diameter of 0.6 m with a total height of 1 m. The geometry and mesh of the propeller case is illustrated in figures 3-22a and 3-22b.

The meshing of the geometry is done using `blockMesh` utility and the surface meshing of the propeller is done using `SnappyHexMesh` in OpenFOAM. The total number of points amount to 656083. The snappyHexMesh utility generates 3-dimensional meshes containing hexahedra (hex) and split-hexahedra (split-hex) automatically from triangulated surface geometries in Stereolithography (STL) format. The mesh approximately conforms to the surface by iteratively refining a starting mesh and morphing the resulting split-hex mesh to the surface. An optional phase will shrink back the resulting mesh and insert cell layers. The specification of mesh refinement level is very flexible and the surface handling is robust with a pre-specified final mesh quality. It runs in parallel with a load balancing step every iteration [63].

The propeller hub and the blades rotate while the cylinder casing and the external cylindrical domain remain stationary. The rotating zones are identified and a solid body rotation functionality is applied to the rotating zones with a specified rotational velocity in the anti-clockwise direction. Since both rotating and stationary parts are involved, Arbitrary Mesh Interface (AMI) patches are created as sliding interfaces between them. AMI is a technique that allows simulation across disconnected, but adjacent, mesh domains. The domains can be stationary or move relative to one another. Since sliding interfaces are used for rotating machinery problems, separate meshes are used for rotating and/or static regions of geometry, which are coupled at patch boundaries through the cyclicAMI boundary condition.

For the baseline setup, we use the $k-\omega$ SST turbulence model. The 3D propeller case is only tested for the phase distribution owing to the change in turbulence models. The fluid under consideration is water flowing with a freestream velocity of 15 m/s from the inlet (top portion indicated as X-Z plane in figure 3-22a). The rotational speed set for the propeller is 53.05 rad/s or 515 rpm in the anti-clockwise direction. The ambient pressure is set at 1 bar, the temperature at 298 K, and the density at 1000 kg/m^3. The solver used is the Transport Equation Solver with the capability to handle rotating meshes. The cavitation number based on freestream velocity is set as $\sigma = 0.868$ and the cavitation number based on rotational velocity of the propeller is set as $\sigma_\Omega = 5.738$. The Reynolds number based on the propeller diameter and the rotational velocity is 2.885×10^6. The simulation parameters are tabulated in table 3-28

The analysis of phase distribution is carried out by plotting the contour of a threshold value of the liquid volume fraction and also by plotting the liquid volume fraction distribution at a particular slice plane. A slice plane is obtained with its centre at the origin. The schematic of the slicing is shown in figure 3-23

Unlike the other cases, cavitation length cannot be directly computed. The other cases involved 2D geometries with fixed position. In the case of a propeller, probe points have to be placed along the surface of the 3D rotating propeller blade. This could not be achieved with the available tools. Also, analysing the volume of cavitation bubble is relevant and

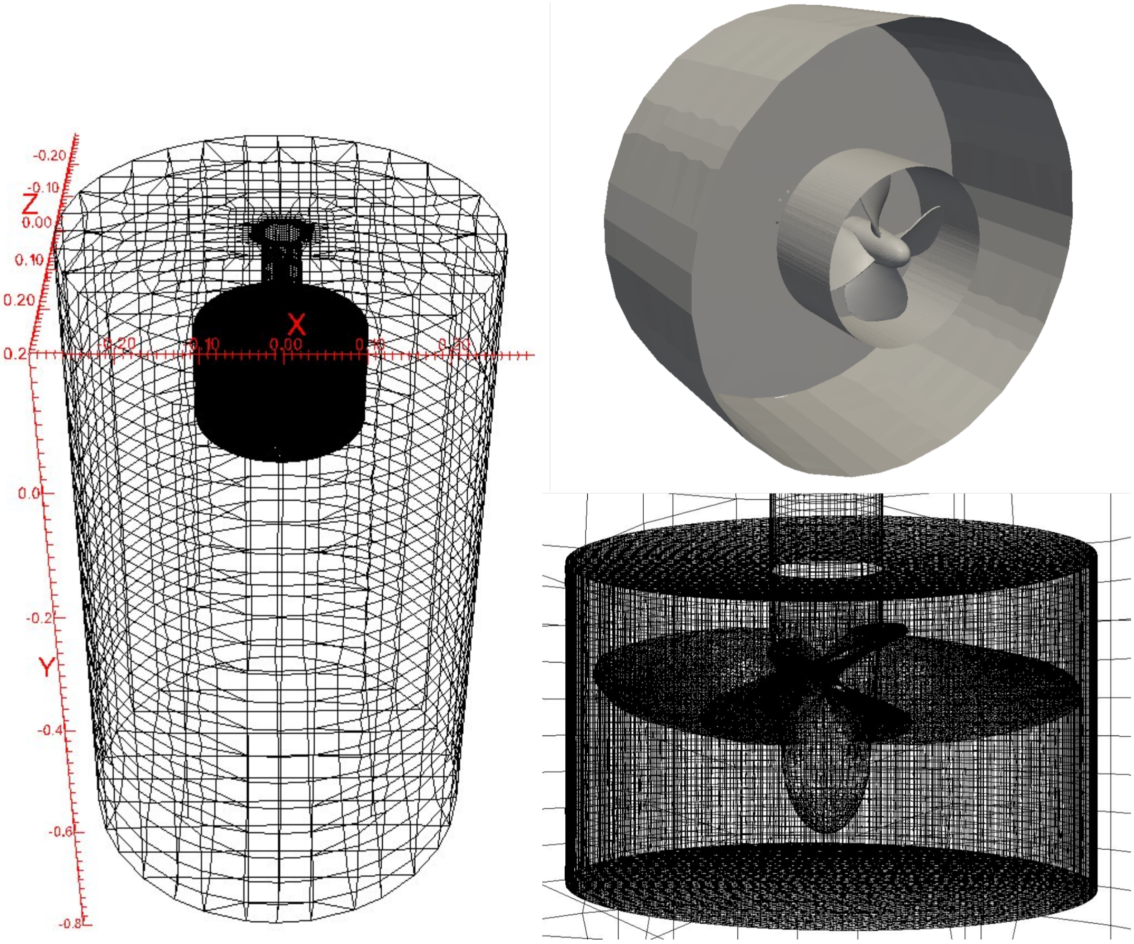

(a) Overall domain mesh **(b)** Propeller geometry and mesh

Figure 3-22: 3D Propeller mesh

Parameter	Value
Fluid	Water
Propeller Tip-tip diameter, [m]	0.22
Ambient Pressure, P_∞ [Pa]	100000
Cavitation No. (freestream) σ [-]	0.868
Cavitation No. (rotation) σ_Ω [-]	5.738
Freestream Velocity, U_∞ [m/s]	15
Freestream Density, ρ_∞ [kg/m^3]	1000
Reynolds No, Re [-]	2.885×10^6
liquid Dyn. Viscosity, μ_l [Pa-s]	9.0×10^{-4}
Vapour Dyn. Viscosity, μ_v [Pa-s]	9.862×10^{-6}
Saturation Pressure, P_{sat} [Pa]	2300
liquid Saturation Density, $\rho_{l,sat}$ [kg/m^3]	1000
Vapour Saturation Density, $\rho_{v,sat}$ [kg/m^3]	0.02308
Turbulence Model	$k - \omega$ SST
Turbulent Kinetic Energy, k [m^2/s^2]	0.06
Specific Dissipation, ω [s^{-1}]	9.1667
Flow Solver	Dynamic Mesh TES
Courant No (Max)	2
Mesh points	656083
Time step, Δt [s]	1×10^{-5}

Table 3-28: 3D Rotating Propeller - baseline simulation parameters

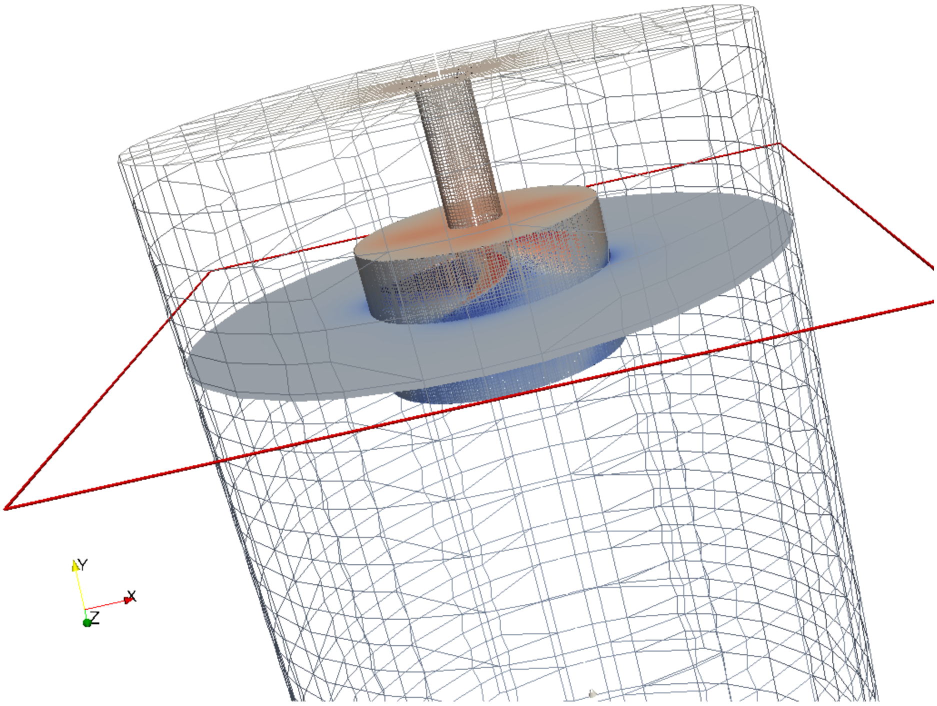

Figure 3-23: 3D Propeller - slice plane location

useful in a 3D simulation. This volume, however, is not easily quantifiable because of the complex nature of the flow. Thus, we have to compare the models by qualitatively assessing the liquid-volume fraction contours. The rotational speed used is relatively low and attached sheet cavitation on the propeller blade surfaces are clearly visible. The contours obtained using the $k-\omega$ SST simulations, at the last time step, are shown in figure 3-24

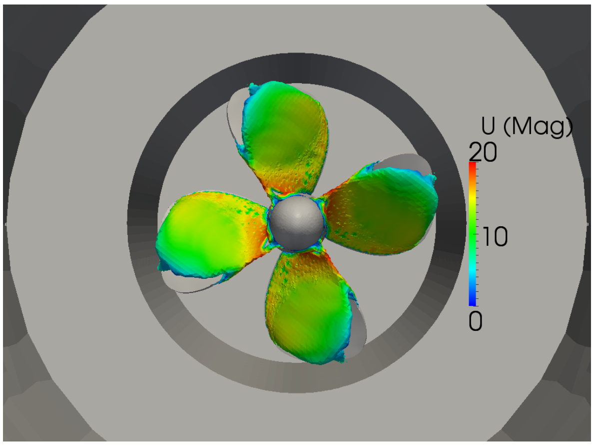

(a) 3D Contour of $\alpha_l = 0.40$

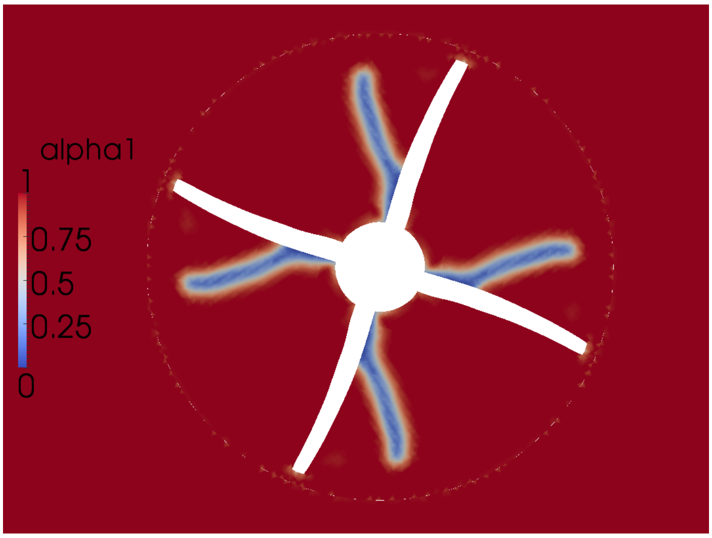

(b) Slice place α_l distribution

Figure 3-24: 3D Propeller - baseline liquid volume fraction distribution. Fig (a) Attached sheet cavitation on the blade surface is clearly visible. The threshold value for the α contour is 0.5 and the contour is coloured by the velocity magnitude. The velocity is high near the hub of the propeller blade. Fig (b) Liquid volume fraction distribution at the slice plane is shown; detachment of the cavity is observed. The rotation in figure (a) is clockwise and in figure (b) is anti-clockwise.

3-4-1 Turbulence model influence

The turbulence models that are under consideration are $k-\omega$ SST, $k-\varepsilon$, $k-\omega$, RNG $k-\varepsilon$, and Launder-Reece-Rodi Reynolds stress model. We qualitatively observe cavitation topology (phase-distribution) and analyse how different each turbulence model estimates it. Apart from using the baseline rotational speed of 515 rpm, we test the effect of increased rotational speed on the phase distribution.

Owing to the complexity of the geometry, the sliding mesh, and a small time scale, the actual simulation time for each case is a lot longer (∼18 hours). The primary focus of this analysis is not only highly accurate modelling of the flow but to analyse the change in phase-distributions due to change in turbulence models. The inlet values for turbulent kinetic energy k, dissipation rate ε, specific dissipation rate ω, and Reynolds stress components R are listed in table 3-29

Turbulence Models	k	ω	R	ϵ
$k-\omega$ SST (Base)	0.06	9.1667	-	-
$k-\epsilon$	0.06	-	-	0.0495
$k-\omega$	0.06	9.1667	-	-
Reynolds Stress Model (LRR)	0.06	-	(0.06 0 0 0.03 0 0.03)	0.0495
RNG $k-\epsilon$	0.06	-	-	0.0495
Laminar	-	-	-	-

Table 3-29: Rotating Propeller - turbulence model influence Cases

The phase distribution is visualised in two ways. First, by plotting 3D contours over the blade surfaces, with a threshold value of $\alpha_l = 0.5$ for 515 rpm simulations and 0.05 for 20000 rpm cases. Second, by plotting the phase distribution over a two-dimensional slice plane at a specific location. The 3D contours are shown in figure 3-25 and 2D slice plots are shown in figure 3-26. Theoretically, Reynolds Stress Model inherently accounts for rotation and associated anisotropies. Thus, it should produce the most accurate results when compared to other models. However, the validity of results is not well known because of the lack of affirmative non-confidential literature for the same propeller geometry.

The turbulence models $k-\omega$ SST and $k-\varepsilon$ exhibit similar behaviour. However, a stark difference is observed in the case of $k-\omega$ model. These similarities and differences are due to their respective sensitivities towards adverse pressure gradients in the freestream region. The $k-\omega$ SST formulation uses blending functions and uses $k-\omega$ formulation near the wall and $k-\varepsilon$ formulation in the freestream region. $k-\omega$ model is very sensitive towards adverse pressure gradients in the freestream whereas $k-\omega$ SST and $k-\varepsilon$ are not. The RNG $k-\varepsilon$ model and RSM exhibit behaviours which differ moderately. RNG $k-\varepsilon$ model has improved predictions for flows with high streamline curvature with some improved accuracy for rotational flows. RSM inherently accounts for rotation and the associated anisotropies. These results again assert our inference from our previous analyses on the importance of turbulence modelling.

Rotation in flows is a major flow phenomenon that appears in turbomachinery. In the case of turbopumps, the rotational speed of the main impeller is very high. One of the leading causes for cavitation occurring in the inducer region is the high rotation speeds involved. However, modelling of the rotational flows is not simple and there are lots of challenges in predicting some of the specific flow features.

The standard two-equation models do not account for the rotation, however, the Reynolds stress model inherently accounts for these effects. Also, owing to the complex flow structure, the assumptions used in the two-equation models are no longer valid.

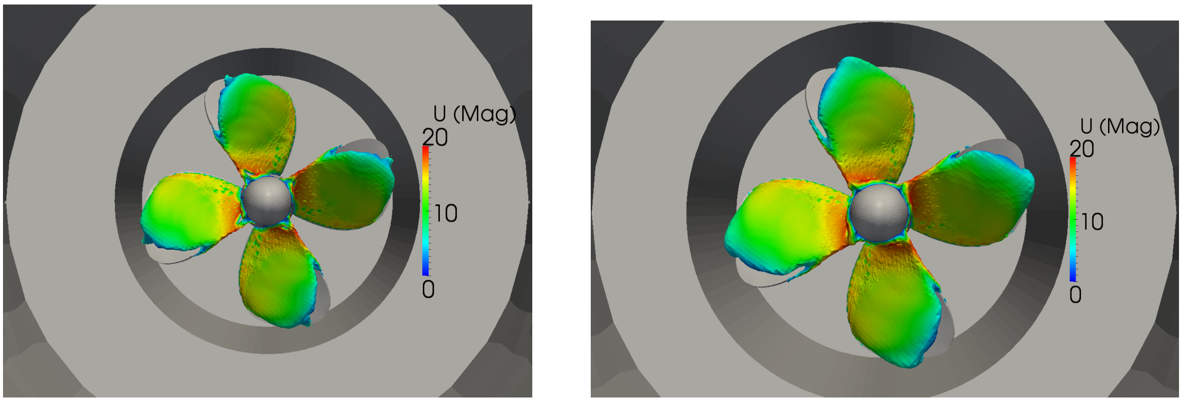

(a) $k-\omega$ SST **(b)** $k-\epsilon$

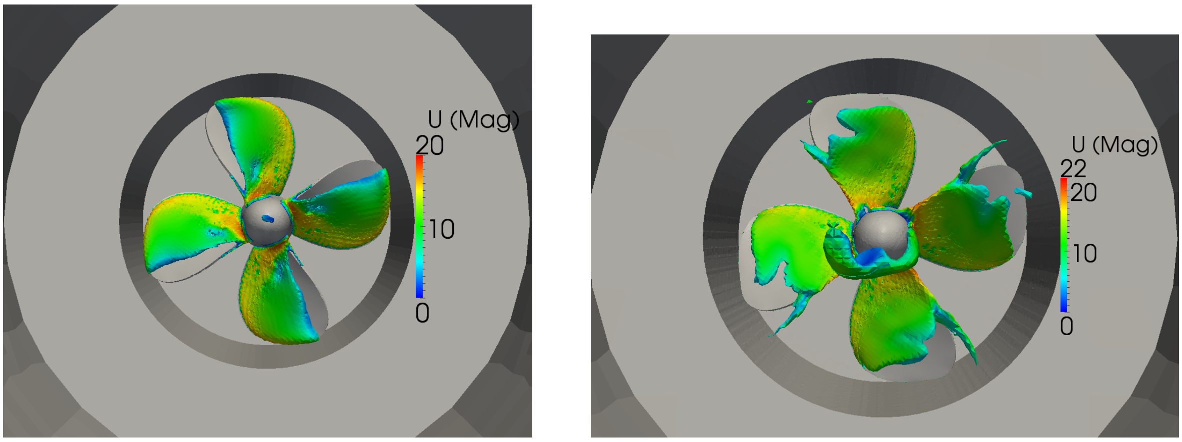

(c) $k-\omega$ **(d)** RSM

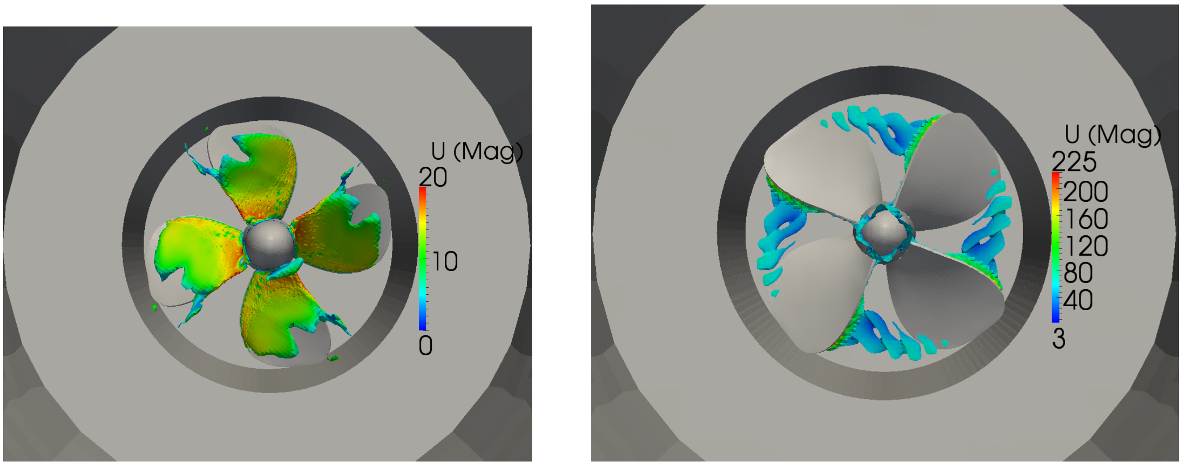

(e) RNG $k-\epsilon$ **(f)** RSM (rpm = 20000)

Figure 3-25: Rotating propeller phase distribution for contours, $\alpha = 0.5$ (515 rpm) and $\alpha = 0.05$ (20000 rpm) - Turbulence model influence. The direction of rotation is clockwise. Strong variations are observed among the turbulence models while predicting liquid volume fractions with the same value. The contours are coloured according to the magnitude of velocity. Drastic difference in contour is found when the rotational speed is increased to 20000 rpm

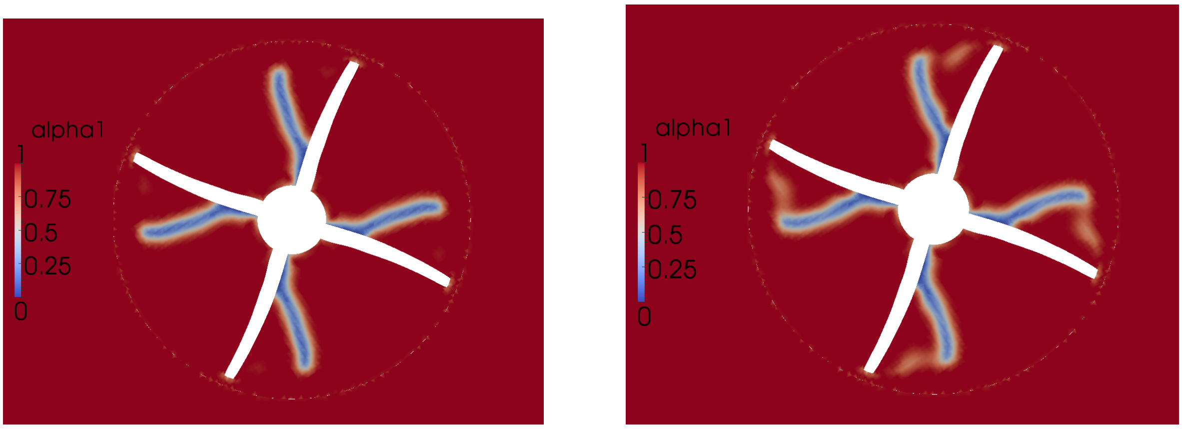

(a) $k-\omega$ SST **(b)** $k-\epsilon$

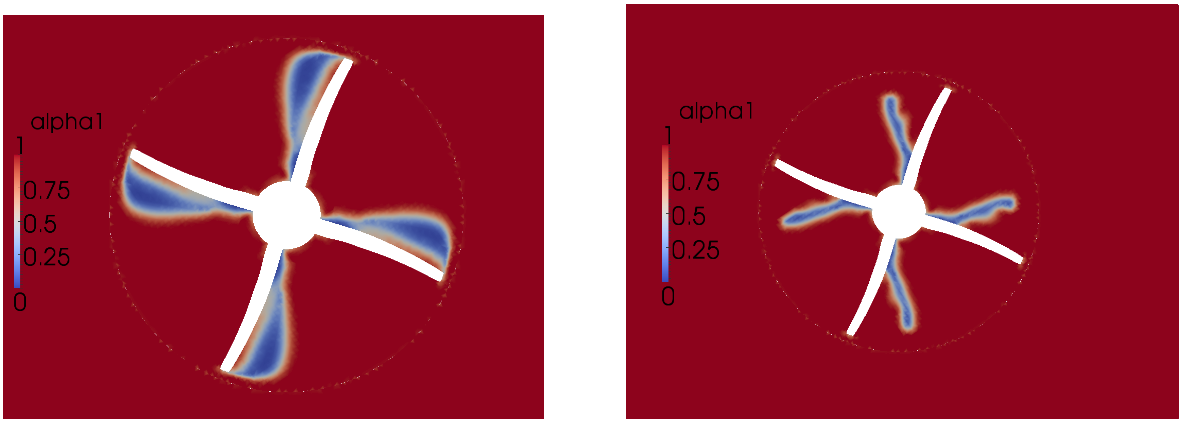

(c) $k-\omega$ **(d)** RSM

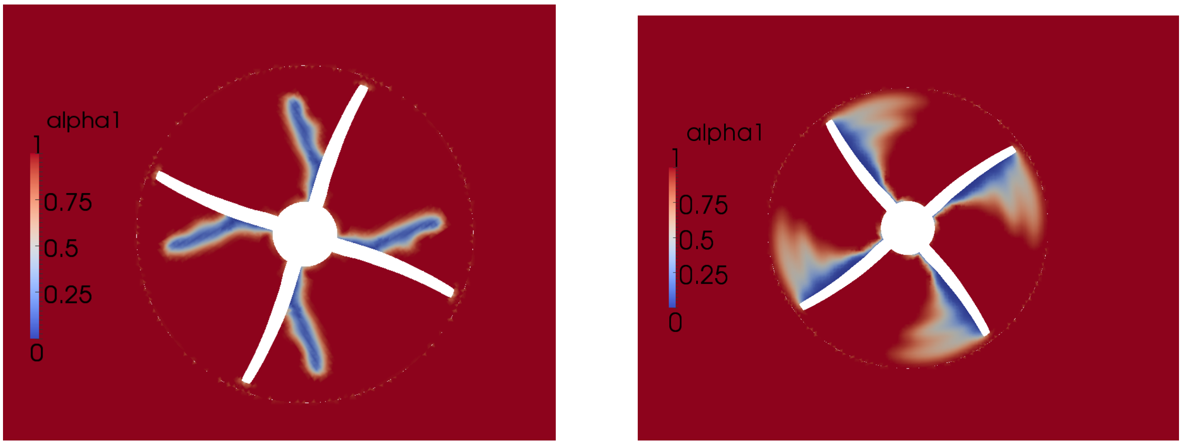

(e) RNG $k-\epsilon$ **(f)** RSM (rpm = 20000)

Figure 3-26: Rotating propeller : 2D liquid volume fraction countours on a slice plane - Turbulence model influence. The direction of rotation is anti-clockwise. Stark to moderate differences are observed among the turbulence models while predicting liquid volume fractions. For all models with the exception of $k-\omega$, bubble detachment from the blade surface is observed. This is due to $k-\omega$ model's sensitivity towards free-stream pressure gradients. The increase in rotational speed alters the liquid volume fraction distribution drastically.

The RSM provides information about all the stress components and account for the rotation, and inherently captures most of the flow phenomena. However, this comes at a price. Although the second moment closures are robust and account for the actual physics of the problem, discretisation and implementation of such models are very difficult. Also, the computational costs are higher compared to the simple turbulence models. Jakirlić et al [64] applied the RSM and two-equation models to developing and fully developed flows in axially rotating pipes, swirling flows in combustor geometries and in long pipes. They divulged some of the shortcomings of this model, for example, there is a wrong negative sign of the $\overline{u_i'u_j'}$ shear stress component, retention of concentrated vortex shape in tangential velocity profile for longer period than expected in pipe flow with a weak swirl, and untimely laminarisation in axially rotating pipes and cylinders.

The standard wall functions that are used for the treatment of wall boundary conditions cannot be used in the case of a rotating flow because it causes a strong deviation of the velocity profile from the logarithmic law. This results in the integration of the governing transport equations upto the wall boundary. Thus the models are prone to laminarisation.

The two-equation models have a linear relationship between the Reynolds stress and the mean rate of strain tensors. This implies that the eddy-viscosity is isotropic and the anisotropies of the Reynolds stress term are not accounted for. The rotation causes strong anisotropies in Reynolds stress term and the dissipation tensor, and also leads to a very high anisotropic eddy-viscosity. Thus, the baseline assumption is contradicted.

The eddy viscosity models require various modifications to account for the rotation. Some of them are based on the rotational Bradshaw-Richardson number and some of them are based on the different modelling techniques for the turbulent eddy viscosity. Although there is no direct inclusion of rotational effects in the dissipation ε equation, there are some indirect rotation effects on the dissipation term due to the anisotropies of the dissipation correlation ε_{ij}, which includes a term affected by the angular velocity.

In the case of RSM, the rotation term in the stress transport equation directly accounts for the effects of rotation on the anisotropy of the Reynolds stress term. It also indirectly influences the dynamics of the dissipation rate ε. Although the rotation effects are accounted for, it doesn't perform very well in the case of high rotational speeds.

The rotational effects reduce the energy dissipation rate ε because the energy transfer owing to the cascade mechanism (from larger eddies to smaller ones) is severely lowered. This has a direct impact on the kinetic energy and the Reynolds stresses.

Although there are many modifications to the turbulence models to account for rotation, they are ill suited for the rotational flow modelling in turbomachinery because of the rotation induces an an asymmetric influence on turbulence. Thus, turbulence modelling of rotational flows in order to capture most of the flow features and to account for all the anisotropies remains a challenge.

3-5 Conclusion

The analysis of the influence of turbulence models and other parameters in multiple flow regimes has yielded results which are of good scientific value. The following are the most important conclusions derived from the analysis.

- There is a significant variation between the results yielded by the individual solvers, the barotropic equation of state based BES and the liquid volume fraction transport based TES. The choice of the solver is of paramount importance. The BES formulation is such that the density is modelled only as a function of pressure and the dependence on other physical parameters are discarded. In the TES, only the cavitation source terms are modelled. Thus, TES is physically more representative of the problem, especially for cryogenic flows having low liquid-vapour density ratios.
- Turbulence modelling holds very high importance while simulating cavitating flows in bounded and non-bounded flow regimes.
- The impact of turbulence models on cavitation parameters are different while different flow solvers are used.
- Significant differences in cavitation lengths, topologies, onset distances, and pressure distributions are observed among turbulence models in bounded flow and rotational flow problems. In the case of non-bounded flows, the importance is relatively moderate. This also exerts the point that the turbulence modelling results are also heavily problem dependent.
- Theoretically, second moment closures provide the most physically accurate RANS closure which are computationally feasible [65]. Two-equation models, which use Boussinesq hypothesis, fail to effectively capture unsteady cavitation due to overestimation of turbulent viscosity. They also poorly account for flow and rotation induced anisotropies and multiphase interactions. However, they are widely validated, simple to implement, and have low computational costs.
- A universal RANS based turbulence model which can capture fluctuations, phase interactions, anisotropies, and rotational effects in all flow domains with an acceptable computational cost seems to be unavailable.
- The turbulence intensity, barotropic compressibility models, and cavitation models have negligible effect of cavitation prediction in this flow regime.
- The change in Reynolds number by an order of magnitude results in minor to moderate variations.
- When there is a change in operating fluid, large variations are observed in internal flows and minor variations are observed in external flows.

Chapter 4

Cavitation dynamics and turbulence-cavitation interaction

Until now, discussion on how the choice of turbulence models and other parameters affect cavitation prediction has been carried out. The upcoming analysis focuses on the effects of bubble dynamics on turbulence production and dissipation in the flow. To this extent, the Rayleigh-Plesset equation (2-4) is numerically solved, submitted to a variable pressure field, with and without thermal effects for a series of characteristic bubble sizes. The first set of analyses deals with the dynamics of individual bubbles of increasing initial radii flowing through two different pressure fields. The second analysis consists of multiple bubbles with the same initial radii simultaneously flowing through a three-dimensional rotating inducer geometry. Although the bubbles flow simultaneously, the process is assumed not to have any bubble-bubble interactions.

The goal of this chapter is to quantify, analyse, and understand the characteristics of bubble dynamics in cryogenic turbopump inducers and how they affect the turbulence in the flow. From section 2-1, one could understand that the bubble grows when the free-stream pressure drops and reaches its maximum size at the lowest pressure. When the pressure recovers, it collapses. This process is not always linear and it leads to oscillations of the bubble radius. In this chapter, the emphasis is placed on two quantities, 1. Radius ratio (R/R_o) which is reflective of the bubble length scale and 2. Bubble oscillation frequency which is the reciprocal of the time scale. Quantification and analysis of these are required to study their contribution, or lack thereof, to flow turbulence. The effect of bubble dynamics on turbulence has to be understood in order to implement physically accurate turbulence models which shall capture cavitation physics.

The turbulence in the flow is qualitatively understood by studying the velocity fluctuations that occur in the flow. The production of turbulent kinetic energy increases with the increase in velocity fluctuations as well as the mean shear in the flow. Consequently, the dissipation rate of the turbulent kinetic energy also increases. Considering a liquid flow with the presence of bubbles, where the liquid is the carrier phase and the bubbles are the dispersed phase, the sources of velocity fluctuations in the carrier phase are:

- Single phase turbulence: The fluctuations that result from an existing energy cascade fed by mean velocity gradients in the flow. This is also called shear-induced turbulence.
- Bubble oscillations & perturbations (pseudo-turbulence): Induced turbulence on the liquid phase near the liquid-bubble interface due to the relative motion of the bubble and oscillation of the bubble size.
- Small scale fluctuations in bubble wakes: The existence of wakes behind a bubble, when experiencing a drag force in the flow, leads to the production of small scale fluctuations which contribute to the turbulence in the flow. The work performed by drag force is equal to the energy dissipation in the wake.
- Interface deformation: Fluctuations caused due to the deformation of the liquid-vapour interface which occur due to accelerations, presence of shear, or the action of turbulent eddies. These depend upon the bubble size, surface tension, and liquid-vapour density ratio.

When the size of the bubbles are larger than the Kolmogorov length scale (the smallest length scale of eddies in the energy cascade mechanism; $\eta = \left({}^{\nu}/_{\varepsilon}\right)^{1/4}$), the carrier phase turbulence is affected by the presence of bubbles and their oscillations [66]. Depending on the flow conditions, the presence of bubbles could augment or attenuate the carrier phase turbulence. However, these oscillations do not directly contribute to turbulent fluctuations but rather indirectly as pseudo-turbulent fluctuations [66, 67, 68]. For example, when we have a laminar flow without any bubbles through a channel and when we record the velocity using a Pitot tube, we do not see any fluctuations. However, when there are bubbles present in the flow, theoretically there are no fluctuations (because the flow is laminar), however minor fluctuations will be recorded by the Pitot tube. When we extend this into a turbulent flow containing bubbles, the fluctuations that naturally occur in the turbulent flow are added with the fluctuations due to the presence of bubbles. Even stronger fluctuations occur when the bubbles oscillate (Figure 4-1).

Turbulence plays a major role in phase-distribution of the flow [70]. The velocity fluctuations have a direct impact on the vapour void fraction (fraction of the flow channel volume occupied by gas-phase) and subsequently the liquid volume fraction. The experimental results of Michiyoshi et al [68] show that the increase in void fraction is accompanied by an increase in velocity gradients (consequently the wall shear stress) and thus enhances turbulence production. The turbulence intensities are also augmented by the increase in gas content in the flow, although it is not always the case as observed in Serizawa et al [67].

Michiyoshi et al [68] also conjectured that the enhancement in turbulence might also be related to the increase of high frequency oscillations of the bubble. However, the turbulence properties strongly depend upon the properties of the liquid-vapour interface. In ducted flows, the overall enhancement of turbulence production is influenced by the wall generated turbulence, i.e., the turbulence generated due to the enclosure walls and rotating inducer, and the bubble-induced turbulence. The wall generated turbulence in two-phase flows is similar to that of single-phase flows. The bubble-induced turbulence is similar to the turbulence production in buoyancy driven flows.

There exists a phenomenon of turbulence suppression away from the wall at certain conditions in two-phase bubbly flows. This is due to the energy dumping effects at the liquid-vapour

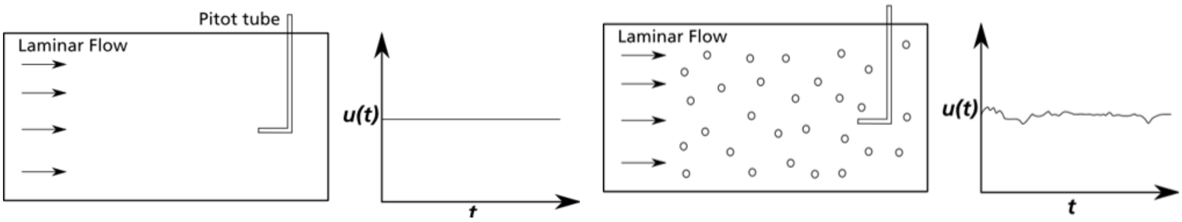

(a) Laminar Flow **(b)** Laminar flow with bubbles

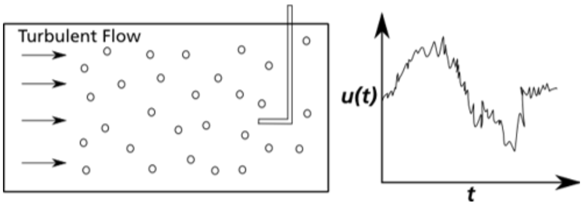

(c) Turbulent flow with bubbles

Figure 4-1: An approximate description of bubble induced velocity fluctuations in laminar and turbulent flows. (a) Laminar flow of a liquid, obviously and by definition, does not have any velocity fluctuations. (b) Bubble presence in a laminar flow produces minor fluctuations although theoretically laminar flow doesn't have any [69]. This is referred to as pseudo-turbulence. (c) In a turbulent flow, the overall fluctuations are influenced by the coupling of shear-induced and bubble-induced turbulence.

interfaces. The liquid-vapour interface can absorb the turbulence energy by deforming the shape of the interface. Thus, there is an increase in surface energy and also an increase in the energy dissipation at the vicinity of the interface due to turbulence eddy interfacial structure interaction [71].

In the upcoming sections, we shall discuss the incompressible simulations of a 3D inducer, implementation of the Rayleigh-Plesset equation and subsequent numerical analyses over certain mean pressure profiles and the actual pressure fields in a 3D inducer. We shall quantify the radius evolution and the frequency of oscillation and discuss the influence of thermal effects on oscillations. Finally, we shall discuss the turbulence-cavitation interaction and the methods to include bubble oscillation effects in turbulence models.

4-1 3D Inducer simulations

Three-dimensional incompressible flow simulations of canonical cryogenic turbopump inducer are carried out using DLR THETA code. The DLR in house code THETA (Turbulent Heat Release Extension of the TAU Code), a pressure-based version, was developed to simulate flow and chemical reaction in combustion chambers. The THETA code was created by DLR Institute of Combustion Technology and the DLR Institute for Aerodynamics and Flow Technology on the basis of the compressible DLR code TAU and is under continuous development in various research projects. It provides a platform for developing and validating new numerical computation methods as well as physico-chemical models for computing multiple flow regimes.

The fluid used is liquid oxygen at an ambient pressure in the order of 2-4 bar and inlet velocity in the order of 5-7 m/s. The rotation speed is in the order of 19,000-21,000 rpm. The mean pressure profiles are obtained after grid convergence (see figure 4-2).

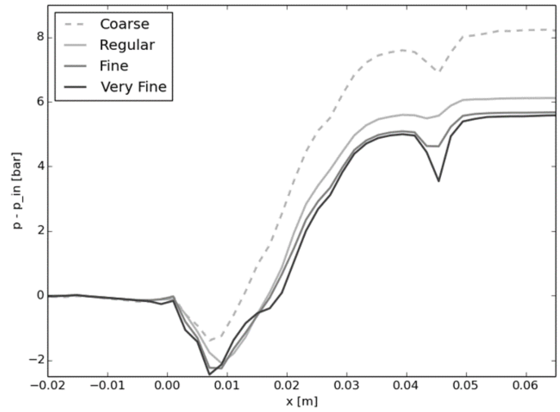

Figure 4-2: Mean pressure distribution in a 3D Inducer obtained from DLR THETA simulations. The pressure profiles are shown for different grid resolutions and the grid convergence test shows good agreement among results after a nominal resolution. These pressure profiles are axially averaged mean pressure profiles.

4-2 Numerical implementation of the Rayleigh-Plesset equation

A Python based code for the numerical implemetation and simulation of the Rayleigh-Plesset equation for bubble dynamics (as expressed in equation (4-1)) has been developed as a part of this work by the author in collaboration with Dr. Jean-Pierre Hickey. The free-stream pressure (p_∞) is input controlled while the temperature (T_∞), density ρ, vapour pressure (p_v), surface tension (S), latent heat (λ_{vap}), thermal conductivity (k), specific heat (c_p), thermal diffusivity ($\mathcal{A}$), and total simulation time (t) are maintained constant. The total simulation time corresponds to the convection time of the bubblein the inducer. The expression for initial non-condensable gas pressure is given by

$$p_{go} = p_\infty(0) - p_v(T_\infty) + 2S/R_o$$

An initial time step value is supplied but due to the numerical instability issues that arise from a constant time stepping scheme, a variable time stepping scheme is employed. The equation is moduled in such a way that one could include and exclude the thermal effects term before the execution of the program. For temporally discretising the ordinary differential equations, an explicit second order Runge-Kutta method is implemented. The method implemented is similar to the one in [72].

$$\overbrace{\frac{p_V(T_\infty)-p_\infty(t)}{\rho_l}}^{\text{Instantaneous tension term}} + \overbrace{\Sigma\frac{dR}{dt}\sqrt{t}}^{\text{Thermal effects term}} \overbrace{+\frac{p_g}{\rho_l}\left(\frac{T_B}{T_\infty}\right)\left(\frac{R_o}{R}\right)^{3\gamma}}^{\text{Non-condensable gas}} = \underbrace{R\frac{d^2R}{dt^2}+\frac{3}{2}\left(\frac{dR}{dt}\right)^2}_{\text{Inertial terms}} + \underbrace{\frac{4\nu_l}{R}\frac{dR}{dt}}_{\text{Viscous term}} + \underbrace{\frac{2S}{R\rho_l}}_{\text{Surface tension term}} \tag{4-1}$$

4-3 Rayleigh-Plesset simulations over mean pressure profiles

The pressure profiles obtained from the 3D inducer simulations are axisymmetrically averaged and an approximate mean pressure profile is obtained. This is done in order to simplify the analysis and qualitatively understand the bubble behaviour under a certain pressure field which is reflective of an inducer pressure field. Another similar pressure profile is also generated and the two approximate mean pressure profiles are used for the first set of RP simulations. This analysis includes 50 bubbles with increasing initial radii from 0.01 mm to 0.5 mm (increments of 0.01 mm) passing through the two mean pressure profiles. The simulation parameters are listed in table 4-1.

Parameters	**Value**
Fluid	Liquid Oxygen
Temperature, T_∞	80 [K]
Inlet Pressure, P_∞	3×10^5 [Pa]
Vapour Pressure, $P_v(T_\infty)$	30123 [Pa]
Liquid density, ρ_l	1190.5 [kg/m^3]
Vapour Density, ρ_v	1.4684 [kg/m^3]
Surface Tension, S	0.1522 [N/m]
Latent Heat (Vap), L	2.223×10^5 [J/kg]
Thermal Conductivity, k	0.16551 [W/m]
Specific Heat (liq.), $c_{p,l}$	1680.7 [J/kg-K]
Thermal diffusivity, $\mathcal{A}_l$	8.328×10^{-8} [m^2/s]
Initial time step, dt	2×10^{-7} [s]
Total simulation time, t	0.0008 [s]
Domain length, x	0.1 [m]

Table 4-1: Parameters for the numerical simulation of the Rayleigh Plesset equation

The two pressure profiles that are used are shown in figure 4-3. One profile has a sharp pressure recovery whereas the other has a flat profile after the first pressure fall. The initial pressure, P_∞ for both cases is 3 bar. The fall in pressure is 2.5 bar and the rise in pressure in 9 bar. The initial bubble radius, R_o is 10 μm. The freestream velocity is set at 125 m/s, which is reflective of the tip velocity of rotating inducer blades at 30,000 rpm.

The bubble growth and collapse over pressure profiles 1 and 2 are shown in figure 4-4. For the thermal effects, the time step was changed to 2×10^{-8} [s] and the thermodynamic parameter was calculated using equation (2-5).

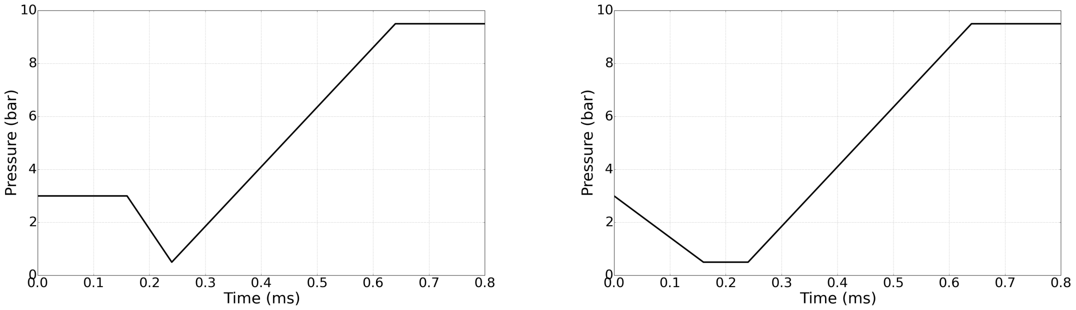

(a) Pressure profile 1 **(b)** Pressure profile 2

Figure 4-3: Pressure profiles for RP simulation are shown in this figure. Pressure profile 1 is an approximate mean pressure profile obtained after simplification of the mean pressure profile obtained from 3D Inducer simulations. This is done in order to reduce complexities and get a qualitative understanding of bubble behaviour in an inducer. Pressure profile 2 is a modification of pressure profile 1.

From figure 4-4, one can observe that there is a high radius ratio achieved in the absence of thermal effects. When the thermal effects are present, they inhibit the growth and also dampen out the bubble subsequent oscillations. The maximum radius ratio achieved in the presence of thermal effects is significantly smaller than the one achieved in their absence. As the thermal effects increase, the inhibition of growth and damping of oscillations become stronger. With the increase in the initial radius of the bubble, there is an initial increase in the maximum R/R_o value. However, the maximum R/R_o value decreases after a certain value of the initial radius.

The frequency and amplitude of oscillations for the range of radii are analysed using a discrete Fourier transform. For all radii, in both the pressure profiles, the lower frequencies have higher amplitudes of oscillation. The spectrum of the ratio of instantaneous radius and the initial radius is first obtained using fast fourier transform algorithm. Then, the amplitude is calculated by taking a square root of the sum of the squares of real and imaginary parts of the radius ratio spectrum. A contour plot highlighting the radii range, frequencies, and amplitudes are shown in figure 4-5. The amplitudes of oscillation for all the radii are similar and lie within a range of ± 25 non-dimensional units. Frequencies upto 10000 Hz have high amplitudes and are thus dominant. The damping of oscillations owing to thermal effects can be clearly observed in figures 4-4 and 4-5

The numerical simulation of the Rayleigh-Plesset equation for single bubble inside a cryogenic liquid oxygen flowing through an approximate mean pressure distribution in a turbopump inducer shows the variation of bubble size and the unsteady phenomena associated with such a cavitation bubble. The dominant frequencies observed and the amplitude of the oscillations give us a good idea of the time scales involved in bubble growth, collapse, and oscillations. The damping caused by the thermal effect and the inhibition of growth and collapse is also clearly observed. However, a more robust analysis is required in order to obtain a clear understanding of the influences of pressure gradients and thermal effects on bubble dynamics while it passes through the inducer blades.

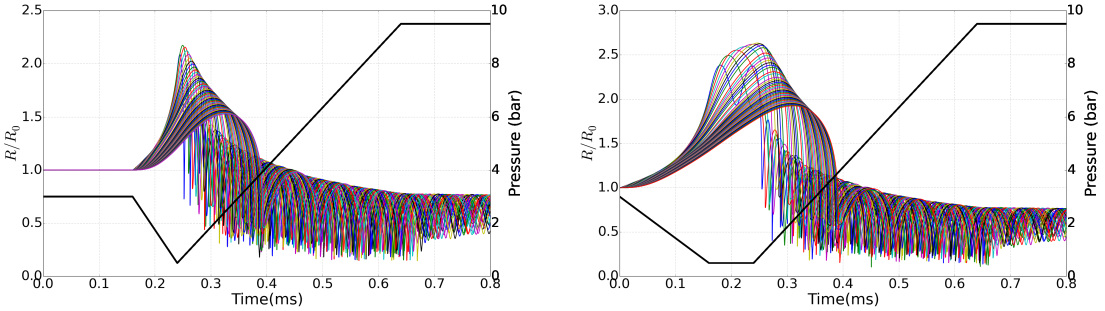

(a) No thermal effects - Profile 1 **(b)** No thermal effects

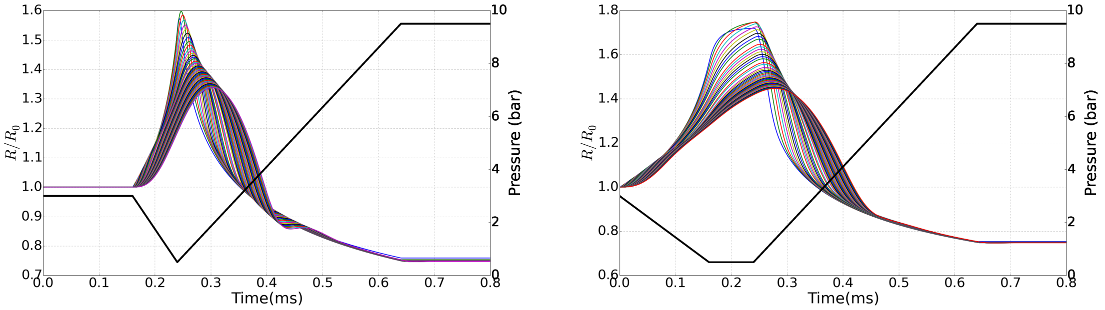

(c) Thermal effects - Profile 1 **(d)** Thermal effects - Profile 2

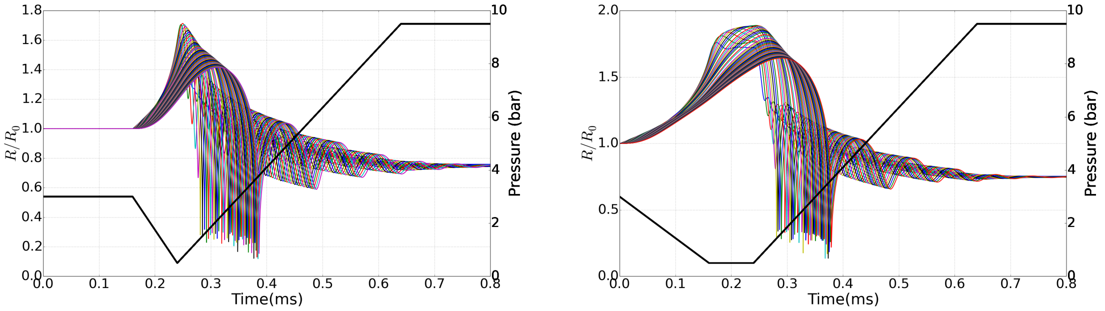

(e) 20 % Thermal effects - Profile 1 **(f)** 20 % Thermal effects - Profile 2

Figure 4-4: This figure shows the bubble radii evolution for two pressure profiles, with and without the thermal effects. For both pressure profiles, the bubble radius continues to grow as the pressure falls and they begin to collapse when there is pressure recovery. Since this is a non-linear process, there are multiple growth-collapses and the bubble radius oscillates and shrinks in magnitude over time. As the initial radius increased, the peak R/R_o values increased initially, reached a maximum, and decreased. Increase in thermal effects significantly reduce the bubble radius magnitude and dampen the oscillations severely.

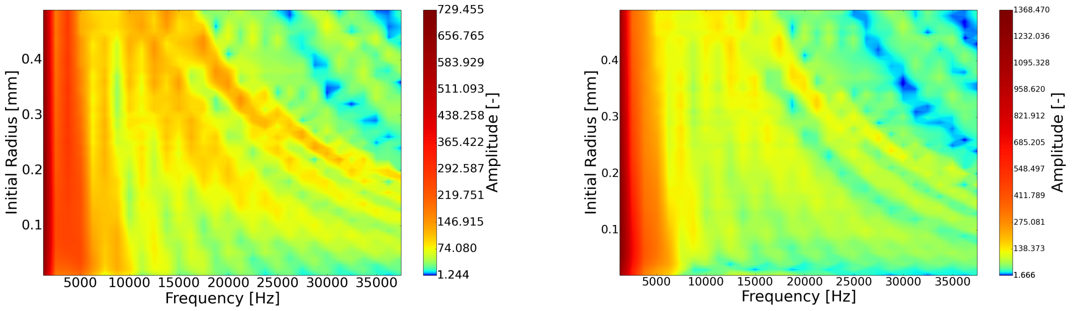

(a) No thermal effects - Profile 1 **(b)** No thermal effects

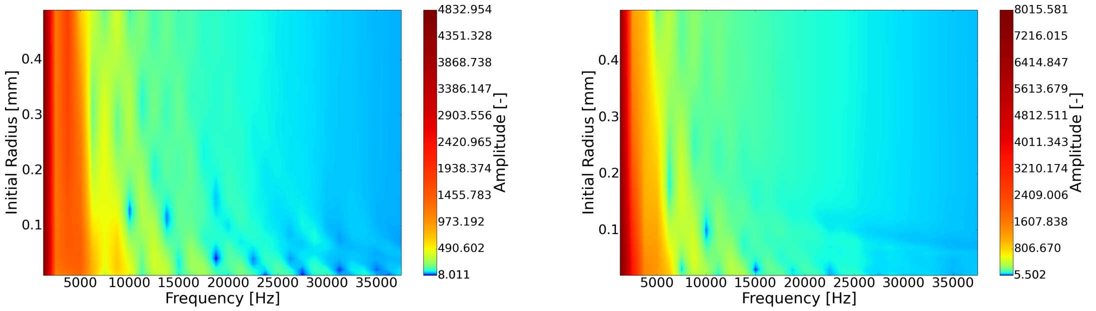

(c) Thermal effects - Profile 1 **(d)** Thermal effects - Profile 2

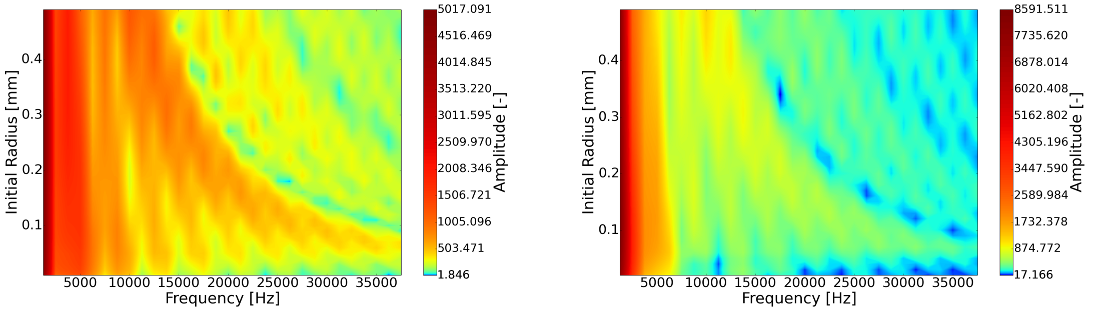

(e) 20 % Thermal effects - Profile 1 **(f)** 20 % Thermal effects - Profile 2

Figure 4-5: This figure shows the frequency and amplitude contours obtained from the Fourier transform of R/R_o spectrum for a range of initial bubble radii while traversing through the two pressure profiles. When there are no thermal effects, multiple dominant frequencies are observed with similar amplitudes. The thermal effects dampen the oscillations and the number of dominant frequencies as well as their values reduce significantly.

4-4 Rayleigh-Plesset simulation through a 3D inducer geometry

This analysis focuses on the bubble formation and collapse in a 3D inducer geometry. This shall give a physically accurate account of the bubble dynamics. The inducer has a diameter in the order of 10 cm with two blade passages. The fluid under consideration is liquid oxygen, entering the inducer inlet at approximately 3 bar pressure. The rotation speed under consideration is 20000 rpm.

First, 100 streamlines are extracted through which 100 individual bubbles shall travel from the inlet, through the rotating inducer, and onto the outlet within a particular time frame. The axial starting locations of the streamlines are fixed to a 2D plane that is 2 diameters upstream of the inducer and the radial locations are randomly selected. Each simulation consists of 100 streamlines with the corresponding bubbles having the same initial radius. For these individual streamlines, pressure distribution, three-component velocity, time, and location are obtained. Then, the characteristics of bubble dynamics are quantified and analysed by solving the Rayleigh-Plesset equation with the above extracted information as input. The results do not vary when the number of streamlines are altered since we neglect hydrodynamic interactions between bubbles.

The initial bubble radii under consideration are 10 μm, 100 μm, 150 μm, 250 μm, and 400 μm. The non-thermal RP equations have been simulated for all radii under consideration and the thermal RP equations were solved for 10 and 250 μm cases. Another simulation with increased rotational speed (30000 rpm) is simulated using 400 μm radius. The simulation parameters are mentioned in table 4-1. The bubble streamlines and the pressure profiles are shown in Figure 4-6. One could clearly observe the streamlines passing through the rotating inducer and then through the blade passages.

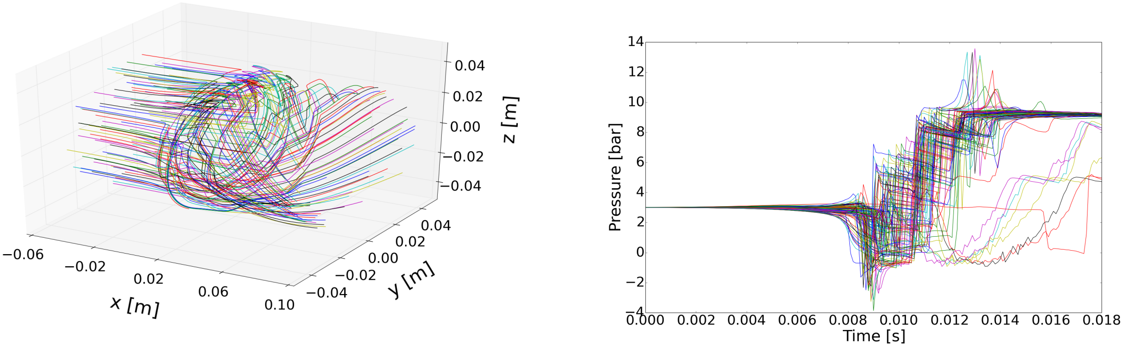

(a) Streamlines **(b)** Pressure Profiles

Figure 4-6: This figure shows the extracted streamlines and corresponding pressure profiles in an Inducer. In total, there are 100 streamlines (or paths) through which 100 individual bubbles travel. (a) The passage of bubbles through the rotating inducer could be clearly observed. (b) The pressure drops at the suction side of the rotating inducer and recovers downstream of the flow while locally dropping at blade passages. The pressure experienced by the bubbles also depend upon their proximity from the blade surface.

Applying the Rayleigh-Plesset equation, the radii evolution for each pressure profile for the

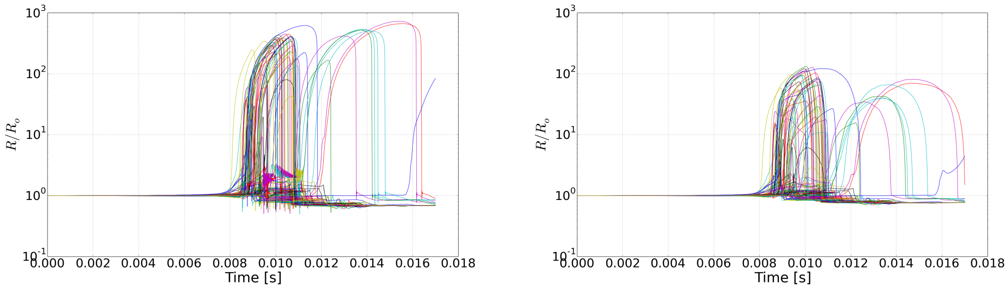

(a) Radii evolution over time - 10 μm

(b) Radii evolution over time - 10 μm - thermal effects

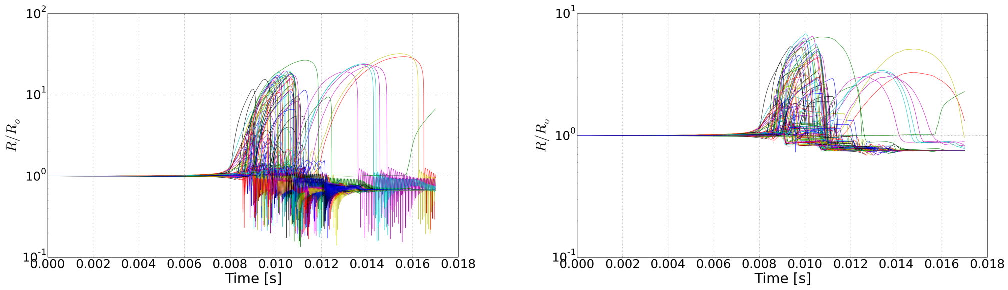

(c) Radii evolution over time - 250 μm

(d) Radii evolution over time - 250 μm - thermal effects

Figure 4-7: This figure shows the radii evolution for 10 and 250 μm R_o cases in a flow through the inducer with and without thermal effects. As the initial radius increased from 10 to 250 μm, the bubble oscillations grew stronger while the magnitude of R/R_o reduced by an order.

corresponding initial radius is obtained. Then, a fourier transform is applied over each of them to obtain the amplitude and the frequency of oscillations. Figures 4-7 show the radii evolution plot for 10 amd 250 μm cases.

The evolution of the radii is represented using the ratio, R/R_o, where R is the instantaneous bubble radius and R_o is the initial bubble radius. From figure 4-7 it is observed that the maximum radius ratio, $R/R_o|_{max}$, for 10 μm is an order of magnitude higher than that of 250 μm. Also, the thermal effects significantly reduce maximum bubble size as well as the the oscillations of the bubbles. Similar analyses, without thermal effects, are carried out for the rest of the cases. The observed trend, from 10 μ to 400 μm, is that the maximum R/R_o drops and the bubble oscillations increase.

A scatter plot, sized according to the magnitude of the radius and colored according to the velocity, is shown in figure 4-8. One could clearly observe the maximum size of the bubbles near the inducer blade tips. The X-component of the velocity drops almost to zero at the blade as the y and the z components increase. The angular velocity is highest at the blade tips and so is the velocity gradient.

The amplitudes and frequencies of oscillations are calculated by obtaining a fourier transform of the radii evolution. The 10 μ case does not yield discrete dominant frequencies but a set of minor peaks. The bubble oscillations are much more prominent and stronger in the 250 μm case. The strong oscillations of bubbles are also oberserved, in increasing order, in the 100,

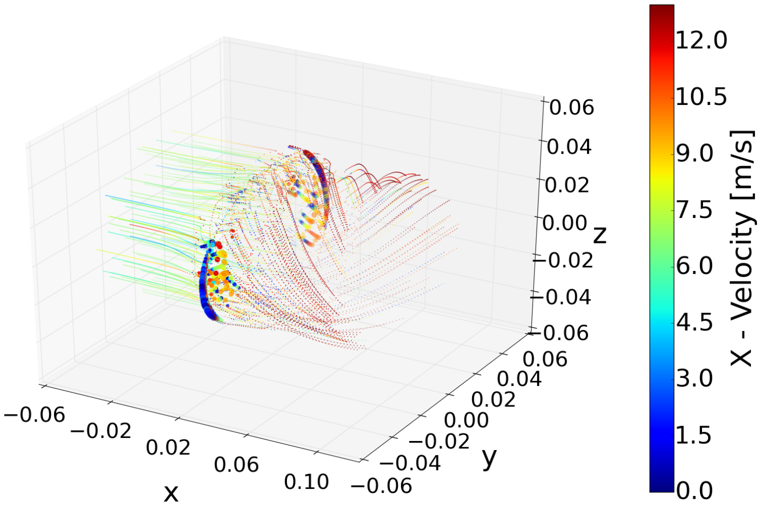

(a) Radii evolution through streamlines- 10 μm

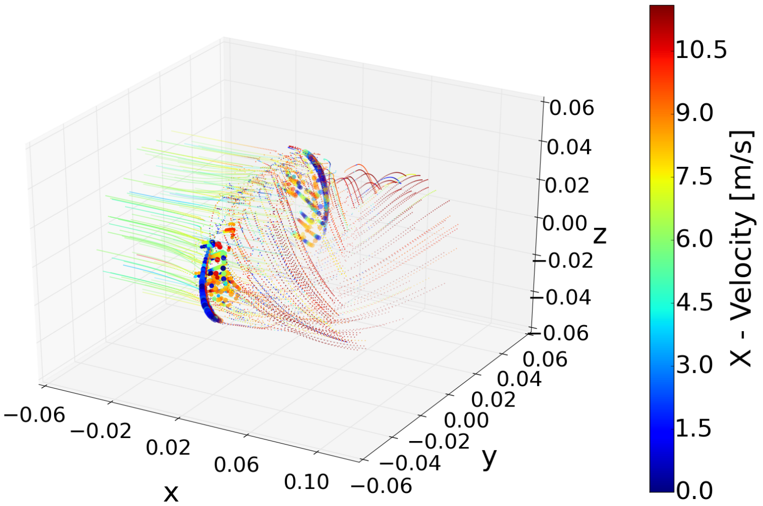

(b) Radii evolution through streamlines- 250 μm

Figure 4-8: This figure shows a scatter plot of bubble locations highlighting the bubble sizes and the corresponding axial velocities for 10 and 250 μm R_o cases in a 3D inducer (without thermal effects). The bubble sizes in the figure are scaled to the acutal bubble sizes obtained from RP simulations. Large R/R_o and the corresponding large void fractions are observed near the walls surrounding the rotating blade tip. At this location, the velocity gradient and shear stresses are high.

150, and 400 μm cases. The 250 μ case lies in between 150 and 400. Thus, the general trend observed here is that as the initial radii was increased, the growth and collapse time scales of the bubbles increased. The amplitudes of oscillations however showed a decreasing trend.

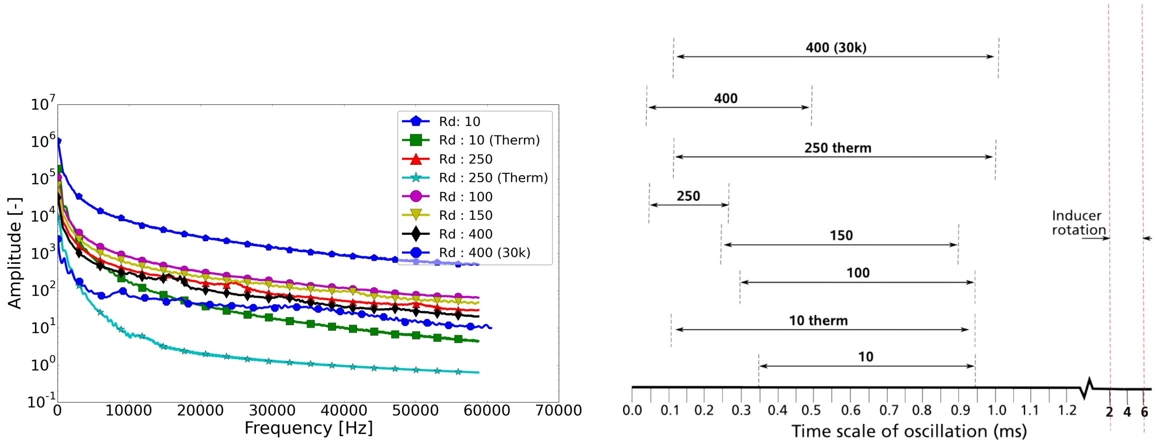

(a) Amplitude vs frequency plot **(b)** Time scales of oscillation

Figure 4-9: This figure shows the Amplitude vs Frequency plots for multiple initial radii cases and the corresponding time scales of oscillations. (a) As the initial radius increase, the amplitude reduces but oscillations increase. Thermal effects significantly reduce the magnitude and dampen oscillations (reduced frequency). Increase in rotational speed also leads to reduction in bubble oscillations because of more violent bubble collapses. (b) Bubble oscillation time scales (reciprocal of frequencies) are shown. These time scales and the bubble sizes could be used in turbulence-cavitation interaction studies.

Thermal effects were studied for 10 and 250 μm cases and some interesting observations are made. As expected, the amplitude of oscillations reduces an order of magnitude and the oscillations in multiple streamlines cease. However, oscillations were still found in certain streamlines which lead to the formation of discrete dominant frequencies. The average frequencies and amplitudes of bubble oscillations for all initial radii cases are shown in figure 4-9. The $R/R_o|_{max}$ values for all cases and the dominant frequencies are listed in table 4-2.

Initial Radii [μm]	$R/R_o\|_{max}$	Frequencies [Hz]
10	726.33	1057, 2230, 2820, 2935
10 (therm)	132.08	1057, 2940, 3880, 6800, 7760, 8350
100	32.06	1057, 2230, 2820, 3527, 3702, 4055
150	6.28	1115, 2235, 3180, 4115, 28200, 40722
250	76.15	3704, 6233, 7352, 16167, 24350, 50000
250 (therm)	65.27	1000, 1821, 3822, 6783, 8113, 9400
400	20.92	1932, 3650, 6465, 10116, 15583, 17107
400 (30000 rpm)	4.83	930, 1953, 2883, 3766, 4743, 8975, 17253

Table 4-2: Dominant frequencies for all initial radii

When the rotational speed was increased to an order of 30000 rpm, the results changed significantly. In the higher rotational speed case, an initial radius of 400 μ was used and the Rayleigh-Plesset equation was solved. The bubble oscillations are much more stronger and multiple dominant frequencies are observed. However, the amplitude of oscillations are very low. The $R/R_o|_{max}$ value dropped sharply by an order of magnitude compared to the corresponding 400 μm case with 20000 rpm.

So far, it is assumed that the flow in the inducer is a two-phase bubbly flow. The turbulence production and energy dissipation are enhanced in two-phase bubbly flows [68], especially near the wall region where the gradient of velocity fluctuation is large and the shear stress is very high. In our case, owing to high rotational speeds, the shear stress near the walls (especially the blade tip and the blade passage) is very high. Large bubbles are also observed near the region between the blade tip of the inducer and the wall of the enclosure. This means that the void fraction is also large in the region.

The results obtained for maximum radius ratio, dominant frequencies, and the time scales of oscillation is important to analyse the turbulence cavitation interaction. We shall relate the corresponding physical time and length scales to the turbulent time and length scales such that when we use RANS models, we can capture the effect of bubble oscillations on turbulence production and dissipation.

4-5 Turbulence-cavitation interaction

Turbulence and cavitation interact in such a way that they influence each other simultaneously. Turbulence influences the phase-distribution and predictions of momentum exchange between the phases [70]. While using two-equation models, which use the Boussinesq hypothesis, for simulating attached cavitating flows, there is an over-prediction of the turbulent viscosity which leads to the production of more stable cavities. In reality, there is significant unsteadiness associated with cavitation bubbles. To counter this issue, Reboud et al [22] proposed a correction to limit the turbulent viscosity. Although the application of this limitation leads to the observation of unsteadiness, it is a semi-empirical method applicable only to a restricted set of problems. From chapter 3, we observed that there are large differences in cavitation predictions due to change in turbulence models. Conversely, the bubble dynamics also influence the turbulence in the flow. Depending upon the operating conditions, they could attenuate or augment turbulence production and dissipation in the carrier phase.

Turbulence-cavitation interaction has to be studied and understood in order to account for cavitation physics while modelling the flow using RANS models. The state-of-the-art techniques to include the effect consist of source terms added to the corresponding turbulent kinetic energy (k) equation, dissipation rate (ε) equation, and specific dissipation rate (ω) equation in the case of two-equation models. For second moment closures, we add an interfacial work term to the main equation.

4-5-1 Second moment closure

In the case of second moment closure such as Reynolds stress model, we add an interfacial work term, W_{ij}, to the Reynolds stress transport equation. The interfacial work term acts as a source or a sink of turbulence energy resulting from velocity fluctuations in the liquid phase. This term is a work performed by the action of drag and added mass on the bubble. Added mass or virtual mass is the inertia added to the bubble because the accelerating/decelerating bubble should displace a volume of liquid in its vicinity as it moves through.

$$\frac{\partial\left(\rho R_{ij}\right)}{\partial t}+C_{ij}=P_{ij}+D_{ij}-\varepsilon_{ij}+\Pi_{ij}+\Omega_{ij}+\underbrace{W_{ij}}_{\text{Interfacial work}} \tag{4-2}$$

The primary problems associated with RSM modelling while trying to include the bubble dynamics are: first the relation between W_{ij} and the dissipation rate ε; second, modelling of the pressure redistribution term. In this, we have the interaction between mean flow field and the fluctuating bubble, and we have inter-bubble interactions. For the sake of simplicity, we assume that the inter-bubble interactions are negligible.

As explained earlier, the main sources of fluctuations come in the form of single-phase (shear-induced) turbulence, bubble fluctuations (pseudo-turbulence), and the fluctuations arising from bubble wakes. Assuming pseudo-turbulence to be inviscid, only the bubble wake fluctuations and the shear induced fluctuations occurring due to energy cascade remain. However, a statistical independence of these processes is assumed. Lance et al [73] measured decaying grid turbulence and have shown that the extra dissipation present in the vicinity of the bubbles approximately cancel out the drag force influence on the liquid phase. Thus, the bubble wake is in local equilibrium when the production due to bubble drag equals the dissipation in the wake. Thus, the interfacial work term is assumed to approximately cancel out the wake related dissipation.

$$W_{ij}=\frac{2}{3}\,\rho\,\varepsilon_{wall}\,\delta_{ij} \tag{4-3}$$

The next step is to account the effect of bubbles in the pressure-strain correlation term which is responsible for the redistribution of stresses. We have to pay particular attention to the isotropisation effect on the liquid phase turbulence [73, 66]. The term consists of rapid and slow moving parts of pressure-strain. For dilute flows, we do not have to modify the rapid part as the stretching and the alignment of the eddies could be unchanged. However, the mean shear could actually have some effect on the flow around the bubbles and on the wake structure. A return-to-isotropy term is added to the slow part of the pressure-strain term to include for the isotropisation caused by eddy distortion.

$$\Pi_{ij}^{bubblyflow}=\Pi_{ij}^{single-phaseflow}-C_L\left(1-\alpha_l\right)\left(\frac{\left|V_2-V_1\right|}{d_b}\right)\left(R_{ij}-\frac{2}{3}\delta_{ij}k\right) \tag{4-4}$$

Here, C_L is the lift coefficient associated with the lift force that acts on the bubble, α_l is the liquid volume fraction, V_2 is the velocity of the bubble (dispersed phase), V_1 is the velocity of the liquid (carrier phase), d_b is the bubble diameter, R_{ij} is the Reynolds stress, d_{ij} is the Kronecker delta function, and k is the turbulent kinetic energy. The quantity $|V_2 - V_1|/d_b$ is the reciprocal time scale (frequency of oscillation) that represents the interaction time between the bubble and the eddy. The C_L for a spherical bubble is positive and acts in the direction of decreasing velocity, i.e., towards the wall. The values are determined empirically.

4-5-2 Two-equation models

In the case of two-equation models such as $k-\varepsilon$, $k-\omega$, $k-\omega$ SST, and RNG-$k-\epsilon$, a set of additional source terms are used for the transport equations of turbulent kinetic energy k and dissipation rate ε. Assuming that the energy lost due to drag on the bubble is converted into turbulent kinetic energy. So a corresponding source term is added to the k equation. For the the ε equation, the k source term is divided by a time scale τ and added [74]. The k and ε source terms, and the corresponding ω source term for the $k-\omega$ models are given by equation (4-5)

$$S_k = F_{drag}\left|V_2 - V_1\right| \;\; ; \;\; S_\varepsilon = C_{\varepsilon B}\frac{S_k}{\tau} \;\; ; \;\; S_\omega = \frac{1}{C_\mu k}S_\varepsilon - \frac{\omega}{k}S_k \tag{4-5}$$

Here, F_{drag} is the drag force, $C_{\varepsilon B}$ is an empirical constant with values depends upon the time scale that is used; a good approximation is 2.0. In the usual sense where single phase turbulence is present, the time scale τ is expressed as k/ε. However, in the complex case of bubbly flow, we have two length and two velocity scales. The two length scales are the eddy size $l = k^{3/2}/\varepsilon$ and the bubble diameter d_b, and the two velocity scales are relative bubble velocity V_r (which equals $|V_2 - V_1|$) and the velocity of the eddy $\sqrt{k}$. This leads to the formation of four different time scales, the bubble time scale V_r/d_b, turbulence time scale $l/\sqrt{k} = k/\varepsilon = 1/\omega$, and two mixed time scales $d_b/\sqrt{k}$ and l/V_r. A relatively new time scale that is used, without clear motivation however, is $\tau = \left(d_b^2/\varepsilon\right)^{1/3}$.

If we consider $\tau = k/\varepsilon$, then the same dissipative mechanism applies for shear induced and bubble induced flows. For $\tau = d_b/V_r$, all eddies are assumed to be affected by the bubbles irrespective of their size or energy. Turbulence and bubble dynamics interactions could be pictured as a collision between bubble dynamics and the eddy actions. While considering mixed time scales, it is assumed that the eddies are spit while the move past the bubbles which happen in the order of $d_b/\sqrt{k}$ or l/V_r seconds. The physical accuracy of all these are debatable because of the lack of literature available. However these are the most promising ones.

The viscosity is also modified to include the bubble effects. $\mu_{eff} = \mu_t + \mu_b$. Where,

$$\mu_t = C_\mu \rho_l \frac{k^2}{\varepsilon} \tag{4-6}$$

$$\mu_b = C_B \rho_l \left(1 - \alpha_l\right) d_b |V_2 - V_1| \tag{4-7}$$

With C_B being the bubble induced turbulence coefficient with a value 0.6 proposed by Sato et al [75]. The drag force F_{drag} mentioned in equation (4-5) is expressed as

$$F_{drag} = -\frac{3}{4d_b} C_D \rho_l \left(1 - \alpha_l\right) \left|V_2 - V_1\right| \left(V_2 - V_1\right) \tag{4-8}$$

where C_D is the drag coefficient whose value depends upon the bubble Reynolds number or the Eötvös number for deformable bubbles. The Eötvös number is expressed as $\mathrm{Eo} = \Delta\rho g L^2/S$, where $\Delta\rho$ is the density difference between the phases, g is the gravitational acceleration, L is the characteristic length, and S is the surface tension.

A more simplified approach is to use a linear additive model for bubble induced turbulence to the grid generated turbulence [73]. However, this applies only for void fractions less than 1%. The Reynolds stresses corresponding to shear induced turbulence R_{SI} and bubble induced turbulence R_{BI} could be linearly added. However, when there are hydrodynamic interactions, the linearity is no longer applicable.

Similarly, additive terms could be used for turbulent kinetic energy k, where $k_{_{total}} = k_{_{SI}} + k_{_{BI}}$. $k_{_{SI}}$ corresponds to the single-phase turbulent kinetic energy and the bubble induced contribution is expressed as,

$$k_{BI} = \frac{1}{2}\left(1-\alpha_l\right)C_{am}\left|\overrightarrow{(V_2 - V_1)}\right| \tag{4-9}$$

where C_{am} is the added mass coefficient expressed as

$$C_{am} \approx \frac{1}{2}\left(1 + 2.78\left(1-\alpha_l\right)\right) \tag{4-10}$$

4-6 Conclusion

The study of the characteristics of bubble dynamics is important for physically accurate modelling of the flow. Our goal is to quantify the bubble length scale and the oscillation frequencies and time scales, study the turbulence cavitation interaction, and get an order of magnitude on the cavitation effects on turbulence. To this extent, 3D inducer simulations are carried out, pressure profiles are obtained, and the Rayleigh-Plesset equation for bubble dynamics is numerically simulated using the pressure field as input. The thermal effects were also included in the analyses. The length scale of the bubble is represented using a dimensionless quantity R/R_o where R is the instantaneous radius of the bubble and R_o is the initial radius. As the initial radius increased, the corresponding maximum R/R_o increased initially and then after a certain R_o, the maximum shows a decreasing tendency. This shows that the length scale is influenced significantly by the initial bubble radius. The thermal effects significantly reduced the R/R_o value for the same initial radius R_o.

The frequency of oscillation is obtained by taking a Fourier transform over the R/R_o spectrum. The observed trend is that as the R_o increased, the oscillations of bubbles increased significantly. The thermal effects significantly reduced the oscillations. The frequency is the reciprocal of the oscillation time scale, i.e., the characteristic time between bubble growth and collapse. There exists a set of dominant growth-collapse time scales. The velocity data obtained gives us the information regarding the bubble motion through the liquid.

Regarding the bubble dynamics influence on turbulence, we add source terms to the transport equations of turbulent kinetic energy, dissipation rate, and specific dissipation rate. The length scales and time scales obtained using the Rayleigh-Plesset simulation can be used in the turbulence source terms in order to model the flow with better physical accuracy.

The quantitative influence of initial radius on turbulence, with the time scale as $d_b/\sqrt{k}$, decreases by $\sim$ 81% for 10 μm initial radius between non-thermal and thermal simulations.

Similarly, for 250 μm, the reduction is by $\sim$ 15%. When the rotation speed is increased, for $R_o = 400$ μm, the reduction is $\sim$ 79%. The change in initial radius R_o also significantly affects the time scale based on d_b. If we are to use the oscillation time scale, shown in figure 4-9b, as the turbulence time scale, thereby assuming that all eddies are affected by the bubble dynamics, also then there is a significant change in the dissipation rate source term.

Chapter 5

Closure

5-1 Summary

The first chapter introduced the purpose for this project, the motivation and the three main objectives:

- Address the uncertainty associated with the importance of the choice of turbulence models while modelling cavitating flows in cryogenic turbopumps.
- Quantify and analyse the characteristics of bubble dynamics and their impact on flow turbulence in an actual turbopump inducer.
- Transpose the knowledge of turbulence modelling and bubble dynamics to assist the turbopump designers in their modelling strategies thus reducing overall costs and number of iterations while improving the predictive capabilities for cavitation.

The problems relating to turbopumps and the need for accurate modelling of cavitating flows are highlighted. Experimental investigation of cavitation, although robust and accurate, are iterative and incur heavy costs and take longer times. The need for numerical investigation with good predictive capabilities to achieve faster, reliable, and cheaper cavitation predictions is underlined. However, with a large amount of modelling uncertainties, the accurate predictive modelling is a difficult task. Thus the importance is placed on addressing these modelling uncertainties.

The second chapter focuses on the theoretical background and existing state-of-the-art modelling techniques employed presently to predict cavitation behaviour in cryogenic turbopumps. Theory of cavitation dynamics, numerical and turbulence modelling techniques are expounded. These give us a good understanding of the topics at hand and help us a great deal in later inferences regarding the behaviour of turbulence and other numerical models.

The third chapter focuses on the analysis of influence of parameters. The influence of cavitation flow solver and the choice of turbulence models in multiple flow regimes are highlighted.

The choice of cavitation flow solver, Barotropic Equation based Solver (BES) or the Transport Equation based Solver (TES), is of primary importance. The former predicts density only as a function of pressure whilst the latter uses a transport equation for the liquid volume fraction. The mixture density is then calculated as a function of the volume fraction. The turbulence models have varied influence, based on both the type of flow solver and the flow domain. Change in operating fluids contribute to a significant change in cavitation prediction in bounded flow problems. This is due to the constraint on the conservation of mass flow rate. Other parameters such as turbulence intensity, Reynolds number, cavitation model, and compressibility model do not have significant influence on cavitation predictions in all flow regimes.

The fourth chapter deals with the cavitation bubble dynamics in a cryogenic flow through a three-dimensional rotating inducer. The behaviour of the bubbles are characterised and the corresponding frequencies, length scales, and time scales of bubble oscillations are quantified. This information is vital to understand the bubble behaviour in realistic operating conditions as well as its usage in characterising the turbulence-cavitation interaction. Modelling strategies to include the bubble oscillation effects on flow turbulence in the RANS based turbulence models are exemplified. Inclusion of these shall allow the user to model the flow with much higher physical accuracy.

5-2 Conclusions

This chapter highlights the main findings and conclusions derived from this work. The research questions that were posed in the beginning are answered and the rationale behind them are expounded.

5-2-1 Check for requirements

A set of qualitative requirements for numerical modelling to be acceptable have been listed in the introduction chapter. However, these requirements were set apriori and are to be considered as rule of thumb rather than strict modelling requirements. In this section, we shall check how well these requirements have been satisfied.

- *The models shall yield an accuracy of ±15% in cavitation length predictions compared to the corresponding literature.*
    - The turbulence model accuracy varies widely depending upon the flow solver that is used and the type of flow regime. In the hemispherical headform case, for the BES simulations, $k-\omega$ and $k-\omega$ SST turbulence models satisfied this requirement. For TES all turbulence models achieved this accuracy. In the 2D Venturi case, where only TES simulations were done, $k-\varepsilon$, RSM, and RNG $k-\varepsilon$ did not satisfy the requirement. The reasons for their behaviour is elucidated in section 3-3-4
- *The simulations shall not take more than 10 hours time in a nominal personal computer setup having 8 gigabytes RAM and 4 cores of processors with 3.2 GHz frequency in total.*

  - The simulation time greatly depends upon the problem domain and mesh size. For the first three cases, TES simulations took well under 5 hours (when parallalized) and BES simulations took ∼10-25 hours. The dynamic TES used in the 3D rotating propeller case took ∼15 hours. However, in this geometry, such a simulation time is considered acceptable.

- *The models shall be widely validated in canonical flow problems.*
  - All turbulence models under consideration are widely validated models and have been formulated after decades of rigorous development.

- *The models shall have less approximations and shall closely emulate the physics of the problem in the investigated flow regimes.*
  - The Reynolds Stress Model has the least amount of modelling assumptions. The two-equation models use Boussinesq hypothesis for turbulent dynamic viscosity. The model equations and their underlying assumptions are listed in section 2-3-7.

- *The models shall have good numerical stability.*
  - All turbulence models have acceptable to very good numerical stability. The Reynolds Stress Model faced the least stability issues whereas $k - \varepsilon$ and $k - \omega$ suffered some minor stability issues depending upon the flow conditions.

5-2-2 On the importance of turbulence modelling, relative variations, and accuracy.

This section aims to answer the two research questions :

1. What is the relative importance of turbulence modelling in cryogenic turbopumps?
2. What is the most *accurate* RANS-based turbulence model to predict the size and onset of attached cavitation bubbles in cryogenic turbopump inducers?

Short answer: The choice of turbulence model is very important and influential in predicting cavitation size and topology. Also, the importance of the choice of turbulence model depends upon two main factors: The choice of cavitation solver and the type of flow domain. Accuracy encompasses physical and computational aspects. A comparison parameter such as cavitation length is used to adjudge the accuracy of each model. Theoretically, the Reynolds Stress Model should yield the most accurate result because of the least number of modelling assumptions involved. Two-equation models provide the minimum acceptable accuracy. Since the turbulence model results are problem dependent, one universal accurate turbulence model for all flow domains seems to be unavailable.

Explanation:

The choice of turbulence model plays a very important and an influential role in prediction cavitation. This importance of these are further enhanced when there are multiple interactions of flow phenomena. However, owing to the complex nature of flow interactions, it is very difficult to address them as a whole and infer the actual causes for the turbulence model behaviour. The following are the observations made from our analyses.

- In non-bounded flow with zero pressure gradient, when BES is used, the variation among turbulence models is significant. The analysed cavitation parameters are cavitation length, onset distance, and the distributions of pressure, density, and liquid volume fraction. Strong variations are found for all turbulence models in estimating the cavitation parameters. These could be linked to the density predictions which affect the modelled dissipation rate ε equation in $k-\varepsilon$ model as well as the Launder-Reece-Rodi RSM model which uses an ε equation. However, when TES is used for non-bounded flows, the variation among turbulence models is negligible. The TES has a better accuracy than the BES when compared with the corresponding literature [58].

- In the case of a non-bounded flow with a negative pressure gradient, when BES is used, some turbulence models and the laminar formulation show significant difference in the distributions of pressure and density. The cavitation length and onset predictions also differ by a considerable margin. Stark variation is found in the $k-\omega$ model which is very sensitive to the freestream pressure gradients. In this case, where there is a negative pressure gradient downstream of the flow, the distributions of pressure and densities are affected and vary from those of the other turbulence models. When TES is used, the strong variations disappear and the difference among the models becomes marginal. However, a moderate variation in liquid volume fraction distribution is observed. The variation of cavitation lengths and pressure distributions also vary starkly between BES and TES.

- In wall bounded flows where the proximity of the upper and lower walls were rather small, drastic differences were observed among the turbulence models. The $k-\omega$ SST and $k-\omega$ models predicted cavitation lengths which were in the range found in the literature [25]. However, there were severe overpredictions of cavitation lengths and volumes when $k-\varepsilon$, RSM, and RNG $k-\varepsilon$ models were used. The laminar fomulation did not produce any attached cavity. In RSM, the reflection of pressure from the walls affects the process of redistribution of energy which increases the parallel wall shear stress thereby stretching the cavity. In RNG $k-\varepsilon$, the production rate and the dissipation rate of turbulent kinetic energy reduces which leads to a lower turbulent viscosity μ_t. This means that there is a longer and a more unsteady cavity. With all other parameters remaining the same and only the turbulence model changed, the observance of drastic changes to cavitation parameters is unprecedented.

- When rotational effects are taken into account, theoretically, the Reynolds Stress Model should produce the most *accurate* result because of its inherent capability to account for rotation and other flow anisotropies. The two-equation models lack such capabilities and these have to be manually included as correction terms. Even then, the predictive capability of two-equation models is not as good. Although RSM is robust in its formulation for rotating flows, it does not perform very well under very high rotating speeds without the use of appropriate correction terms.

Thus, choice of turbulence model is too important to be neglected while simulating turbopump inducers. Multiphase interactions are not directly included in the RANS based turbulence models but corresponding source terms can be added to account for such effects. The thermodynamic effects found in cryogenic flows are accounted for using the cavitation models rather than the turbulence models. The turbulence in the flow do not affect the thermodynamics of the fluid.

The term accuracy encompasses the physical and computational accuracies. To analyse the physical accuracy of turbulence models, comparison parameters should be used. Cavitatation length and topology are used in our analyses based on which the model accuracies are defined. Computational accuracy relates to numerical stability and convergence of results. Both, physical and computational accuracies must be high, however the physical accuracy is more important to be truly reflective of the flow. For the turbulence models considered, the accuracy of each model is heavily dependent upon the flow solver and the flow domain. A universal turbulence model which is accurate for all flow solvers and flow domains seems to be unavailable.

5-2-3 On the characteristics of bubble dynamics in an inducer flow, thermal effects, and their effect on turbulence.

This section aims to answer the research questions,

1. What are the characteristics of bubble dynamics in an inducer flow and how do they affect flow turbulence?
2. How do the thermal effects affect the characteristic scales of oscillation?

Short answer: The main parameters of bubble dynamics that are quantified and analysed are oscillation frequencies, times scales, and bubble size. Bubble oscillations affect the main flow turbulence by either augmenting or attenuating them depending upon the flow conditions. These effects come in multiple forms such as pseudo-turbulence, interface deformation, bubble drag etc. The thermal effects occurring in the case of cryogenic fluids reduce the oscillation frequencies and the bubble length scale. Turbulence-cavitation interaction is accounted for by using a mixed turbulence time scale involving bubble radius and the velocity scale of eddies. Otherwise, if we are to assume that all eddies regardless of their size are affected by bubble oscillations, we can use the bubble oscillation time scale as the turbulence time scale.

Explanation:

The main characteristics of bubble dynamics that are analysed are oscillation frequencies and length & time scales of bubble oscillations. From the trends observed, under a varying pressure field, the maximum length scale (radius) of the bubbles increased initially, reached a maxima, and decreased eventually for a set of increasing initial bubble radii. This shows that there is a maximum length scale associated with a particular pressure profile. The bubble oscillations augment or attenuate the liquid phase turbulence based on operating conditions. There exists a phenomenon called 'pseudo-turbulence' which contributes positively or negatively towards the flow turbulence. Also, the drag and lift on the bubble, which is related to its length scale, influences the flow turbulence. These length and time scales associated with bubble oscillations are used in correspondence with the turbulence time scale. Four different time scales exist but there is no consensus on which time scale is the most physically representative one. If we are to assume that all turbulent eddies in the liquid phase regardless of their sizes are affected by bubble oscillations, we shall use the calculated time scales from the Fourier analysis of length scale spectrum estimated using the Rayleigh-Plesset equation. If we are to assume that the turbulent eddies influence the bubble dynamics and the bubble oscillations interact with the eddies simultaneously, we shall use the time scale which is represented as the diameter of the bubble divided by the square root of turbulent kinetic energy ($d_b/\sqrt{k}$).

The thermal effects occurring in cryogenic fluids have a significant effect on reducing the oscillation frequencies and length scales of oscillations. From the trends observed, the thermal effects reduce the maximum length scale at least by an order of magnitude. The time scales increase as the dominant frequencies of oscillation decrease. Thus, the thermal effects have an indirect effect on flow turbulence as they alter the characteristic scales of bubble dynamics.

In the turbulence models, we also add corresponding source terms to account for turbulence-cavitation interaction. These include the addition of interfacial work term to the Reynolds stress transport equation in second moment closures, addition of individual source terms in the equations for turbulent kinetic energy, dissipation rate, and specific dissipation rate. These source terms use the aforementioned time and length scales. Also, the turbulent viscosity uses an additive term to include bubble dynamics. Owing to the lack of literature, the veracity of these models are unclear. However, these techniques seem to be the most promising ones.

5-2-4 Problems with numerical and turbulence modelling of cavitating flows

In this section we discuss and to an extent summarise the problems associated with the numerical modelling of cavitation.

- Two different flow conditions are to be modelled; incompressible fluids such as pure liquid or pure vapour, and compressible two-phase transition layer. In the case of cryogenic cavitation, it is very difficult to model the interface because of the low liquid-vapour density ratio.
- In cavitating flows, we have multiphase mixtures for which there are no dependable equations of state. We also do not have proper model equations for the propagation of sound in these multiphase mixtures.
- The Rayleigh-Plesset equation for bubble dynamics has an inherent assumption for the bubble shape to be spherical. In reality, this is not the case.
- The eddy viscosity two-equation models and their constants are derived and iterated using steady-state non-cavitating mean flow data.
- The eddy viscosity models also use Boussinesq hypothesis for the calculation of turbulent eddy viscosity. This leads to similar turbulent eddy viscosities for different flow problems and will give erroneous results.
- The use of Boussinesq hypothesis also leads to the over-prediction of the turbulent eddy viscosity. This leads to the generation of stable cavities, reduces the two-phase structure shedding, and the development of the re-entrant jet thereby damping cavitation instabilities [20].

- For modelling unsteady cavitation sheets accurately, the turbulent eddy viscosity should have a limit. The limit is calculated using Reboud correction [22]. However, this is an empirical correction applicable to a very narrow set of problems.
- The eddy viscosity models are based on the eddy viscosity concept which assumes,
    - Reynolds stress tensor is characterised by single time and length scales.
    - The interaction between the eddies is not elastic in the case of molecular interactions in kinetic theory of gases.
    - The length and the time scales are not very small compared to the system length and time scales.
- The eddy viscosity is a scalar quantity and may not be even true for simple shear flow problems. They predict 2D flows well but they produce erroneous results even in the case of simple shear flows such as wall jets and channel flows with varying wall roughness.
- The eddy viscosity models do not distinguish among plane shear, plane strain and rotating plane shear flows.
- The two-equation models poorly account for the streamline curvature, rotational strains, and body forces. They also tend to neglect the history and non-local effects on the Reynolds stress anisotropies. These are due to the assumption that there are clearly defined separation scales for the second order Reynolds stress tensor.
- The second order closure models are robust and are devoid of the inaccuracies that arise due to the Boussinesq hypothesis. Although robust, the implementation is difficult and the required computational effort is much higher compared to other turbulence models.
- All RANS based models require robust modelling of the wall. For rotating problems, non-rotating wall conditions will lead to inaccurate results although these non-rotating wall models are widely available and validated.

In a bigger picture, the most difficult challenge would be to model a turbulent cavitating flow of a cryogenic fluid in a turbopump which rotates at speeds in the range of 20000-40000 rpm. We need to solve the Navier-Stokes equations which are Favre averaged and in conservative form, the two-equation turbulence model closure or a second order closure, and an equation for liquid volume fraction transport. The source and the sink terms in the liquid volume fraction transport equation are derived from semi-empirical models, interfacial dynamics model based on transport across the phases, or the Rayleigh-Plesset equation for bubble dynamics [11]. We also have to incorporate the thermodynamic effects that occur in cryogenic fluids and also account for the rotation induced anisotropies in the flow. The modelling of liquid-vapour interface and the speed of sound is also a challenge in the case of cryogenic fluids where the liquid-vapour density ratio is much lower compared to non-cryogenic fluids.

5-2-5 Considerations and recommendations to the turbopump designer

In this section, the main "take-aways" for the turbopump designer are highlighted.

- The choice of turbulence models plays a very important role in cavitation prediction. Arbitrarily chosing any turbulence model without strong reasoning shall lead to inaccurate or unreliable results thereby increasing the time and effort required to achieve the optimum design point.
- Simplification of the problem is of vital importance. Although a full 3-D simulation could yield a bigger picture, it does not help us understand and isolate the problems associated with turbulence model behaviour.
- The choice of turbulence model should be based on the type of investigation and the type of solver. Different turbulence model behave differently under set conditions.
- In bounded flow problems where the difference in predicted cavitation topology among the turbulence models is drastic, efficiency predictions for the inducer is severely affected. When there is an over-prediction of the cavity size, the volumetric flow rate as well as the outlet flow coefficient of the liquid phase reduces because the overall flow rate is conserved and that leads to blockage of the flow. This directly affects the predicted pump efficiency as well as the overall mass savings[1, 76]. This is illustrated in figure 5-1.

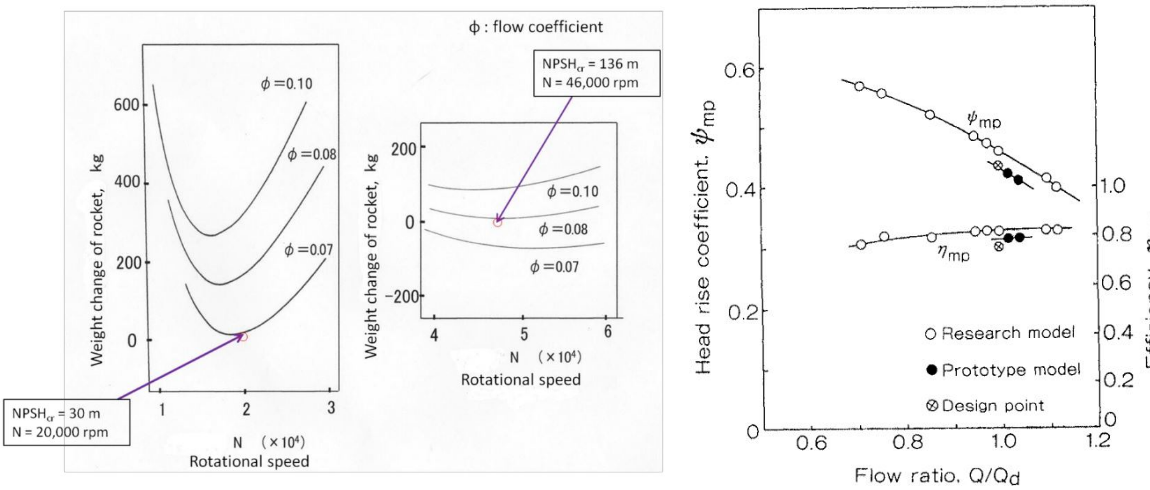

(a) Weight change (reduction) vs rotational speed for different flow coefficients

(b) Pump efficiency vs flow ratio for LOX turbopump

Figure 5-1: Figure (a) illustrates the relationship between weight reduction in rockets and the shaft rotational speed for different flow coefficients in the LE-7 engine LOX turbopump. Figure (b) illustrates the relationship between efficiency of the main pump and the flow ratio (ratio of volumetric flow rates of actual fluid and reference fluid - water). For the same rotational speed, when the liquid volumetric flow rate reduces (consequently the flow coefficient), the system mass increases and the efficiency drops. Over-prediction or under-prediction of cavitation size by the turbulence models will lead to drastic changes in the estimation of pump efficiency.

- Theoretically the second moment closure yields the highest level of closure which is computationally feasible. The two-equation models provide the minimum acceptable level of closure. In a practical sense, these may vary depending upon the problem.

- Cavitation dynamics influences flow turbulence. Inclusion of these dynamics is vital for physically accurate modelling. Moreover, the thermal effects significantly alter the cavitation bubble dynamics.
- There exists multiple modelling assumptions and empiricism. These are not generalisable and are problem specific. Thus, appropriate modelling corrections should be used for the corresponding flow regimes to capture intricate flow physics.
- Inclusion of multiphase source terms, rotational wall boundary conditions, and problem specific corrections to account for rotation, flow anisotropies, phasic-interaction, and flow unsteadiness shall lead to an improvement in predictive capabilites of the numerical and turbulence modelling techniques. These shall lead to faster, cheaper, and reliable results. Numerical simulations are the first step in testing the functionality and performance of turbopump inducers. These are complemented with experimental investigations. Thus, accurate predictive capabilities are desired and in many cases required to save costs.

5-3 Personal reflections of the author

During this work, the first issue that was encountered was the setting of definite goals which are of good scientific value and which were feasible within an objective period of 8 months. This was especially difficult given the broad scope of the investigation of cryogenic turbopump flows. The scientific goals were established and project planning was carried out, albeit with much more optimism because multiple simulation issues were unforeseen.

The real world flow through a rotating cryogenic turbopump inducer, in its entirety, involves multiple flow complexities, interactions, and unknown unknowns. The next step was to simplify the analyses by decomposing such a flow into canonical problems where the corresponding cavitation phenomena are well understood. To systematically investigate the influence of the choice of turbulence models and other simulation parameters, the results are compared against the literature and among themselves.

Regarding time management, all objectives of the work that were initially laid out were achieved within 8 months. However in between, there were certain times when the schedule was stretched. This was due to the underestimation of the difficulty in setting up the simulation cases and the time taken for simulations. It is now clear that these factors should surely be treated significantly while making project schedules.

To analyse the influence of each parameter, baseline cases were first setup and only one control parameter was changed at a time. The transformations that occurred in the analysed parameters were then compared with the baseline results. This type of analysis made the understanding of turbulence model influence very clear. This systematic approach is very useful for any kind of analysis.

In the analysis of cavitation bubble dynamics in rotating inducers, Python based codes for Rayleigh-Plesset equation implementation and simulation were developed by the author in collaboration with Dr. Jean-Pierre Hickey. Valuable data regarding the real frequencies and time scales of bubble oscillations in cryogenic inducer flows were obtained. This gave us a great insight into the bubbly turbulent flow through an inducer.

Turbulence modelling, simulation, and analysis of a cavitation in a full three-dimensional rotating inducer was set as an optional objective. However, as the other analyses progressed, very little use was found for such simulations. Comprehensive understanding of real cavitation phenomena occurring in such a case is very hard due to the existence of mutually coupled multiple interactions such as fluid-structure interactions, multiphase turbulence, rotation induced anisotropies, and cavitation unsteadiness in multiple flow domains. Addressing these together accurately in a RANS-based simulation is a seemingly impossible task. Some suggestions for future work based on the current work are posed in the following section.

5-4 Future Work

This work has so far focussed on asserting the importance and influence of the choice of turbulence models in cryogenic inducer flow simulations as well as the need to include the cavitation dynamics effects on turbulence for physically accurate modelling. However, plenty of analyses can be carried out with this work as the base. They are listed as follows:

- Robust turbulence closures with least modelling uncertainties and assumptions are required. Thus there is a need for the development of these closures which are physically reflective of the problem, i.e., to include robust closure models to include cavitation dynamics, phasic-interactions, rotation, and flow anisotropies.
- Thermal effects are included in cavitation modelling through the available cavitation models for source and destruction terms in the liquid volume fraction transport equation. However, the modelling constants used are empirical. The mushy interfacial dynamics provides a great scope for cryogenic cavitation modelling. Thus, this model needs to be implemented and simulations have to be carried out.
- A full three-dimensional simulation of a cryogenic flow through an inducer is required to get an overall picture. Although the information regarding certain behaviour is hard to deduce, it nevertheless provides a good overall picture.
- Analysis of interactions or coupling of flows in multiple domains and a subsequent analysis of the influence of turbulence models in such problems should give further insights into modelling approaches.
- Development and implementation of robust rotating wall models is a must to obtain any physically accurate results for rotating flows.

Appendix A

Solver equations

A-1 Barotropic Equation based Solver

In OpenFOAM, the Barotropic Equation based Solver (BES) is represented by `cavitatingFoam`. The flow equations along with the mass and momentum equations are,

$$Continuity: \ \frac{\partial \rho_m}{\partial t} + \nabla \cdot (\rho_m U) = 0 \tag{A-1}$$

$$Momentum: \ \frac{\partial \rho_m U}{\partial t} + \nabla \cdot (\rho_m U U) = -\nabla P + \nabla \cdot \left[\left(\mu_{eff} \left(\nabla U + (\nabla U)^T \right) \right) \right] \tag{A-2}$$

Where ρ_m, U, P, and μ_{eff} are mixture density, velocity, pressure, and effective viscosity respectively. The density is modelled by,

$$\frac{D\rho}{Dt} = \psi \frac{DP}{Dt} \tag{A-3}$$

$$\psi = \frac{1}{a^2} \tag{A-4}$$

$$\tag{A-5}$$

where ψ is the compressibility expressed as the reciprocal of the square of the speed of sound. The vapour mass fraction, mixture density, mixture compressibility, and the mixture viscosity are represented as,

$$\gamma = \frac{\rho_m - \rho_{l,sat}}{\rho_{v,sat} - \rho_{l,sat}} \tag{A-6}$$

$$\rho_m = (1-\gamma)\rho_l^0 + (\gamma\,\psi_v + (1-\gamma)\psi_l)P_{sat} + \psi_m(P - P_{sat}) \tag{A-7}$$

$$\psi_m = \gamma\,\psi_v + (1-\gamma)\,\psi_l \tag{A-8}$$

$$\mu_m = \gamma\,\mu_v + (1-\gamma)\,\mu_l \tag{A-9}$$

$$\mu_{eff} = \mu + \mu_t \tag{A-10}$$

Here, the subscripts m, v, l, t, and sat represent mixture, vapour, liquid, turbulent, and saturation respectively. If $\gamma = 1$, it denotes pure vapour phase and if $\gamma = 0$, it denotes pure liquid phase.

The speed of sound, a, is represented using one of the following models.

$$Linear: \qquad a = \frac{1}{\sqrt{\gamma\psi_v + (1-\gamma)\,\psi_l}} \tag{A-11}$$

$$Wallis: \qquad a = \frac{1}{\sqrt{\left(\gamma\rho_{v,sat} + (1-\gamma)\,\rho_{l,sat}\right)\left(\gamma\frac{\psi_v}{\rho_{v,sat}} + (1-\gamma)\left(\frac{\psi}{\rho_{l,sat}}\right)\right)}} \tag{A-12}$$

$$Chung: \qquad a = \frac{1}{\left[\frac{(1-\gamma)}{\sqrt{\psi_v}} + \gamma\frac{F}{\sqrt{\psi_l}}\right]\frac{\sqrt{\psi_v\psi_l}}{F}} \tag{A-13}$$

$$where,\, F = \sqrt{\frac{\frac{\rho_{v,sat}}{\psi_v}}{(1-\gamma)\,\frac{\rho_{v,sat}}{\psi_v} + \gamma\frac{\rho_{l,sat}}{\psi_l}}} \tag{A-14}$$

A-2 Transport Equation based Solver

The `interPhaseChangeFoam` solver uses the same continuity and momentum equations as that of `cavitatingFoam`. However, the barotropic compressibility model is not used. Instead, a transport equation for the liquid volume fraction α is used. For cavitation, three cavitation models could be implemented, the Kunz model, the Merkle model, and the Schnerr Sauer model.

The α transport equation is represented as,

$$\frac{\partial\alpha_l}{\partial t} + \frac{\partial}{\partial x_j}(\alpha_l\,u_i) = \dot{m}^+ + \dot{m}^- \tag{A-15}$$

With $\dot{m}^+$ and $\dot{m}^-$ are implemented as,

$$Kunz: \qquad m^+ = \frac{C_{prod}\,\alpha_l^2\,(1-\alpha_l)\,\rho_v}{t_\infty} \tag{A-16}$$

$$m^- = \frac{C_{dest}\rho_v\alpha_l MIN\,[0, P - P_{sat}]}{0.5\rho_l U_\infty^2\,t_\infty} \tag{A-17}$$

$$Merkle: \qquad m^+ = \frac{C_{prod}\,MAX\,[P - P_{sat}, 0]\,(1-\alpha_l)}{0.5\rho_l U_\infty^2\,t_\infty} \tag{A-18}$$

$$m^- = \frac{C_{dest}MIN\,[0, P - P_{sat}]\,\alpha_l\rho_l}{0.5\rho_v U_\infty^2\,t_\infty} \tag{A-19}$$

$$SchnerrSauer: \qquad m^+ = C_{prod}\,(1-\alpha_l)\,\alpha_l C_{pres}\,MAX\,[P - P_{sat}, 0] \tag{A-20}$$

$$m^- = -C_{dest}\,(1+\alpha_n-\alpha_l)\,C_{pres}\,MIN\,[0, P - P_{sat}] \tag{A-21}$$

$$\begin{aligned} V_n &= n\pi d_n^3/6 \\ \alpha_n &= V_n/\,(1+V_n) \\ R_b &= \left[\frac{4\pi n}{3}\frac{\alpha_l}{1+\alpha_n-\alpha_l}\right]^{1/3} \\ \rho_m &= \alpha_l\rho_l + (1-\alpha_l)\,\rho_v \\ C_{pres} &= \frac{3\rho_l\rho_v\sqrt{2/3\rho_l}\,R_b}{\rho_m\sqrt{P-P_{sat}}} \end{aligned}$$

In the above models, C_{prod} is the condensation coefficient and C_{dest} is the vapourisation coefficient. In the SchnerrSauer model, n is the number of number density of the bubble, d_n is the nucleation site diameter, α_n is the nucleation site volume fraction, R_b is the bubble radius, and C_{pres} is the pressure coefficient.

Appendix B

Analysis of influence of parameters

B-1 Hemishperical headform

B-1-1 Turbulence Intensity

The sensitivity of cavitation towards turbulence intensity is calculated and analysed in this section. To that extent, two cases with increased values of turbulence intensity are set up. The first case is run with 10% intensity and the second with 20% intensity. The shift is from low-medium turbulence, 5% - baseline, to medium turbulence, 10%, and finally to high turbulence, 20%.

Cases	Intensity	k $[m^2/s^2]$	ω $[s^{-1}]$
Baseline	0.05	1.47665	4437.1973
Medium Turbulence	0.1	5.90661	8874.3948
High Turbulence	0.2	23.6264	17748.7896

Table B-1: Hemispherical Headform - turbulence intensity sensitivity cases

All parameters in the baseline configuration remain the same except for the turbulence intensity I, turbulent kinetic energy k, and the specific dissipation ω. The results of the medium and high turbulence cases are compared with that of the corresponding baseline cases which have low turbulence.

- With the BES solver, the variations observed for medium (10%) and high (20%) turbulence intensity cases for cavitation length, onset distance, and $C_{p.min}$ are low.
- With the TES solver, the variation observed for the medium (0.1) and high (0.2) turbulence cases for the cavitation length, onset distance, and $C_{p,min}$ are negligible.
- The C_p vs s/d distributions for BES simulation cases and TES simulation cases are almost identical. The change in turbulence intensity has negligible effect on the pressure distribution over the hemispherical headform.

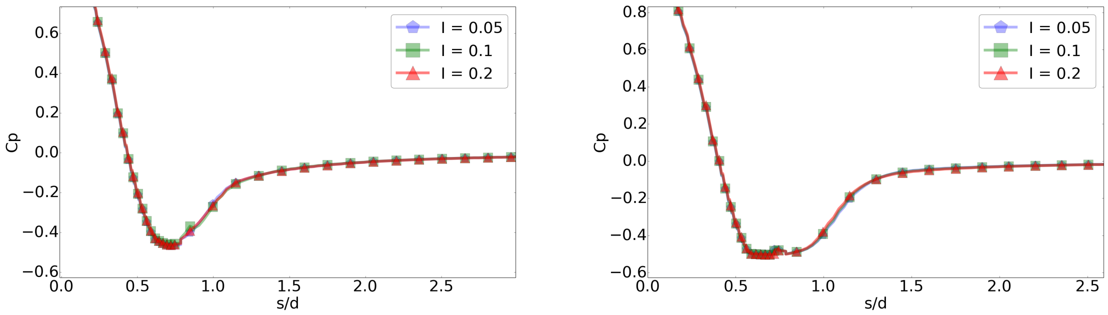

(a) Normalized pressure distribution - BES **(b)** Normalized pressure distribution- TES

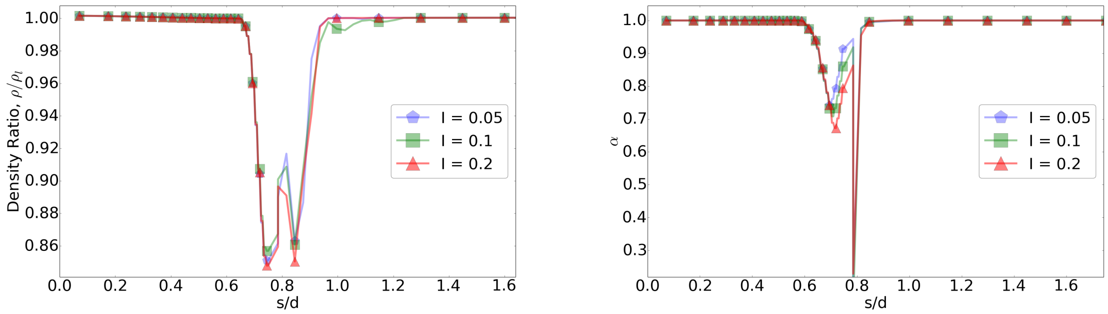

(c) Density ratio distribution - BES **(d)** liquid volume fraction distribution - TES

Figure B-1: Normalized pressure, density ratio, and liquid volume fraction distribution over the surface of the hemispherical headform are shown for the turbulence intensity sensitivity analysis. Figure (a) The cases yield results for $C_{p,min}$ which vary marginally and are within 1.5% of the baseline case. Figure(b) The cases yield almost identical results with the variation lying within 0.08%. Figure(c) & (d) All three cases capture the density and the liquid volume fraction similarly.

BES			
Case	Cavity Length	Cav. onset	$C_{p,min}$
I = 0.05	0.450153 d	0.636753 d	-0.468363
I = 0.1	0.469771 d	0.647285 d	-0.461016
I = 0.2	0.469771 d	0.647285 d	-0.463184
TES			
I = 0.05	0.377880 d	0.588424 d	-0.502942
I = 0.1	0.377880 d	0.588424 d	-0.503149
I = 0.2	0.377880 d	0.588424 d	-0.503368

Table B-2: Hemispherical Headform - Cavity Length, Onset, and $C_{p,min}$ Turbulence Intensity Sensitivity Analysis. The length and the onset distance are represented as a measure of the diameter of the hemispherical headform.

	BES		
Case	ΔCavity Length	ΔCav. Onset	$\Delta C_{p,min}$
I = 0.1	0.019618 d (4.35%)	0.017074 d (2.90%)	0.007347 (-1.57%)
I = 0.2	0.019618 d (4.35%)	0.017074 d (2.90%)	0.005178 (-1.11%)
	TES		
I = 0.1	-0.000000 d (-0.00%)	-0.000000 d (-0.00%)	-0.000207 d (0.04%)
I = 0.2	-0.000000 d (-0.00%)	-0.000000 d (-0.00%)	-0.000426 d (0.08%)

Table B-3: Hemispherical Headform - ΔCavity Length, ΔOnset, and $\Delta C_{p,min}$ Turbulence Intensity Sensitivity Analysis. The length and the onset distance are represented as a measure of the diameter of the hemispherical headform.

- The density and the liquid volume fraction distribution patterns also follow a similar pattern. The intensity doesn't play a major role in influencing cavitation parameters.

B-1-2 Barotropic compressibility model influence

In this section, we analyse the sensitivity of cavitation parameters due to the change in barotropic compressibility model. This analysis is only applicable for BES simulations because it uses a barotropic relation between density and pressure, i.e., the dependence of density is attributed only to the pressure and it is assumed to be independent of other physical parameters.

The varying parameter is the barotropic compressibility model. The BES baseline case uses the linear barotropic compressibility model. The other two models analysed are Wallis [77] and Chung models. The speed of sound in the fluid is modelled using these formulations.

The speeds of sound used are:

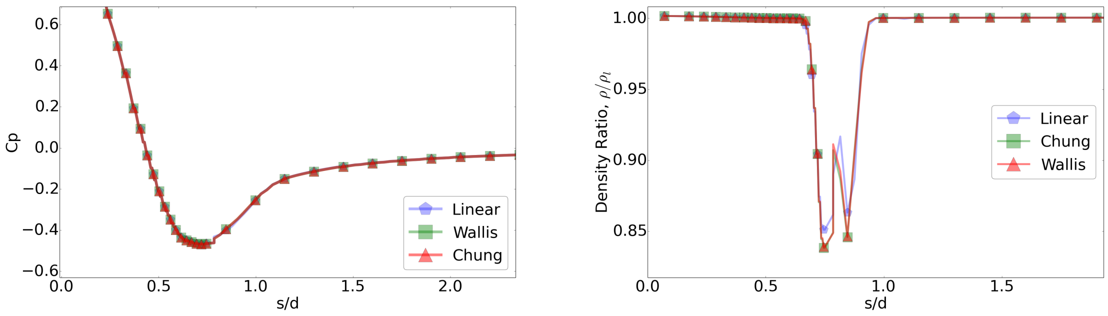

(a) Normalized pressure distribution - Barotropic Compressibility - BES

(b) Density ratio distribution - Barotropic Compressibility - BES

Figure B-2: Hemispherical Headform - Normalized pressure and density ratio distribution - barotropic compressibility model sensitivity. Figure(a) The pressure distributions are almost identical with the maximum variation being 0.03% compared to the baseline case. Figure (b) The density ratio distributions are very similar.

- The normalized pressure distribution (C_p vs s/d) plot and the density ratio distribution plot have identical patterns.

Model	Speed of sound, a
Linear	$\dfrac{1}{\sqrt{\left(\gamma\psi_v + (1-\gamma)\,\psi_l\right)}}$
Wallis	$\dfrac{1}{\sqrt{\left(\gamma\rho_{v,sat} + (1+\gamma)\,\rho_{l,sat}\right)\left(\gamma\dfrac{\psi_v}{\rho_{v,sat}} + (1-\gamma)\left(\dfrac{\psi_l}{\rho_{l,sat}}\right)\right)}}$
Chung	$\dfrac{\left(\dfrac{1}{\psi_v\ \psi_l}\right)\sqrt{\dfrac{\dfrac{\rho_v}{\psi_v}}{\dfrac{(1-\gamma)\,\rho_v}{\psi_v}+\dfrac{\gamma\rho_l}{\psi_l}}}}{\dfrac{(1-\gamma)}{\sqrt{\psi_v}}+\dfrac{\gamma}{\sqrt{\psi_l}}\sqrt{\dfrac{\dfrac{\rho_v}{\psi_v}}{\dfrac{(1-\gamma)\,\rho_v}{\psi_v}+\dfrac{\gamma\rho_l}{\psi_l}}}}$

Table B-4: List of barotropic compressibility models with the corresponding speed of sound formulation

BES			
Case	Cavity Length	Onset Distance	$C_{p,min}$
Linear	0.450153 d	0.636753 d	-0.468363
Chung	0.450153 d	0.636753 d	-0.468241
Wallis	0.450153 d	0.626154 d	-0.468308

Table B-5: Hemispherical Headform - cavitation length, onset distance, and $C_{p,min}$ Barotropic Compressibility Model Sensitivity Analysis. The length and the onset distance are represented as a measure of the diameter of the hemispherical headform.

BES			
Case	Δ Cav. Length	Δ Cav. Onset	$\Delta C_{p,min}$
Wallis	0.000000 d (0.00%)	-0.010599 d (-1.66%)	0.000054 d (-0.01%)
Chung	0.000000 d (0.00%)	0.000000 d (0.00%)	0.000122 (-0.03%)

Table B-6: Hemispherical Headform - Δ Cavity Length, Δ Onset, and $\Delta C_{p,min}$ Barotropic Compressibility Model Sensitivity Analysis. The length and the onset distance are represented as a measure of the diameter of the hemispherical headform.

- The cavitation length variation among the barotropic compressibility models are negligible in this case.
- The effect of the compressibility model on the cavitation onset distance, the density distrbution, and the pressure distribution are negligible.

B-1-3 Cavitation model influence

Cavitation models are used in the case of incompressible solvers such as TES to predict and simulate the phase change. The cavitation models used in this analysis are Kunz, Merkle, and Schnerr-Sauer model. For the TES baseline case, we use the Kunz model. Then, we change the cavitation model to analyse the sensitivity of pressure and liquid volume fraction distributions. We also analyse the effect on cavitation length, onset distance, and $C_{p,min}$.

The parameters involved are listed in table B-7

Cases	C_{prod}	C_{dest}	t_∞ [s]	ρ_l/ρ_v
Kunz Model (Base)	10	1000	5.04×10^{-4}	43184.77
Merkle Model	0.8	0.01	5.04×10^{-4}	1000
			Number Density $[m^{-3}]$	Nucleation Diameter [m]
Schnerr-Sauer	1	1	1.6×10^{13}	2.0×10^{-6}

Table B-7: Hemispherical Headform - Cavitation model influence test cases

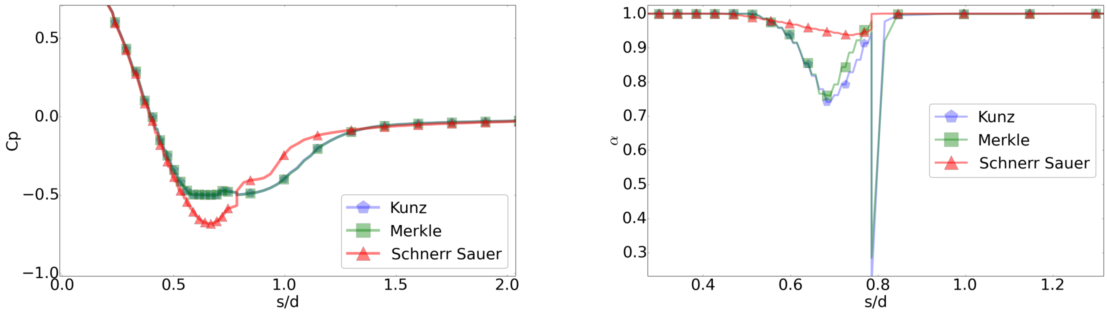

(a) Normalized pressure distribution - Cavitation Model - TES

(b) Density ratio distribution - Cavitation Model - TES

Figure B-3: Hemispherical Headform - Normalized pressure and liquid volume fraction distribution - cavitation model influence. Figure(a) The pressure distributions are nearly identical for Kunz and Merkle models. The SchnerrSauer model, in this case, over-predicts cavitation. Figure (b) The density ratio distributions are similar for Merkle and Kunz models whereas the SchnerrSauer model varies significantly.

- The Merkle and Kunz models show a similar distribution pattern for the pressure and liquid volume fraction.
- The variation observed in the cavitation length, onset, and $C_{p,min}$ are very low for the Merkle model when compared with the Kunz model.

Case	Cav. Length	Cav. Onset	$C_{p,min}$
Kunz	0.377880 d	0.588423 d	-0.502942
Merkle	0.377880 d	0.588423 d	-0.498046
Schnerr Sauer	0.235931 d	0.549467 d	-0.682666

Table B-8: Hemispherical Headform - cavitatation length, onset distance, and $C_{p,min}$ cavitation model influence

Case	Δ Cav. Length	Δ Cav. Onset	$\Delta C_{p,min}$
Merkle	0.000000 d (0.00%)	0.000000 d (0.00%)	0.004896 d (-0.97%)
Schnerr Sauer	-0.141949 d (-37.56%)	-0.038956 d (-6.62%)	-0.179725 d (35.73%)

Table B-9: Hemispherical Headform - change in cavitatation length, onset distance, and $C_{p,min}$ cavitation model influence

- The SchnerrSauer model produces a large variation in results. The model assumes a spherical shape for the cavity and computes cavitation parameters by taking the Rayleigh-Plesset equation into account. The spherical bubble assumption is not physically accurate for this problem set up.

- Thus, considering only the Merkle and the Kunz models, the sensitivity of cavitation parameters due to a change in cavitation model is not significant.

B-1-4 Reynolds Number

Rouse *et al* [58] state that cavitation is not affected by the change in Reynolds number as long as it is well above the critical value and in the same order of magnitude. Thus, in this section, we change the order of magnitude of the Reynolds number by adjusting the hemisphere diameter or the fluid viscosity to analyse the sensitivity of cavitation parameters.

Reynolds Number	diameter [m]	viscosity [Pa-s]	y^+_{wall}
Re = 2.22×10^5 (Base)	0.01	8.89×10^{-4}	87.5
Re = 2.22×10^4 (d)	0.001	8.89×10^{-4}	10.3
Re = 2.22×10^4 (μ)	0.01	8.89×10^{-3}	10.3

Table B-10: Hemispherical Headform - Reynolds number influence cases

- A change in Reynolds number by an order of magnitude yields results which vary significantly for BES simulations and also for TES simulations. Between the solvers, the variation is also large.

- For BES, the decrease in Reynolds number (increase in viscosity) results in a lower but a close prediction for $C_{p,min}$.

- The cavitation length predictions vary by a large margin for the low Reynolds number case compared to the BES baseline case. The onet distance varies moderately.

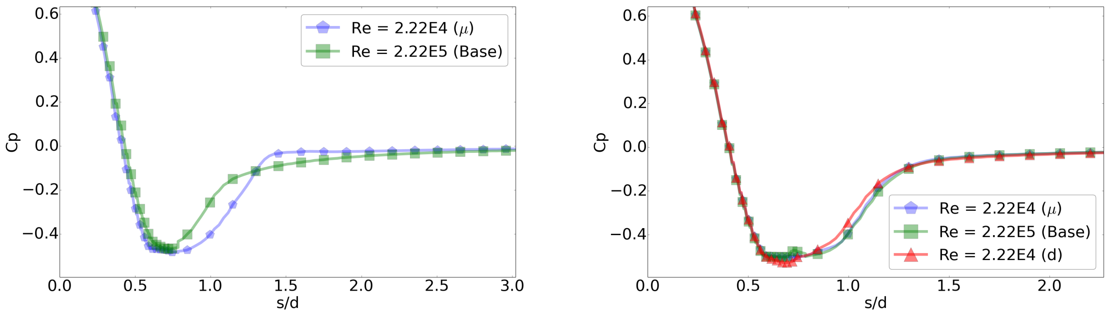

(a) Normalized pressure distribution - BES

(b) Normalized pressure distribution- TES

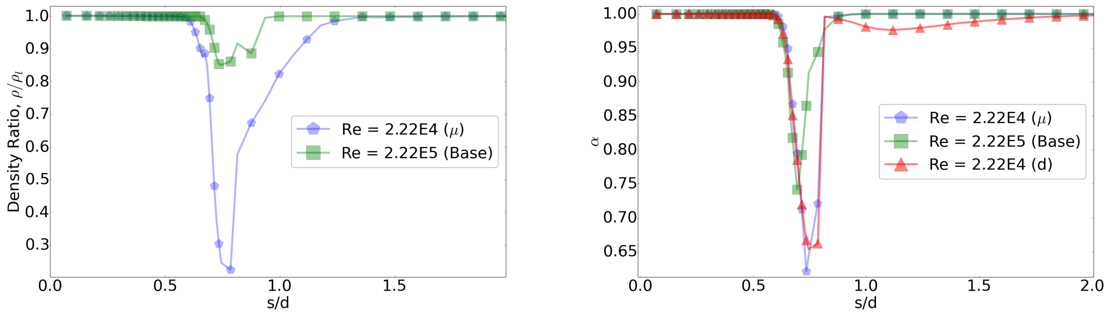

(c) Density ratio distribution - BES

(d) Liquid volume fraction distribution - TES

Figure B-4: Normalized Pressure, Density ratio, and liquid volume fraction distribution over the surface of the hemispherical headform are shown for the Reynolds number influence analysis.

Case	Cav. Length	Cav. Onset	$C_{p,min}$
	BES		
Re = 2.22E4 (μ)	1.159328 d	0.560743 d	-0.485013
Re = 2.22E5 (Base)	0.450153 d	0.636753 d	-0.468363
	TES		
Re = 2.22E4 (μ)	0.336838 d	0.599314 d	-0.501603
Re = 2.22E4 (d)	0.287427 d	0.588424 d	-0.527888
Re = 2.22E5 (Base)	0.377880 d	0.588424 d	-0.502942

Table B-11: Hemispherical Headform - cavity length, onset distance, and $C_{p,min}$ - Reynolds number influence

	BES		
Case	Δ Cav. Length	Δ Cav. Onset	$\Delta C_{p,min}$
Re = 2.22E4 (μ)	0.709175 d (157.54%)	-0.076010 d (-11.94%)	-0.016651 d (3.56%)
	TES		
Re = 2.22E4 (μ)	-0.041041 d (-10.86%)	0.010890 d (1.85%)	0.001339 d (-0.27%)
Re = 2.22E4 (d)	-0.090453 d (-23.93%)	-0.000000 d (-0.00%)	-0.024946 d (4.96%)

Table B-12: Hemispherical Headform - change in cavity length, onset distance, and $C_{p,min}$ - Reynolds number influence

- For TES, the low Reynolds numbers (viscosity and diameter changes) do not have a significant effect on $C_{p,min}$ prediction. The maximum variation is 4.96% compared to the TES baseline case.
- The cavitation length predictions by the low Re cases vary moderately with respect to the TES baseline case. The variations in onset distance predictions are negligible.

Bibliography

[1] G. Sutton and O. Bilbarz, *Rocket Propulsion Elements 7th Edition.* Wiley, 2010.

[2] Y. Wu, S. Li, S. Liu, H.-S. Dou, and Z. Qian, *Vibration of hydraulic machinery.* Springer, 2013.

[3] L. Stripling and A. Acosta, “Cavitation in turbopumps - part 1,” *Journal of Fluids Engineering*, vol. 84, no. 3, pp. 326–338, 1962.

[4] L. Stripling, “Cavitation in turbopumps - part 2,” *Journal of Fluids Engineering*, vol. 84, no. 3, pp. 339–349, 1962.

[5] A. Cervone, L. Torre, A. Pasini, and L. d’Agostino, “Cavitation and turbopump hydrodynamics research at alta spa and pisa university,” in *Fluid Machinery and Fluid Mechanics*, pp. 80–88, Springer, 2009.

[6] A. Cervone, R. Testa, C. Bramanti, E. Rapposelli, and L. D’Agostino, “Thermal effects on cavitation instabilities in helical inducers,” *Journal of propulsion and power*, vol. 21, no. 5, pp. 893–899, 2005.

[7] L. Torre, A. Cervone, A. Pasini, and L. d’Agostino, “Experimental characterization of thermal cavitation effects on space rocket axial inducers,” *Journal of Fluids Engineering*, vol. 133, no. 11, p. 111303, 2011.

[8] L. d’Agostino, “Turbomachinery developments and cavitation,” *VKI Lecture Series on Fluid Dynamics Associated to Launcher Developments, von Karman Institute of Fluid Dynamics, Rhode-Saint-Genese, Belgium, Apr*, pp. 15–17, 2013.

[9] Y. Tsujimoto, Y. Yoshida, Y. Maekawa, S. Watanabe, and T. Hashimoto, “Observations of oscillating cavitation of an inducer,” *Journal of fluids Engineering*, vol. 119, no. 4, pp. 775–781, 1997.

[10] K. Kikuta, Y. Yoshida, M. Watanabe, T. Hashimoto, K. Nagaura, and K. Ohira, “Thermodynamic effect on cavitation performances and cavitation instabilities in an inducer,” *Journal of Fluids Engineering*, vol. 130, no. 11, p. 111302, 2008.

[11] Y. Utturkar, J. Wu, G. Wang, and W. Shyy, “Recent progress in modeling of cryogenic cavitation for liquid rocket propulsion,” *Progress in Aerospace Sciences*, vol. 41, no. 7, pp. 558–608, 2005.

[12] Y. Utturkar, *Computational Modelling of Thermodynamic Effect in Cryogenic Cavitation.* PhD thesis, University of Florida, 2005.

[13] M. Deshpande, J. Feng, and C. L. Merkle, “Numerical modeling of the thermodynamic effects of cavitation,” *Journal of fluids engineering*, vol. 119, no. 2, pp. 420–427, 1997.

[14] A. Hosangadi, V. Ahuja, and R. Ungewitter, “Simulations of cavitating inducer flowfields,” in *JANNAF 38th combustion subcommittee meeting, Sandestin, FL*, 2002.

[15] A. Hosangadi and V. Ahuja, “A generalized multi-phase framework for modeling cavitation in cryogenic fluids,” *AIAA Paper*, vol. 4000, p. 2003, 2003.

[16] A. Hosangadi and V. Ahuja, “Numerical study of cavitation in cryogenic fluids,” *Journal of Fluids Engineering*, vol. 127, no. 2, pp. 267–281, 2005.

[17] V. Ahuja, A. Hosangadi, and S. Arunajatesan, “Simulations of cavitating flows using hybrid unstructured meshes,” *Journal of Fluids Engineering*, vol. 123, no. 2, pp. 331–340, 2001.

[18] V. Ahuja, P. Cavalla, and A. Hosangadi, “Multi-phase flow modeling on adaptive unstructured meshes,” *AIAA Fluids 2000 and Exhibit*, 2000.

[19] O. Coutier-Delgosha, P. Morel, R. Fortes-Patella, and J.-L. Reboud, “Numerical simulation of turbopump inducer cavitating behavior,” *International Journal of Rotating Machinery*, vol. 2005, no. 2, pp. 135–142, 2005.

[20] J.-L. Reboud, B. Stutz, and O. Coutier, “Two phase flow structure of cavitation: experiment and modeling of unsteady effects,” in *Third International Symposium on Cavitation, Grenoble, France*, 1998.

[21] J. Reboud, E. Sauvage-Boutar, and J. Desclaux, “Partial cavitation model for cryogenic fluids,” in *Cavitation and Multiphase Flow Forum, Toronto, Canada*, 1990.

[22] J. Reboud, O. Coutier-Delgosha, B. Pouffary, and R. Fortes-Patella, “Numerical simulation of unsteady cavitation flows: Some applications and open problems,” in *Fifth International Symposium on Cavitation*, 2003.

[23] E. Goncalves and R. F. Patella, “Numerical simulation of cavitating flows with homogeneous models,” *Computers & Fluids*, vol. 38, no. 9, pp. 1682–1696, 2009.

[24] J. Decaix and E. Goncalvès, “Time-dependent simulation of cavitating flow with k- âĎŞ turbulence models,” *International Journal for Numerical Methods in Fluids*, vol. 68, no. 8, pp. 1053–1072, 2012.

[25] E. Goncalvès, “Modeling for non isothermal cavitation using 4-equation models,” *International Journal of Heat and Mass Transfer*, vol. 76, pp. 247–262, 2014.

[26] S. B. Pope, *Turbulent flows.* Cambridge university press, 2000.

[27] R. E. Arndt, "Cavitation in vortical flows," *Annual Review of Fluid Mechanics*, vol. 34, no. 1, pp. 143–175, 2002.

[28] A. Prosperetti, "A generalization of the rayleigh–plesset equation of bubble dynamics," *Physics of Fluids (1958-1988)*, vol. 25, no. 3, pp. 409–410, 1982.

[29] C. E. Brennen, *Cavitation and bubble dynamics.* Cambridge University Press, 2013.

[30] E. Goncalvès and R. F. Patella, "Numerical study of cavitating flows with thermodynamic effect," *Computers & Fluids*, vol. 39, no. 1, pp. 99–113, 2010.

[31] T. Theofanous, L. Biasi, H. Isbin, and H. Fauske, "A theoretical study on bubble growth in constant and time-dependent pressure fields," *Chemical Engineering Science*, vol. 24, no. 5, pp. 885–897, 1969.

[32] A. Prosperetti, "Thermal effects and damping mechanisms in the forced radial oscillations of gas bubbles in liquids," *The Journal of the Acoustical Society of America*, vol. 61, no. 1, pp. 17–27, 1977.

[33] I. Senocak and W. Shyy, "A pressure-based method for turbulent cavitating flow computations," *Journal of Computational Physics*, vol. 176, pp. 363–383, 2002.

[34] Y. Delannoy and J. Kueny, "Cavity flow predictions based on the euler equations," in *ASME Cavitation and Multi-Phase Flow Forum*, vol. 109, pp. 153–158, 1990.

[35] A. Kubota, H. Kato, and H. Yamaguchi, "A new modelling of cavitating flows: A numerical study of unsteady cavitation on a hydrofoil section.," *Journal of fluid Mechanics*, vol. 240, no. 1, pp. 59–96, 1992.

[36] G. H. Schnerr and J. Sauer, "Physical and numerical modeling of unsteady cavitation dynamics," in *Fourth International Conference on Multiphase Flow, New Orleans, USA*, vol. 1, 2001.

[37] Y. Chen and S. Heister, "Modeling hydrodynamic nonequilibrium in cavitating flows," *Journal of Fluids Engineering*, vol. 118, no. 1, pp. 172–178, 1996.

[38] A. Singhal, N. Vaidya, and A. Leonard, "Multi-dimensional simulation of cavitating flows using a pdf model for phase change," *ASME Paper FEDSM97-3272*, 1997.

[39] C. L. Merkle, J. Feng, and P. E. Buelow, "Computational modeling of the dynamics of sheet cavitation," in *3rd International Symposium on Cavitation, Grenoble, France*, vol. 2, pp. 47–54, 1998.

[40] R. F. Kunz, D. A. Boger, T. S. Chyczewski, D. Stinebring, H. Gibeling, and T. Govindan, "Multi-phase cfd analysis of natural and ventilated cavitation about submerged bodies," in *Proceedings of FEDSM*, vol. 99, 1999.

[41] R. F. Kunz, D. A. Boger, D. R. Stinebring, T. S. Chyczewski, J. W. Lindau, H. J. Gibeling, S. Venkateswaran, and T. Govindan, "A preconditioned navier–stokes method for two-phase flows with application to cavitation prediction," *Computers & Fluids*, vol. 29, no. 8, pp. 849–875, 2000.

[42] S. Venkateswaran, J. W. Lindau, R. F. Kunz, and C. L. Merkle, "Preconditioning algorithms for the computation of multi-phase mixture flows," *AIAA Paper*, vol. 279, 2001.

[43] A. K. Singhal, M. M. Athavale, H. Li, and Y. Jiang, "Mathematical basis and validation of the full cavitation model," *Journal of fluids engineering*, vol. 124, no. 3, pp. 617–624, 2002.

[44] E. Goncalves, "Turbulence modelling in cavitating flows." Lecture - Advanced School in Cavitation - Udine, July 2014.

[45] B. E. Launder and D. Spalding, "The numerical computation of turbulent flows," *Computer methods in applied mechanics and engineering*, vol. 3, no. 2, pp. 269–289, 1974.

[46] W. Shyy, S. Thakur, H. Ouyang, J. Liu, and E. Blosch, *Computational techniques for complex transport phenomena*. New York: Cambridge University Press, 1997.

[47] S. T. Johansen, J. Wu, and W. Shyy, "Filter-based unsteady rans computations," *International Journal of Heat and fluid flow*, vol. 25, no. 1, pp. 10–21, 2004.

[48] J. Wu, Y. Utturkar, and W. Shyy, "Assessment of modeling strategies for cavitating flow around a hydrofoil," in *Fifth International Symposium on Cavitation, Osaka, Japan, Nov*, pp. 1–4, 2003.

[49] V. Yakhot, S. Orszag, S. Thangam, T. Gatski, and C. Speziale, "Development of turbulence models for shear flows by a double expansion technique," *Physics of Fluids A: Fluid Dynamics (1989-1993)*, vol. 4, no. 7, pp. 1510–1520, 1992.

[50] D. C. Wilcox *et al.*, *Turbulence modeling for CFD*, vol. 2. DCW industries La Canada, CA, 1998.

[51] P. E. Smirnov and F. R. Menter, "Sensitization of the sst turbulence model to rotation and curvature by applying the spalart–shur correction term," *Journal of Turbomachinery*, vol. 131, no. 4, p. 041010, 2009.

[52] C. G. Speziale, "Analytical methods for the development of reynolds stress closures in turbulence," tech. rep., DTIC Document, 1990.

[53] H. K. Versteeg and W. Malalasekera, *An introduction to computational fluid dynamics: the finite volume method*. Pearson Education, 2007.

[54] B. Launder, G. J. Reece, and W. Rodi, "Progress in the development of a reynolds-stress turbulence closure," *Journal of fluid mechanics*, vol. 68, no. 03, pp. 537–566, 1975.

[55] F. Mashayek and R. Pandya, "Analytical description of two-phase turbulent flows." Review article submitted for publication.

[56] D. Cokljat, M. Slack, S. Vasquez, and A. Bakker, "Reynolds-stress model for eulerian multiphase," *Progress in computational Fluid Dynamics, an International Journal*, vol. 6, no. 1, pp. 168–178, 2006.

[57] N. Beishuizen, B. Naud, and D. Roekaerts, "Evaluation of a modified reynolds stress model for turbulent dispersed two-phase flows including two-way coupling," *Flow, Turbulence and Combustion*, vol. 79, no. 3, pp. 321–341, 2007.

[58] H. Rouse and J. S. McNown, “Cavitation and pressure distribution: head forms at zero angle of yaw,” 1948.

[59] J. Hord, *Cavitation in Liquid Cryogens: Hydrofoil. II*, vol. 2156. National Aeronautics and Space Administration, 1973.

[60] R. W. Erney, *VERIFICATION AND VALIDATION OF SINGLE PHASE AND CAVITATING.* PhD thesis, The Pennsylvania State University, 2008.

[61] R. McCarty, J. Hord, and H. Roder, “Selected properties of hydrogen (engineering design data), us dept,” *Commerce, NBS*, 1981.

[62] B. A. Younglove, “Thermophysical properties of fluids. i. argon, ethylene, parahydrogen, nitrogen, nitrogen trifluoride, and oxygen,” tech. rep., DTIC Document, 1982.

[63] C. Open, “Openfoam user guide,” *OpenFOAM Foundation*, vol. 2, no. 1, 2011.

[64] S. Jakirlic, K. Hanjalic, and C. Tropea, “Modeling rotating and swirling turbulent flows: a perpetual challenge,” *AIAA journal*, vol. 40, no. 10, pp. 1984–1996, 2002.

[65] F. Mashayek and R. Pandya, “Analytical description of particle/droplet-laden turbulent flows,” *Progress in energy and combustion science*, vol. 29, no. 4, pp. 329–378, 2003.

[66] D. Lathouwers, *Modelling and simulation of turbulent bubbly flow.* PhD thesis, TU Delft, Delft University of Technology, 1999.

[67] A. Serizawa, I. Kataoka, and I. Michiyoshi, “Turbulence structure of air-water bubbly flow-ii. local properties,” *International Journal of Multiphase Flow*, vol. 2, no. 3, pp. 235–246, 1975.

[68] I. Michiyoshi and A. Serizawa, “Turbulence in two-phase bubbly flow,” *Nuclear engineering and design*, vol. 95, pp. 253–267, 1986.

[69] S. Hosokawa and A. Tomiyama, “Bubble-induced pseudo turbulence in laminar pipe flows,” *International Journal of Heat and Fluid Flow*, vol. 40, pp. 97–105, 2013.

[70] S. Wang, S. Lee, O. Jones, and R. Lahey, “3-d turbulence structure and phase distribution measurements in bubbly two-phase flows,” *International Journal of multiphase flow*, vol. 13, no. 3, pp. 327–343, 1987.

[71] A. Serizawa and I. Kataoka, “Turbulence suppression in bubbly two-phase flow,” *Nuclear Engineering and Design*, vol. 122, no. 1, pp. 1–16, 1990.

[72] H. Alehossein and Z. Qin, “Numerical analysis of rayleigh–plesset equation for cavitating water jets,” *International Journal for Numerical Methods in Engineering*, vol. 72, no. 7, pp. 780–807, 2007.

[73] M. Lance and J. Bataille, “Turbulence in the liquid phase of a uniform bubbly air–water flow,” *Journal of Fluid Mechanics*, vol. 222, pp. 95–118, 1991.

[74] R. Rzehak and E. Krepper, “Bubble-induced turbulence: Comparison of cfd models,” *Nuclear Engineering and Design*, vol. 258, pp. 57–65, 2013.

[75] Y. Sato, M. Sadatomi, and K. Sekoguchi, “Momentum and heat transfer in two-phase bubble flow -i. theory,” *International Journal of Multiphase Flow*, vol. 7, no. 2, pp. 167–177, 1981.

[76] K. Kamijo, *Research and Development of Rocket Turbopumps - 35 Years in Retrospect.* Tohoku University Press, Sendai, Japan, February 2013.

[77] G. B. Wallis, *One-dimensional two-phase flow*, vol. 1. McGraw-Hill New York, 1969.